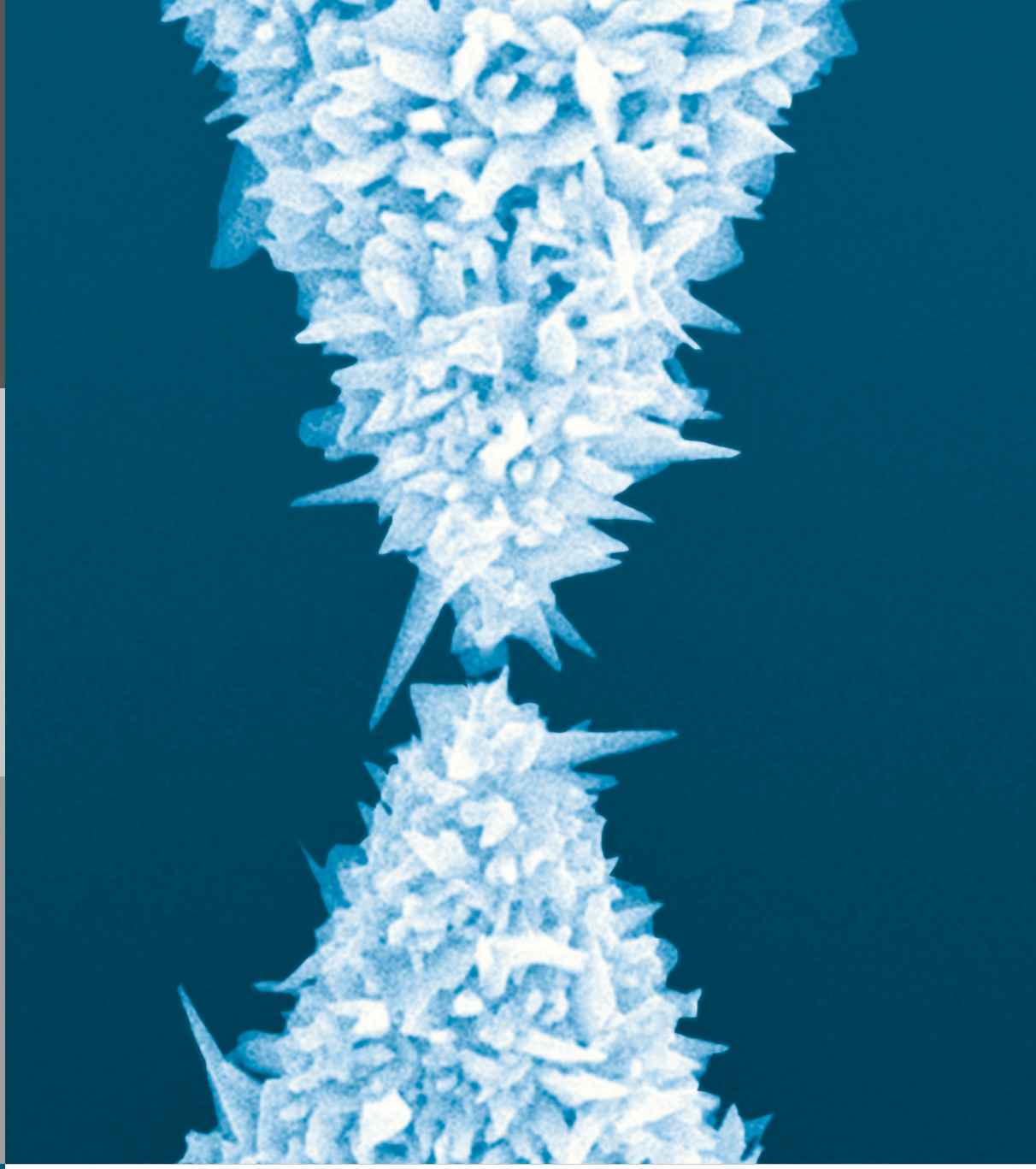

Fabrication of Nanogaps and Investigation of Molecular Junctions by Electrochemical Methods

Zhiwei Yi

Member of the Helmholtz Association

JÜLICH
FORSCHUNGSZENTRUM

Schriften des Forschungszentrums Jülich
Reihe Information / Information Band / Volume 22

Forschungszentrum Jülich GmbH
Peter Grünberg Institute / Institute of Complex Systems
Bioelectronics (PGI-8 / ICS-8)

Fabrication of Nanogaps and Investigation of Molecular Junctions by Electrochemical Methods

Zhiwei Yi

Schriften des Forschungszentrums Jülich
Reihe Information / Information Band / Volume 22

ISSN 1866-1777 ISBN 978-3-89336-812-9

Bibliographic information published by the Deutsche Nationalbibliothek.
The Deutsche Nationalbibliothek lists this publication in the Deutsche Nationalbibliografie; detailed bibliographic data are available in the Internet at http://dnb.d-nb.de.

Publisher and Distributor:	Forschungszentrum Jülich GmbH Zentralbibliothek 52425 Jülich Phone +49 (0) 24 61 61-53 68 · Fax +49 (0) 24 61 61-61 03 e-mail: zb-publikation@fz-juelich.de Internet: http://www.fz-juelich.de/zb
Cover Design:	Grafische Medien, Forschungszentrum Jülich GmbH
Printer:	Grafische Medien, Forschungszentrum Jülich GmbH
Copyright:	Forschungszentrum Jülich 2012

Schriften des Forschungszentrums Jülich
Reihe Information / Information Band / Volume 22

D 82 (Diss., RWTH Aachen University, 2012)

ISSN 1866-1777
ISBN 978-3-89336-812-9

The complete volume is freely available on the Internet on the Jülicher Open Access Server (JUWEL) at http://www.fz-juelich.de/zb/juwel

To my families

Abstract

In this work, an electrochemical method of fabricating and modifying nanogap electrodes on a silicon chip was developed. Electrochemical deposition was used to narrow a nanogap template and the electrodeposition process was optimized that the electrodeposited nanogap electrodes have needle-like surface morphology, which makes them suitable for assembling single Metal/Molecule/Metal molecular junctions. In addition, a setup combining mechanical controlled break junction (MCBJ) and electrochemical deposition was introduced, which combined the advantages of both techniques. By this setup, atomic scale junctions not only can be formed and broken repeatedly as those in MCBJ, but also can be regenerated easily by electrochemical deposition. A new type of molecular junctions based on electrostatic interactions was assembled. This type of molecular junctions can be used to investigate the charge transport properties across intermolecular electrostatic interfaces.

The nanogap electrode arrays comprising twenty-nine pairs of facing nanoelectrodes were fabricated on a silicon chip by electron beam lithography. The nanogap electrodes had a width of 100 nm and the size of the nanogap formed by the facing nanogap electrodes was defined as 150 nm. These nanogap arrays cannot directly be used for assembling molecular junctions, but can be used as templates for following electrochemical modification.

The electrochemical modification of the nanogap electrodes were performed in chloroauric acid solution and the morphology of the deposited gold clusters was investigated under various voltages. It was found that at low over-potentials (0.1 V), the deposited electrodes were observed to have needle-like surfaces and the radius of curvature of the nano-needle was as small as 2 nm [1]. The nanogaps formed by such nano-needles can reduce the possibility of integrating multiple molecules when assembling molecular junctions, and thus they are suitable to study transport properties through single molecules.

The electrodeposited nanogaps have fixed gap sizes, that is not convenient for adjusting the nanogap size in situ. For this reason, the MCBJ techniques were introduced and combined with the electrochemical modification techniques. This setup features with low electrochemical leakage current(as low as 20 pA) at the electrolyte/substrate interfaces and makes it suitable to measure molecules of low conductivity in solutions.

A new type of molecular junctions based on electrostatic interaction was assembled in solution on such electrochemical break junction set-up. The electrostatic interfaces play

important roles in the biological macromolecule interactions and in the bio-sensor applications. The conductance through single molecular electrostatic interfaces is $3.4\,\mathrm{x}\,10^{-5}\,\mathrm{G}_0$, which is one order of magnitude smaller than the corresponding single covalent interface ($3\,\mathrm{x}\,10^{-4}\,\mathrm{G}_0$), indicating that the electrostatic coupling is strong enough to form an electron transport pathway, but the electron transfer rate across the electrostatic interface is lower than the electron transfer rate across the covalent bond [2].

Contents

1. Introduction

With the development of semiconductor industry, the size of electronic components scales down to nanometer dimensions. Molecules, the size of which ranges from several nanometers to tens of nanometers, become potential candidates to substitute or extend the functions of silicon-based electronic components. To use molecules as electronic components, the knowledge of charge transport across molecules is required. The studies of charge transport across molecules have created new research fields: molecular electronics and bioelectronics. Some organic molecules were investigated to function as rectifiers [3], memories, amplifiers [4] and single electron transistors [5]. Some biomolecules were operated as rectifiers [6], logical gates [7] and biosensors owing to their highly-specific recognition capabilities which are not accessible by silicon-based components [8].

Molecular electronics is a highly interdisciplinary field and many challenges need to be addressed. The difficulty to employ molecules as functional components includes design and synthesis of molecules with desired functional motifs, modification of biological molecules with tailored functions, miniaturization of electrodes and integration of the molecules into electric circuits. The properties of molecules can be investigated at macroscopic level by electrochemical or spectroscopic methods; however it is generally difficult to study the molecular properties at single molecule level [9]. To measure molecules or other functional components individually, a source and a drain electrode separated by a nanoscale gap are required to contact molecules and form Metal/Molecules/Metal junctions. Most of the simple organic molecules have the dimensions of several nanometers; correspondingly, the contact electrodes are required to have similar sizes as single molecules. The nanoelectrodes can be fabricated by electron beam lithography. However, the finest structures fabricated by state of art electron beam lithography are difficult to reach sub 5 nm; as a result, the sizes of the electrodes fabricated by lithography are usually much larger than the sizes of single molecules. One problem of the nanoelectrodes used for contacting molecules is that large numbers of molecules are assumed to reside between the contact electrodes. When applying a bias voltage on the Metal/Molecules/Metal junctions, the measured current is actually a sum of current through a uncontrolled parallel and/or series circuits of all the involved molecules. Besides, if multiple molecules are packed between the contact electrodes,

the intermolecular transport are also involved in the transport process across the molecular junctions. It would be difficult to exclude this intermolecular transport effect and to reveal the fundamental mechanism of charge transport through single molecules. To this end, it is necessary to fabricate small nanoelectrodes with similar sizes as single molecules. The resolution of e-beam lithography can reach down to 5 nm. However, it is not enough to fabricate nanoelectrodes suitable for contacting single molecules by only e-beam lithography. One reason is that the surface morphology of the nanoelectrodes influences the actual contact area between the electrode and the molecules. Modifying and controlling the morphology of the electrodes become crucial to obtain appropriate electrode/molecule contact configurations. The atomic configurations at the molecule/electrode interfaces also play an important role in the charge transport process, which has already been verified theoretically [10] and experimentally [11]. Controlling the electrode morphology allows to control the Metal/Molecules/Metal interfaces and allows one to investigate electric properties of a single molecule at a specific configuration status.

The first part of this thesis deals with the modifications of nanogap electrodes by electrochemical methods. A electrochemical routine was developed to fabricate nanoelectrodes with controlled needle-like electrode morphology and such nanoelectrodes were employed to contact single molecules. Electrochemical deposition is an appropriate technique for the modifications of surface morphology, since the structure and morphology of electrodeposited materials are determined by electrochemical parameters like overpotential, chemical composition, and concentration of the electrolytes [12]. For instance, the overpotential, which is the potential deviation from the reaction equilibrium potential, determines the transition of the growth mode between isotropic growth and anisotropic growth [13] and results in different surface morphology.

The second part describes a home-made electrochemical mechanical break junction setup. Nanogaps have been implemented by various techniques [14]. Some groups have fabricated nanogaps with fixed gap sizes, using techniques like shadow evaporation [15] and electromigration [16]. Some groups have fabricated nanogaps with tunable gap sizes, such as scanning tunneling microscope (STM) based break junctions [17,18], mechanical controlled break junction [19] and electrodeposition/dissolution technique [20,21]. Tunable nanogaps are more versatile than the fixed nanogaps for investigating the molecule properties, since one can adjust the nanogap to the size of the species or the objects of interest. The capability of adjusting the nanogap size repeatedly also increases the yields of assembling Metal/Molecules/Metal junctions and allows one to investigate the influence of the gap size on the electric response of molecular junctions.

STM based break junctions and mechanical controlled break junction are among the most widely used methods of generating nanogaps. The basic principle of a mechanical

break junction setup is to break a narrow connection between two electrodes which are fixed on a substrate [22, 23]. The electrodes are usually fabricated by optical or electron beam lithography. By applying a mechanical force on the substrate, the substrate bends and the bridge elongates. The thinnest portion of the narrow connection breaks apart, and a nanogap is formed between the two facing electrodes. For the measurements of biomolecules, measurements in aqueous condition are necessary to maintain structural integrity and functionality. Aqueous conditions are also required for the investigation of redox molecules, where an electrochemical gating electrode is used to modulate the electron transport process by controlling their electrochemical potentials. Although various routines of fabricating nanogaps were proposed, not many methods are available for fabricating tunable nanogaps in aqueous conditions. The STM based mechanical break junction with additional electrochemical control has the ability to measure molecules in liquid. Many redox molecules and biomolecules were investigated successfully by STM based methods [6, 24]. Another approach to measure molecules in liquid is to integrate an electrochemical cell to mechanical break junction setup, forming an electrochemical mechanical break junction [25–28]. However, to add an electrochemical cell to the conventional mechanical break junction setup is not straightforward. The bending of the substrate (several millimeters of displacement) would induce many irregular holes and cracks in insulating layer (especially for commonly used stiff dielectric materials like SiO_x/SiN_x). These cracks would create large and unpredictable parasitic leakage currents at the liquid/electrode interface when the electrolyte penetrates through the insulating layer. This parasitic electrochemical leakage current would then interfere with the tunneling current across the Metal/Molecules/Metal junctions. The detailed characterization and optimization of the setup from the electrochemical aspects are still absent and the influence of the electrochemical leakage currents at the substrate/liquid interface during the opening/closing process is still unclear. In this work, several modifications were made to optimize a mechanical controllable break junction setup for the use in liquid. The leakage currents at the substrate/liquid interfaces were also characterized by electrochemical methods.

The third part summarizes the investigation of intermolecular charge transport across electrostatic interfaces. Once the appropriate mechanical break junction setup with an electrochemical cell is successfully tested, the charge transport across single molecules can be measured on such setup. In this work, we focus on the intermolecular charge transport since the intermolecular charge transport is widely involved in the biological process and is of fundamental importance to understand the energy metabolisms in biological systems.

Electron transfer reactions between proteins are widely involved in many biological processes ranging from photosynthesis to aerobic respiration [29, 30]. The intermolecular electron transfer between proteins depends on the proper alignment of their binding sites. The

formation of protein complex often involves an encounter complex, which is mainly dominated by electrostatic interactions [31]. For example, the biomolecular electron shuttle cytochrome *c* is guided via a positively charged lysine rich domain to its native binding partners (exposing negatively charged patches) cytochrome *bc*1 and cytochrome *c* oxidase of the respiratory chain to facilitate a facile charge transfer across the formed electrostatic interface. Electrostatic binding motifs are also employed for the assembling of nanoparticles and nanotube based nanohybrids or their immobilization on various substrates, creating functional surface for sensor or electronic applications [32]. In such systems, electron transport across electrostatically bridged molecules is of critical importance for the performance of the final devices. In recent years, the size of engineered devices has approached the dimensions of few or even single molecules and the charge transport within these systems can be investigated. For instance, mechanical break junctions are well established tools, where individual molecules can be incorporated between two nanoelectrodes, forming Metal/Molecules/Metal junctions [9,33]. Such molecular junctions can be reproducibly formed or broken by mechanical control and the conductance of single molecular junction can be retrieved [11]. The conductance of the molecular junctions depends on the intrinsic electrical properties of the molecules and their molecule/metal interface. Model molecules like single ring aromatic compounds or alkanes with terminal dithiol [34], diamines [35], diisothiocyanate [36], and dicarboxylic-acid groups [37] were systematically studied by several research groups and the contribution of metal/molecule bonds to the electron transport pathway was discussed. More complex single molecules like fullerene [38], aniline oligomer [39], transition metal complexes [40] and DNA molecules [28] have also been investigated and the observed electron transport was related to sizes of the molecules, electrode coupling, their electronic structures and environments. If intermolecular electron transport is investigated, also the interfaces between the involved molecules need to be considered. Wu et al. investigated electron transport through an aromatic interface by comparing the electron transport of a single molecule with two coupled aromatic molecules bridging a nanoelectrode junction [41]. Electron transport properties across nucleoside interconnected by hydrogen bonds were studied by Chang et al. and a relation between nucleoside sequences and electrical properties was revealed [42].

The third objective of this thesis is to investigate the intermolecular electron transport across a molecular junction containing two electrostatic interfaces. Since the protein molecules are too complex for current studies, single model organic molecules are used in this work. By careful designing the experiments, molecular junctions based on intermolecular electrostatic coupling were assembled and the charge transport through the electrostatic interfaces was investigated.

2. Fundamentals

Because of the interdisciplinary nature of this thesis the fundamentals have to cover a broad range of topics and can only give a brief overview of the required basics. In the first part, the electron transport theories in nanometer scale structures are described. The second part deals with the basics of electrochemistry.

2.1. Electron transport in nanometer scale

When the size of a solid in at least one dimension is less than 100 nanometers ($1\,\mathrm{nm} = 10^{-9}\,\mathrm{m}$), the properties of the solid become different from the properties of the solid in bulk size. The electron transport property is one of those properties, which is greatly altered if the size of the conductor goes into nanoscale [43]. A fundamental difference between nanoscale objects and bulk materials is that quantum mechanics becomes the dominant mechanisms and determines many unique properties observed in the nanoscale objects. One novel phenomenon is that ballistic transport substitutes the electron scattering mechanism in nanoscale conductors. Owing to ballistic transport, the conductance of metal nanowire does not obey Ohm's law any more if the width of the metal wire decreases to a few nanometers and the conductance is quantized in such nanoscale systems [44]. Another phenomenon observed in the nanoscale world is electron tunneling. Electron tunneling is widely observed that the electrons are not totally blocked by a potential barrier but tunnel through the potential barrier [45]. The tunneling current between a nanoscale gap formed by two facing conducting electrodes can be measured by state of art measuring instruments. This tunneling current is the basis of electron tunneling microscopy which is one of the most important inventions in the 20th century. One motivation to study the transport properties in nanoscale comes from the developing semiconductor industry. With continuing downscale of silicon based electronic components, understanding the electron transport behavior in the nanoscale material is of increasing importance than ever since new organic/inorganic materials are brought into the public for fabricating transistors with better performance or lower cost [46]. The electron transport properties are vital to utilize new functional materials as substitutes to the silicon-based electric components or to

employ new functions to the current devices.

In the first section, the general theory of electron transport properties at the nanoscale is described. Firstly, the free electron gas model and Landauer theory [47] is introduced and then these theories are employed to describe quantized conductance. Secondly, the general quantum mechanical description of electron tunneling through a potential barrier is discussed, which is the basis to understanding the tunneling of electrons through nanoscale gaps and molecular junctions. Finally, a description of electron transport characteristics through nanoscale objects including single molecules will be given.

2.1.1. Atomic scale junctions and conductance quantization

When an electric field is applied on a bulk metal, the electrons move under the force $F = -eE$. If the size of a conductor is much larger than the mean free path of the electrons, the moving electrons collide with the impurities, lattice imperfections, or the phonons. These collisions are summarized as the electron scattering process [48]. The electric current density is given by Ohm's law:

$$j = \frac{ne^2\tau E}{m} \tag{2.1}$$

where j is the current density, n is the number of electrons, τ is the collision time, E is the strength of electric field and m is are the electron mass.

The electrical conductivity is defined by $\sigma = j/E$, thus

$$\sigma = \frac{ne^2\tau}{m} \tag{2.2}$$

For a cylinder conductor, the conductance G is:

$$G = \frac{l}{s}\sigma \tag{2.3}$$

where σ is the conductivity of the material, l is the conductor length, s is the area of the cross section of the conductor.

The Ohm's law fails when the size of the conductor decreases to nanoscale. For instance, in one-dimensional nanowires, each scatterer contributes almost equally to the wire resistance, and the resistance is proportional to the cross section [49]. For an atomic-sized Pt and Nb conductor, the conductance was observed with reproducible jumps in the order of $2e^2/h$ when changing the constriction radius of the atomic-sized conductor [50].

The investigation of atomic-sized conductors was carried out shortly after the STM was invented in 1986. Gimzewski and Möller were the first to employ an STM to study the conductance in atomic-sized conductors and they found a transition between contact and

vacuum tunneling at a resistance of about 20 kΩ [51]. The first experimental observation of quantized conductance was realized on a quasi one dimensional channel of 2D electron gas formed in GaAs/AlGaAs heterostructures [44, 52]. The study of atomic-sized conductors surged in the beginning of nineties that was mostly attributed to the seminal works of Muller, van Ruitenbeek and de Jongh, who introduced a mechanical controllable break junction (MCBJ) that can create atomic-sized connections reproducibly [50, 53, 54]. After that, the quantized conductance were observed by different groups using various methods [55–57].

Scanning tunneling microscope and mechanical break junction experiment are two of the tools that can measure quantized conductance. Both methods have the capability to create atomic point contact configurations. The STM creates an atomic point contact by crashing the gold tip into a metal surface and retracting the gold tip. The MCBJ setup creates atomic point contact by breaking a thin metal nanowire fixed on a flexible material. By applying a mechanical force on the substrate, the substrate bents and the bridge elongates. The thinnest portion of the bridge breaks apart, and a nanogap between the two facing electrodes is formed. By analyzing the histograms of the conductance traces recorded during the process of breaking and closing the point contact, quantized conductance can be revealed in the conductance histograms.

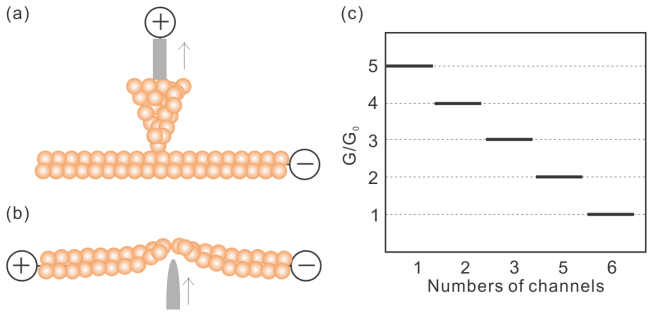

Figure 2.1.: Schematic of atomic point contacts formed by STM (a) and mechanical controlled break junction (b). The quantized conductance decreases when the size of the constriction gets smaller and the allowed number of channels decreases (c).

The theoretical descriptions of the quantized conductance in atomic-sized conductors were not clear at first. Some people believe this phenomenon should be interpreted in the quantum framework [58], but others think it is mainly due to the atomic rearrangements [59]. Many more results were published with a wide variety of metals under various conditions and the basic conductance quantum was found different in different materials. This fact can not be interpreted in terms of free electron gas inside a constrained space. A breakthrough in understanding the quantized conductance was made when the I-V curves were obtained on aluminum single-atom contacts [60]. It was found that for

aluminum single-atom contacts, three channels were involved in the transport, with transmission probabilities for each channel less than 1. This result agrees with the first principles calculation, where the conductance is discussed in terms of 'resonances' in local density states [61], which means that the quantized conductance is better interpreted by the chemical structure of atoms than by simple free electron plane wave model.

However, the simple free electron model is still valid to interpret the quantized conductance if the we restrict ourselves to monovalent metals such as gold and sodium. Since gold is the only material we used in this work, we will introduce the simple free electron gas model to interpret the quantized conductance.

Free electron gas model

The electrons in metals can be seen as a free electron gas, which is usually referred to as free electron model [62, 63]. In this model, the valence electrons of the constituent atoms become conduction electrons and they can move freely through the volume of the metal.

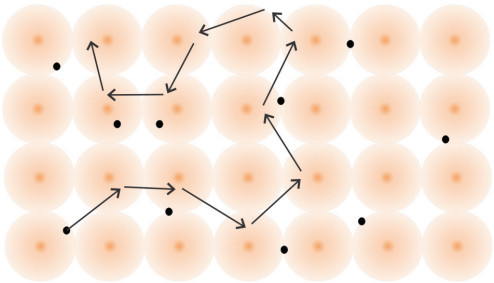

Figure 2.2.: The free electron gas model: conduction electrons (black dots) move around in the metal conductor and scatter at impurities, lattice imperfection and the phonons.

The Schrödinger equation of free electron gas is:

$$H\Psi_n = \varepsilon\Psi_n \tag{2.4}$$

where Ψ is the wave function, H is the Hamiltonian operator, ε is the energy of eigenstates.

In the free electron gas model, the solution of the Schrödinger equation is a set of plane waves with discrete energy levels. The wave functions of the electrons $\Psi_n(x)$ are in the form of

$$\Psi_n(x) = A\sin\left(\frac{2\pi}{\lambda}x\right) \tag{2.5}$$

Where λ is the wavelength of the energy state n.

By solving the Schrödinger equation, the energy of the electrons can be obtained:

$$\varepsilon = \frac{\hbar^2 k^2}{2m} \tag{2.6}$$

where ε is the electron energy and k is the wave number.

Free electrons in a quantum well

If the size of the conductor decreases to nanoscale, the movement of the electrons are confined between the boundaries. The effect of the boundaries of the object can be seen as a potential step. The height of this potential step is the energy difference between the Fermi level of the metal and the energy level in vacuum (The Fermi energy E_F is defined as the energy of topmost filled level in the ground states of the N electron system). This energy difference is referred to as the work function and can be determined by the photoelectric effect [64]. The confined system is mathematically described as electrons in a potential well and analyzed by the Schrödinger equation. The solution of the Schrödinger equation of a quantum well is also a set of plane waves with discrete energy levels as shown in Fig. 2.3.

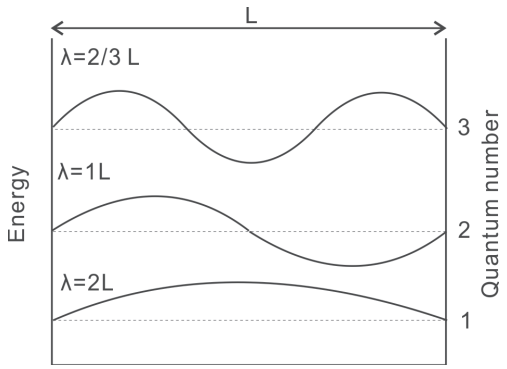

Figure 2.3.: Energy states of electrons confined in a potential well of width L. The larger the size of the constriction is, the more energy states can be allowed

These plane waves are referred to as modes or channels since electrons in a potential well must stay at one of those channels. One mode corresponds to one plane wave with specific wave number, thus the modes can be noted by this wave number. The number of quantum modes allowed in the quantum well is decided by the size and geometry of the constriction. If the size of the restriction is increased, more modes with increasing energy can be accommodated in the constriction. In the case of nanowires, the sizes are in the nanoscale in x and y dimensions but in the micrometer scale or larger in z scale, thus the energies states are quantized in x and y dimensions and the total energy is given by

$$\varepsilon = \varepsilon_{i,j} + \frac{\hbar^2 k^2}{2m} \tag{2.7}$$

Where i, j are the quantum numbers labeling the eigenstates in the x, y dimensions. k is the wave vector in the direction of motion.

Note that this ground energy is the energy at temperature of absolute zero. If the temperature is increased, the Fermi-Dirac distribution needs to be considered which describes the probability of a state occupied by an ideal electron gas in thermal equilibrium.

Atomic scale junctions and quantized conductance

The discrete energy states of electrons in confined systems would alter the electron transport behavior greatly since those electrons can only tunnel through these limited channels. The available channels are limited by the size of constriction. Therefore, the nanoscale conductor has a finite current-carrying capacity for a given voltage applied across its ends.

If the size of the conductor is decreased to the same order as the electron wavelength, the electrons directly transport through the conductor without collision with the phonons. This process is referred to as ballistic transport. If the electrons transport through ballistic movement, the conductance of the nanoscale conductor will be quantized due to the discrete properties of allowed transport channels [44]. To observe the quantized conductance, the size of the conductor needs to be decreased to the similar sizes as the Fermi wavelength of the electrons. For gold, the Fermi wavelength of the electrons is 0.5 nm [65], which is comparable to the size of one gold atom. The one atom constriction can be realized in an atomic point contact configuration where one or several gold atoms are contacted by a pair of nanoelectrodes. The pair of nanoelectrodes is usually over 100 nm in width which is much larger than the size of the Fermi wavelength, so that it can be simply considered as electron reservoirs. The leads connecting the atomic point contact to the electron reservoirs are constricted to several nanometers and the electron wave functions in the leads are quantized to a set of discrete states. The lowest energy level of the allowed mode can be calculated as $\frac{\hbar^2 k^2}{2m}$ (Eq. 2.6), where L is the width of the smallest constriction (3 Å at atomic point contact). This lowest energy channel is lower than the Fermi energy of the electron in gold electrodes.

In an nanoscale constriction, suppose there are N and M energy states allowed in the left and right leads, respectively. If one electron transports from the i mode on one side to the j mode of the other side at a small bias $eV = E_F$ applied on the atomic point contact, the conductance for transporting through one channel is only the ratio of fundamental constants:

$$G_0 = 2\frac{e^2}{h} \tag{2.8}$$

Where G_0 is the universal quantum of conductance with the value $G_0^{-1} = 12.9\,k\Omega$. The prefactor 2 in the equation comes from the degeneracy of spin up and down and is absent

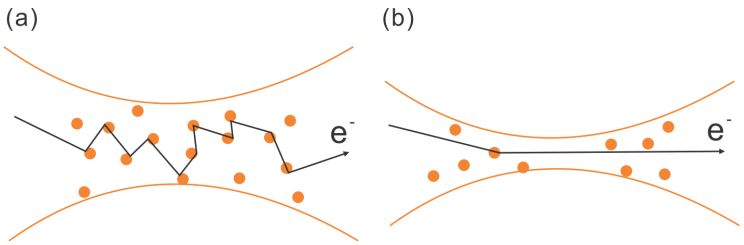

Figure 2.4.: Ballistic transport occurs if the size of conductor is decreased to the similar size as Fermi wavelength of electrons. (a) The electrons scatter at defects. (b) The electrons directly transport through the constriction without collision.

for magnetic material. If imperfect transport is considered, the transmission amplitude $T(E_F)$ is introduced.

$$G = 2\frac{e^2}{h}T(E_F) \tag{2.9}$$

If more channels are involved in the ballistic transport, the conductance is in the form of:

$$G = 2\frac{e^2}{h}\sum_{i,j} T_{i,j}(E_F) \tag{2.10}$$

This equation is the Landauer Formula and $T_{i,j}(E_F)$ is the probability that an electron from the source electrode in transmission mode i is transmitted to the drain electrode into a different mode j.

Note that the elastic scattering occurs exclusively at the walls forming the boundary of the system and scattering of electrons mainly change the spin and phase of the electron wave function, thus the contribution of the scattering to the conductance can be neglected, that means $T(E_F) \leq 1$.

Since the effect of scattering is negligible only diagonal terms remain in Eq. 2.10, the conductance through a channel of n modes is given by [66]:

$$G = nG_0 \tag{2.11}$$

This means that the conductance of atomic point contact is multiple times of the universal quantum of conductance G_0. The number of modes involved in the transmission increases with the transverse size of the constriction, therefore the quantized conductance cannot be observed if the size of constriction is much larger than the atomic point contact scale.

Another requirement for observing the quantized conductance in room temperature is that the difference in energy between the ground state and the next available state should

be large enough to be recorded [22]. Otherwise, the thermodynamic energy will disturb the energy state of the electrons. For gold, this energy gap between the ground state and the next available state is about 1 eV at room temperature (Eq. 2.6), so that the quantized conductance in gold atomic point contact configuration can be observed at room temperature. For semiconductor materials (2D electron gas), the electron wavelength is in the order of a few tens of nanometer at room temperature and energy difference between the transverse modes is in the order of 1 meV, thus the quantized conductance can be only observed at low temperature.

2.1.2. Electron tunneling through nanogaps

In the previous section, we introduced the electron transport through atomic scale junctions. In the following, we will discuss about how the electrons transport if the atomic scale junctions break into nanogaps. If an atomic scale junction breaks, a nanoscale gap is formed between the broken facing electrodes (in either STM or mechanical break junction). The gap size can be adjusted by a mechanical controlled piezo system. In quantum mechanics, the nanogap between two metallic electrodes is modeled by a square potential barrier with height of Φ_0. If a bias voltage is applied across the gap, this square potential will have a saw tooth shape due to the shifted Fermi energy of the leads. The electrons have small but not zero probability to transport across the potential barrier. This electron transport from the occupied electronic states of the source electrode to the unoccupied states of the drain electrode is referred to as "tunneling".

Quantum mechanics description of electron tunneling

To determine the tunneling current, the basic idea is to calculate the transparency of the electrons from one end to the other end of the nanogap, which is determined by the wave function of the electrons at either end of the nanogap. The wave function for a free electron has the form:

$$\varphi(x) = \varphi(0)e^{\pm ikx} \tag{2.12}$$

$$k = \frac{\sqrt{2m(\varepsilon_x - \Phi_0)}}{h}$$

Where ε_x is the electron kinetic energy in direction and Φ_0 is the potential barrier.

Considering the Hamilton operator of the electrons:

$$H(x) = -\frac{h^2}{2m}\frac{\partial^2}{\partial x^2} + V(x) \tag{2.13}$$

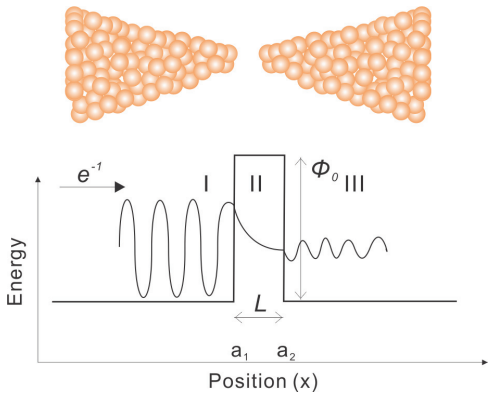

Figure 2.5.: Electron tunneling through a nanogap under a rectangular potential. The size of the nanogap is L, which corresponds to the length of potential barrier. The electrons experience three phases during the tunneling: I, before the potential barrier; II, in the middle of potential barrier: III, after the potential barrier.

Where the $V(x)$ is the barrier potential. Then the Schrödinger equation of electrons facing a barrier is:

$$-\frac{h^2}{2m}\frac{\partial^2\varphi(x)}{\partial x^2}+V(x)\cdot\varphi(x)=E\cdot\varphi(x) \tag{2.14}$$

The barrier potential $V(x)$ for a rectangular barrier (Fig. 2.5) can be written as a subsection function:

$$V(x)=\begin{cases}\Phi_0, & a_1\le x\le a_2\\ 0, & x<a_1 \text{ or } x>a_2\end{cases} \tag{2.15}$$

Thus, the potential can be divided into three parts: before the barrier (I), in the barrier (II) and after the barrier (III). The Schrödinger equation can be expressed in three parts.

For the region (I) and (III):

The potential is zero, so the Schrödinger equation is:

$$\frac{\partial^2\varphi(x)}{\partial x^2}=-\frac{2mE}{h^2}\cdot\varphi(x) \tag{2.16}$$

The wave function in the region (I) and (III) can be expressed as:

$$\varphi_{I+III}(x)=A\cdot e^{ikx}+B\cdot e^{-ikx} \tag{2.17}$$

$$k=\sqrt{2mE}/h$$

For the region (II), the barrier is Φ_0, the Schrödinger equation is:

$$\frac{\partial^2\varphi(x)}{\partial x^2} = \frac{2m(\Phi_0 - E)}{h^2} \cdot \varphi(x) \tag{2.18}$$

The wave function is:

$$\varphi_{II}(x) = C \cdot e^{i\kappa x} + B \cdot e^{-i\kappa x} \tag{2.19}$$

$$\kappa = \sqrt{2m\Phi_0 - E}/h$$

In the region (I), the wave function is composed of two components: one is the wave function move forwardly, and the other is the wave function that is reflected at the barrier boundary, so, the wave function can be written as:

$$\varphi_I(x) = e^{ikx} + A \cdot e^{-ikx} \tag{2.20}$$

A is the coefficient that can bee seen as the percentage of the wave function that is reflected at the interface.

In the region (III), the only possible wave function is the tunneling wave function, so only forward direction wave function exists.

$$\varphi_{III}(x) = B \cdot e^{i\kappa x} \tag{2.21}$$

In the barrier region, both forwarding and reflecting wave function can coexist, so the wave function takes the form:

$$\varphi_{II}(x) = \alpha \cdot e^{i\kappa x} + \beta \cdot e^{-i\kappa x} \tag{2.22}$$

Solving the Schrödinger equation gives the value of B:

$$B = \frac{2}{1 + \frac{k^2+\kappa^2}{4k^2\kappa^2} \cdot \sinh(\kappa L)} \tag{2.23}$$

As introduced in the beginning of this part, to calculate the tunneling current, the transparency of the electrons from one end to the other end of the nanogap is required. The Eq. 2.23 gives the coefficient of the forwarding wave functions, thus the barrier transparency coefficient $T(\varepsilon_x)$ (Eq. 2.9) is equal to

$$T = \left|B^2\right| \tag{2.24}$$

Simmons equation

Simmons et al. derived a generalized formula for the electron tunneling between similar electrodes separated by a nanogap [67]. This equation permits accurate expressions for both high and low voltages.

$$I(V,L) = \frac{eA}{4\pi^2 hL^2}\left[\left(\Phi_0 - \frac{eV}{2}\right)\exp\left(-L\frac{2\sqrt{2m_e}}{h}\sqrt{\Phi_0 - \frac{eV}{2}}\right)\right. \\ \left. - \left(\Phi_0 + \frac{eV}{2}\right)\exp\left(-L\frac{2\sqrt{2m_e}}{h}\sqrt{\Phi_0 + \frac{eV}{2}}\right)\right] \tag{2.25}$$

Where V is the bias voltage, L is the distance of between the facing nanoelectrodes and α is a constant which is related to the shape of the potential barrier.

At low bias, the equation can be simplified by Taylor series, the resulting equation is:

$$I = \frac{(2m\Phi_0)^{1/2}e^2\alpha}{h^2 L}V\exp\left[-\frac{2(2m)^{1/2}}{h}\alpha(\Phi_0)^{1/2}L\right] \tag{2.26}$$

Further simplified equation is given by:

$$I \approx V\exp\left(-\frac{2L\sqrt{2m_e\Phi_0}}{h}\right) \tag{2.27}$$

This equation shows that the tunneling current decays exponentially with the gap size L at a given bias V. The conductance defined as I/V also decays exponentially with the gap size. A simulated decaying curve of conductance is shown in Fig. 2.6

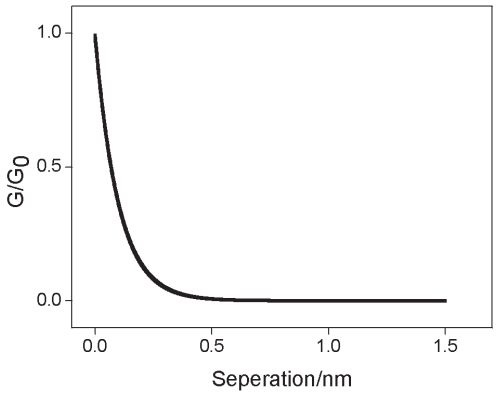

Figure 2.6.: Tunneling current between a nanoscale gap: the conductance decays exponentially with the gap size and decreases to almost zero when the gap size is over 0.5 nm.

At intermediate voltages($V < \varphi_0/e$) , the Simmons equation takes its original form as

Eq. 2.25.

This equation is usually used for fitting the I-V curves of nanogaps at intermediate voltage range to estimate the gap sizes. It should be noted that the I-V curve is nearly linear at small bias ranges, but it takes the "S" shape in the intermediate voltage ranges as shown in Fig. 2.7, which is the curves simulated from the Simmons equation.

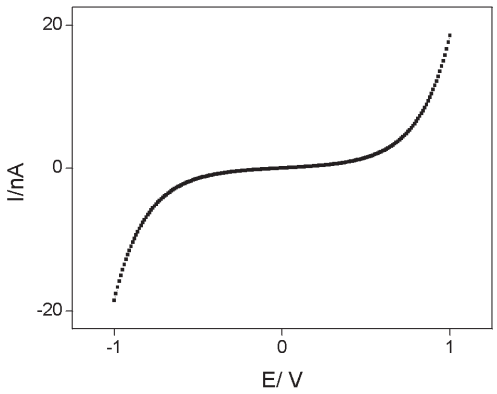

Figure 2.7.: An I-V curve generated from the Simmons equation at potentials from -1 V to +1 V. The curve shows an "S" shape which is characteristic for the curve in tunneling regime.

At high bias, the Simmons equation is simplified as:

$$I \approx V^2 \exp\left(-\frac{4L\sqrt{2m_e\Phi_0^3}}{3hqV}\right) \tag{2.28}$$

which means:

$$\ln\left(\frac{I}{V^2}\right) \approx -\frac{4L\sqrt{2m_e\Phi_0^3}}{3hq} \cdot \left(\frac{1}{V}\right) \tag{2.29}$$

This mode of tunneling is usually referred to as field emission. The transition from tunneling to field emission was observed at metal-molecule-metal junctions [68]. The $\ln\left(\frac{I}{V^2}\right)$ vs. $\left(\frac{1}{V}\right)$ plot, which is known as Fowler Nordheim plot [69], is usually used to identify the field emission transport mechanism.

2.1.3. Electron transport through molecules

In recent years, the size of electrical components is continuously decreasing, new material like molecules are proposed to be used as a substitute to the traditional silicon based components or provide new functionality for the conventional electronics devices. The silicon based electric components already reached the feature size of 65 nm in the year of

2000. The molecules have the feature size of about several nanometers, and some molecules exhibit similar functions as silicon based components. More importantly, the molecule based devices exhibit new functions that are not available on silicon based components. The biomolecules are of special interests since the protein structures have evolved over very long time and unique properties are developed. For example, a series of proteins are involved in the respiratory systems of plant cells, and transfer electrons across the membrane of mitochondrion. Studying the charge transport through molecules traces back to work in 1949, when the conduction in proteins was investigated [70]. Carter et al. introduced the fabrication methods in the molecular level that can accomplish molecular devices [71]. Recent progress of using molecules to realize electric function was described in the work of Liu et al. [6], where gold electrodes were modified by redox mediator microperoxidase-11 (MP-11), which is the heme-containing domain of the biological electron shuttle cytochrome c . In such system, electrochemical rectification of a redox current transferred between redox probes (ferricyanide) in solution and a gold electrode functionalized with the biomolecules (MP-11) was achieved.

The major difference between molecules and semiconductor materials is their electronic structures. Semiconductors are characterized by the existence of a quasi-continuum of states near the Fermi level. On the contrary, the energy states of molecules are discrete.

HOMO-LUMO of molecules

Compared to the band gap theory which describe electronic structures of semiconductor materials, two terms are often used to describe the electronic states of molecules: the occupied states and the non-occupied states. The highest occupied molecular orbitals (HOMO) and the lowest unoccupied molecular orbitals (LUMO) are especially of interest since they are related to measurable current and the electronic transport.

The HOMO-LUMO can be estimated by linear combination of atomic orbitals calculation (LCAO). For example, a gold quantum dot of 20 atoms has a HOMO-LUMO gap of 1 eV and the gap is 2 eV for a cluster of 10 atoms [72]. For organic molecules, the HOMO-LUMO gap depends on their chemical structures. Alkane molecules usually have large HOMO-LUMO gaps over 6 eV and are almost insulating [73]. Conjugated molecules like poly-paraphenylene have HOMO-LUMO gaps of 2–4 eV and behave like ordinary semiconductors [74, 75]. HOMO-LUMO energy gaps can be investigated experimentally by the I-V curves of the molecules. Current is observed to be suppressed when the voltage across the molecules is smaller than the barrier. The barrier is defined by the distance between the Fermi energy and the HOMO/LUMO energy.

For organic molecules, the HOMO-LUMO gaps are generally larger than the metallic quantum dot so that I-V curves have different shape compared with the metal quan-

tum dot. However, the HOMO-LUMO gaps of molecules are determined not only by the molecules themselves but also by the contact configuration to the metal leads and the micro environment of the molecules. It was observed in the photoemission spectroscopy and single molecule I-V curves that the effective HOMO-LUMO gap of molecules coupled to a metal surface can be significantly smaller than the HOMO-LUMO gap of the isolated molecules [5, 76].

Noncoherent tunneling

In a configuration that a single molecule is incorporated between two electrodes, the interface between the molecules and the electrode affects the electron transport mechanism greatly. If the coupling between molecules and the metal electrodes is weak, the coupling can be treated as perturbation to molecules and the leads.

$$H = H_0 + V \tag{2.30}$$

Where H_0 represents the uncoupled electrodes and molecules and V is coupling between them.

Then the transparency coefficient across the molecular junctions is:

$$|T(E)|^2 = |\langle i|H|f\rangle|^2 \tag{2.31}$$

Where i, f are states of lead and molecules responsible for conduction and H is the Hamiltonian of the total system.

In this system, the influence of the coupling to the energy states is negligible. The molecular orbitals in the system are localized and very close to those of the isolated molecules. As a consequence, the electron transport through the weakly coupled molecular junctions is a sequentially two-step process: firstly, the electrons pass to the molecules and reside on the molecules, the molecules are charged; secondly, the electrons tunnel from the molecule to the electrodes and the molecules are successively discharged. This type of transport with two steps is called noncoherent tunneling as illustrated in Fig. 2.8.

According to Markus theory [77], when the electrons fill a molecular orbital, the energy level of the molecules will be shifted and the system is reorganized to minimize the total energy level. The energy needed to make the reorganization of molecules is called reorganization energy (Fig. 2.9).

In the noncoherent tunneling, the molecules are charged when accepting electrons and discharged when donating electrons. According to the Marcus theory, there is a difference between the energy of the reactants and the energy of the products ΔG. However, the reactants cannot turn into the products spontaneously, they need to overcome the activation

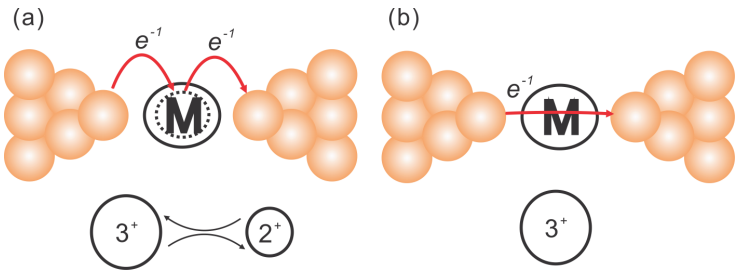

Figure 2.8.: (a), Noncoherent tunneling, the coupling between the molecules and the electrode is weak and the electrons firstly transport to the molecules, then transport to the other electrode. During this process, the molecules experience charge and discharge. (b), Coherent tunneling, the coupling between molecules and electrodes is strong and the electrons tunnel directly through the molecules without changing the status of the molecules.

energy ΔE. The reorganization energy λ is the energy required to allow the reactants to make a rearrangement to have the same nuclear configuration as the products when an electron resides on the molecules.

The rate constant k of the reaction is given by:

$$k = A \exp\left(\frac{-\Delta G}{k_B T}\right) \tag{2.32}$$

$$\Delta G = \frac{\lambda}{4}\left(1 + \frac{\Delta G^0}{\lambda}\right)^2$$

The constant A represents the nature of the electron transfer reaction (intra or intermolecular transfer). It can be seen from the above equation that the reorganization energy λ has an influence to the charge transfer rates and the higher the reorganization energy λ is, the smaller the rate constant would be.

Coherent tunneling

If the coupling between the molecules and the electrode is strong, the electrons in either molecules or the electrodes will be delocalized and the electron tunneling is one step process [78]. In this case, the interaction between the tunneling electrons and the electrons occupying lower states of the molecules is also small. This type of transport is called coherent tunneling. In coherent tunneling, the tunneling time through the molecules is much smaller than the time needed in noncoherent tunneling, since the molecules are not charged or discharged during the electron transport process.

In coherent tunneling the current calculates as [79]:

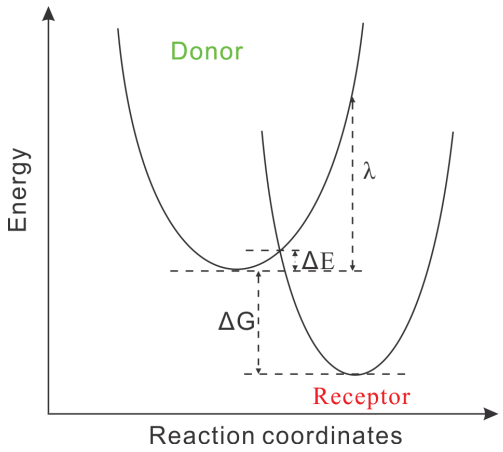

Figure 2.9.: According to the Marcus theory, the molecules experience energy changes when accepting or donating electrons. The reaction does not occur spontaneously, but activation energy ΔE must be overcome.

$$I = \frac{e^2}{\pi h} \int_{-\infty}^{+\infty} T(E,V) \left[f(E-\mu_1) - f(E-\mu_2) \right] dE \tag{2.33}$$

$$\mu_2 = \varepsilon_F + (1-\eta)eV$$

$$\mu_1 = \varepsilon_F - \eta eV$$

Where $T(E,V)$ is the effective transparency, $\mu_{1,2}$ is the chemical potential of the electrode, η is a parameter used to describe the strength of coupling between the molecule and the electrodes and $f(\varepsilon)$ is the Fermi function at the temperature of the experiment.

From this equation, it can be concluded that the current depends on three factors: the overlap between the orbitals of the metal electrodes and the molecules, the localization of the molecular orbital and the symmetry between the two metal/molecule contacts.

2.2. Electrochemistry

In this part, some basic concepts of electrochemistry are introduced. When isolated compounds with different redox potentials come into contact, they can exchange electrons. Electrochemistry studies the electron transfer reactions at the interfaces. The electron losing process is referred to as oxidation and the flow of electrons out of the species is anodic current. On the other hand, the electron harvesting process is called reduction and the flow of electrons into the species is cathodic current. The field of electrochemistry covers many

phenomena including electrodeposition or etching, electrochemical sensors and fuel cells. In this thesis, two main subjects of electrochemistry are related: one is utilizing electrochemical deposition/etching to fabricate nanoscale gaps; the other is investigating the charge transport across molecules on a self assembled monolayer and across single molecules in electrochemical environment.

The introduction of fundamental electrochemistry follows the textbook of Bard et al. [80].

2.2.1. Electrochemical interface

Gouy-Chapman-Stern model

The simplest electrochemical system is the half cell which contains a conductive electrode and a surrounding conductive electrolyte. The basic electrochemical process is the charge transfer between the metal electrode and the dissolved electroactive species. For instance, a zinc electrode immersed in pure water forms a half cell. The zinc atoms will dissolve into the water and leave the negative charged electrons at the zinc electrode. At the same time, the positive zinc ions will accumulate at the zinc/water interface. The accumulated opposite charges will generate an electric field which will hinder further zinc atom dissolving and finally a thermodynamic balance is reached. This solid/liquid interfaces consisting of two phases of charges are know as the electric double layers. According to the Gouy-Chapman-Stern model [81], the inner layer of the electric double layer is the adsorbed charged water molecules and ions (Stern layer). The outer layer is the diffusion region which gradually balances the opposite charges to electroneutrality (Gouy-Chapman layer). In the case of flat surface and symmetrical electrolyte, the relationship between the electric charge σ and the Stern potential ϕ is given by:

$$\sigma = \sqrt{8\kappa T \varepsilon_0 \varepsilon n} \sinh \frac{ze\phi}{2\kappa T} \tag{2.34}$$

Where κ is Boltzmann constant, σ is the charge density, T is absolute temperature, ε_0 is dielectric constant and ε is the electrostatic potential.

For dilute solutions at room temperature, the charge density can be evaluated by:

$$\sigma = \sqrt{11.7C} \sinh(19.5z\phi) \tag{2.35}$$

Where C is the concentration in mol/L.

The capacitance of the double layer is given by:

$$\frac{1}{C_d} = \frac{x_2}{\varepsilon\varepsilon_0} + \frac{1}{(2\varepsilon\varepsilon_0 z^2 e^2 n/\kappa T)^{1/2} \cosh(ze\phi/2\kappa T)} \tag{2.36}$$

Where C_d is the double layer capacitance and x_2 is the position of centers of the ions.

The potential generated by the opposite charges at the electric double layer is related to the thermodynamics and the kinetics of electrode reactions. Controlling the potential across the double layer affords an important way to manipulate the charge transfer reactions. On the other hand, measuring the potential and current across the double layer can gain the information of the electrode reactions.

Electrochemical cell

Directly measuring the potential across the electric double layer is not possible. Contacting a metal electrode is simple, but connecting the other lead to the solution site will inevitably introduce another solid/liquid interface and the interface potential. Therefore, a basic measurable electrochemical cell includes at least two half cells. In most electrochemical experiments, only one half cell is of the research interest and it is the common practice to employ a reference electrode as the other half cell. One example of reference electrode is the Ag/AgCl electrode, which usually takes the form of a piece of silver wire coated with silver chloride and immersed into saturated potassium chloride solution. The potential across the Ag/AgCl interface is very accurately determined against the hydrogen half cell. The latter is actually a platinum wire surrounded by hydrogen gas and the potential of hydrogen half cell is defined as zero.

A typical electrochemical cell includes three electrodes: working electrode (WE), reference electrode (RE) and counter electrode (CE). All the electrodes are immersed in a solution and the potential difference between the electrodes are controlled by an external power supply (a potentiostat). The reference electrode has very high impedance and the current flowing through the reference electrode is negligible. Hence, the potential difference between the working electrode and reference electrode can be monitored. The counter electrode has low impedance and the current is applied between the counter electrode and working electrode. Adjustable resistor is connected to the counter electrode and can be varied according to changes of current. By this way, the potential applied on the cell can be controlled.

2.2.2. Standard electrode potential and Nernst equation

The potentials of many electrode reactions have been measured at standard conditions: the effective concentration of solutes is 1 M, gases are at a pressure of 1 bar and temperature is at 25 °C. Such potentials measured at standard conditions are called standard electrode potentials E^0.

If the concentration and gas pressure are not of the standard values, the relation between the potential and the concentration is given by the Nernst equation [80].

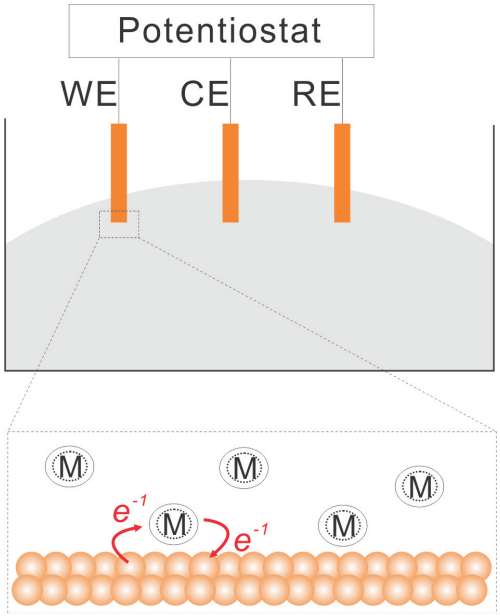

Figure 2.10.: Typical electrochemical setup that include working electrode, counter electrode and reference electrode. The electrochemical reactions of interest occur at the working electrode.

In a system where all associated chemical reactions are much faster than the mass transfer processes and the reaction is reversible:

$$O + ne \rightleftharpoons R \tag{2.37}$$

The reactive species in the equilibrium reaction follows Nernst equation:

$$E_i = E^0 - \frac{RT}{nF} \cdot \ln \frac{C_R}{C_O} \tag{2.38}$$

where R is the gas constant, T the temperature, n the valence of the ion, F the Faraday constant, and $C_{R/O}$ are the respective ion concentrations.

The Nernst equation is more commonly written in base 10 log form rather than natural logarithms and for 25 °C:

$$E_i = E^0 - \frac{0.59}{n} \cdot \log \frac{C_R}{C_O} \tag{2.39}$$

This simple equation shows that a half-cell potential will change by 59 mV if the concentration of a substance involved in a one electron redox process changes by a order of 10.

Since the redox reaction includes the losing and gaining electrons, many reactions involve the hydrogen ions. Therefore, the potentials given by Nernst equation vary with the pH value.

2.2.3. Faradaic current and nonfaradaic current

The current at the electrode/liquid interface can be recorded against the applied potentials. Such curves can provide information of the properties of the interface and the nature of the solution. Interpreting the rate of an electrochemical reaction is often very complex since it is a heterogeneous reaction and two types of currents are involved in the process.

The first type of current is caused by the charge transfer between the electrode and the electroactive species. The electron exchange redox reaction is affected by the reaction kinetic variables. Such current is governed by Faraday's law and referred as to Faradaic processes.

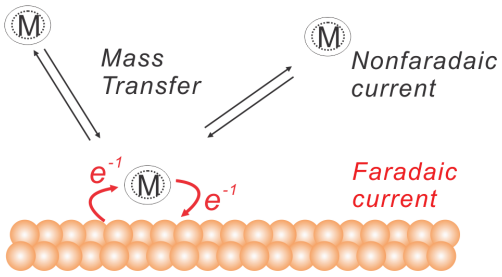

Figure 2.11.: Faradaic and nonfaradaic current in an electrochemical cell

The number of the electrons that cross the interface in Faradaic current is determined by the extent of the chemical reaction and the number of electrons can be measured by integrating the current. The relationship between the total charge and the amount of product formed is given by Faraday's law.

$$m = \left(\frac{Q}{F}\right)\left(\frac{M}{Z}\right) \tag{2.40}$$

Where M is the mass of the substance generated at an electrode, Q is the total electric charge passed through the substance, F is the Faraday constant and Z is the valence number of the substance.

From this equation, it is known that the passage of 96.385 C of electrons is equivalent to consumption of 1 mole reactants or 1 mole of products in a one-electron reaction.

Butler-Volmer equation

When the current is solely controlled by the rate of electrochemical charge transfer process, the current-potential relationship is described by the Butler-Volmer equation [80]:

$$I = Ai_0 \left\{ \exp\left[\frac{(1-\alpha)nF}{RT}(E - E_{eq})\right] - \exp\left[-\frac{anF}{RT}(E - E_{eq})\right]\right\} \tag{2.41}$$

Where I is the electrode current, i_0 is the current density, E is the electrode potential, E_{eq} is the equilibrium potential, A is the electrode active surface area, T is the absolute temperature, n is the number of electrons involved in the electrode reaction, F is the Faraday constant, R is the universal gas constant and α is the dimensionless symmetry factor.

For a specific electrochemical cell, a defined equilibrium potential is established which can be used as the reference of the system. The difference of the electrode potential from the equilibrium value is called overpotential η . In the Butler-Volmer equation $\eta = E - E_{eq}$.

At the low overpotential region, the Butler-Volmer equation simplifies to:

$$i = i_0 \frac{nF}{RT}(E - E_{eq}) \tag{2.42}$$

At the high overpotential region ($E > 0.1\,V$), the second term of the equation becomes negligible. Hence, exponential relationships between current and over potentials are obtained in the form of:

$$\eta = a + b \log i \tag{2.43}$$

Where a, b are the characteristic constants of the electrode system.

This theoretical results coincide with the experimental Tafel lines which describe the linear relationship between the overpotential and the log current density. The slope of the Tafel plot reveals the value of the transfer coefficient for the given experimental conditions.

The second type of current is related to the mass transport process of the electroactive species because that the reactive species need to be transferred to the electrode surface before any charge transfer at interface. This process is affected by the mass transfer variables and various surface effects. Under particular circumstances, no charge transfer reactions occur at the electrode/liquid interface since they are thermodynamically or kinetically unfavorable, but current still can be recorded which is related to the adsorption and desorption of molecules, the charging/discharging effect of the interface, and the mass transport process. This type of current is called nonfaradaic processes.

In a situation where the recorded current is composed of only nonfaradaic current, no charge transfer occurs across the electrode/liquid interface regardless of the applied poten-

tial by the external potential source; this electrode is called an ideal polarizable electrode. In reality, there are no perfect ideal polarizable electrodes but some electrode-solution systems can be seen as ideal polarizability in limited potential ranges. For example, a gold electrode in a diluted sulfuric acid solution approaches an ideal polarizable electrode in the potential range from 0 V to 0.9 V with respect to Ag/AgCl reference electrode.

Capacitance current

The charging/discharging current is a nonfaradaic current which always occurs in the electrochemical cell due to the double layer capacitance. This double layer has the ability to hold a certain amount of electrons. Note this capacitance current is not constant but varies with the applied potentials and the surrounding liquid environment. The structure of the electrical double layer is very complex. One layer of the double layer structure is the specifically adsorbed solvent molecules, and the packed order of the molecules affects the capacitance greatly. By investigating the capacitance current, the internal structural information of the packed molecules can be obtained.

Applying a potential to the ideal polarizable electrode is the typical RC problem. The behavior of capacitance current i with t, when applying a potential step of magnitude E is:

$$i = \frac{E}{R_s} \exp(-t/R_s C_d) \tag{2.44}$$

Where R_s is the resistance, C_d is the capacitance of the electrical double layer.

An often used technique in electrochemistry is the sweeping potential technique, where a voltage ramps or increases linearly with time, starting at some initial value (here assumed to be zero) at a sweep rate v (in V/s). The potential at a certain time is then $E = vt$.

If such a ramping voltage is applied to the RC circuit (ideal polarizable electrode), the capacitance current is:

$$i = vC_d \left[1 - \exp(-t/R_s C_d)\right] \tag{2.45}$$

The current increases from zero to a steady state value vC_d. This steady sate current can be used to estimate the capacitance.

Cottrell equation

Many parameters in the electrochemical cell affect the measurable variables like currents, potentials, or concentrations. These parameters include: the electrode variables (electrode surface area, geometry and surface condition), mass transfer variables (diffusion,

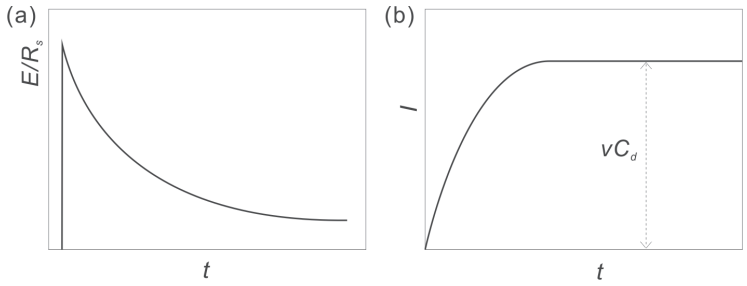

Figure 2.12.: (a) Capacitance current in a potential step. (b) Capacitance current under a sweeping potential.

convection, surface coverage), solution variables (concentration of the electroactive species, electrolyte and pH) and external variables (temperature, pressure).

The modes of the mass transfer affect the measured current greatly. Three modes are involved in the mass transfer processes: migration, diffusion and convection.

The mass transfer obeys the Nernst-Planck equation:

$$J_i(x) = -D_i \frac{\partial C_i(x)}{\partial x} - \frac{z_i F}{RT} D_i C_i \frac{\partial \phi(x)}{\partial x} + c_i v(x) \tag{2.46}$$

Where $J_i(x)$ is the flux of the species i at distance x from the surface, D_i is the diffusion coefficient, $\frac{\partial C_i(x)}{\partial x}$ is the concentration gradient at distance x, $\frac{\partial \phi(x)}{\partial x}$ is the potential gradient, z_i, c_i is the charge and concentration of species and $v(x)$ is the velocity with which a species in solution moves along the axis.

The three terms in the right hand of the equation represent the contribution from diffusion, migration, and convection to the flux, respectively.

Diffusion of ions to the electrode due to the concentration gradient is the most important mass transport process that contributes to the nonfaradaic current. If the current is solely diffusion controlled, solution of the diffusion equation is given by the Cottrell equation:

$$i = nFAc_0\sqrt{\frac{D}{\pi t}} \tag{2.47}$$

By plotting the i vs. $t^{-1/2}$ curve, the diffusion coefficient D can be evaluated. The requirement to use Cottrell equation to evaluate the diffusion coefficient is that the reaction must be diffusion controlled. This Cottrell conditions can be realized when applying a potential step to electrochemical cell. It should be noted that the exponentially decayed charging current will impose on the measured current since there is always a double layer capacitance C_d. Actually, the charging process is the process of establishing the potential step, after about five time constants, the contribution of the charging current can be neglected. Therefore, the data collecting time in the potential step experiment must be

longer than the time constant $R_s C_d$.

2.2.4. Diffusion in nanoscale

Nanoelectrodes found many applications in the electrochemistry, such as, determining the reaction constant [82], detecting epinephrine with a carbon fiber ultramicroelectrode [83] and concentration measurements. The nanoelectrodes are suitable to measure the kinetics of reactions since the diffusion is very fast in the nanoelectrodes compared to the macro electrode.

For macro electrodes, the diffusion of electroactive species is unidirectional diffusion. The size of the ions is much smaller than the size the electrode, and the movement of the ions can be seen parallel. On the contrary, the size of nanoelectrodes is comparable to the size of the ions, thus for ultramirco- and nanoelectrodes, the movement of the ions is radial.

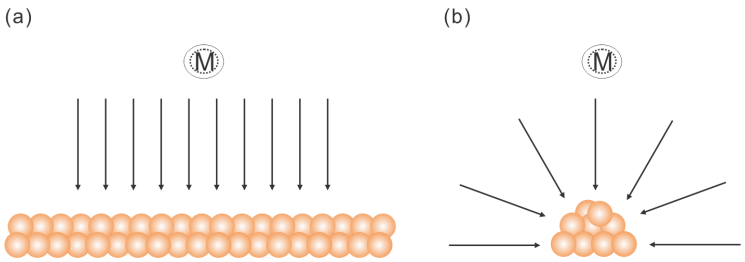

Figure 2.13.: (a) Parallel(unidirectional) diffusion for macro electrodes. (b) Radial diffusion mode for nanoelectrodes.

In cyclic voltammetry, the reaction rate depends on the electron transfer at the electrode and the relationship between electrode current and the potential is described by Butler-Volmer equation. The reaction at the electrode takes place in the Helmholtz layer and with reaction proceeding, molecules are consumed and a concentration gradient develops.

For large electrodes, the geometry of the electrode dose not influence the diffusion and the diffusion can be seen as one dimensional diffusion profile. The one dimensional diffusion equation is given by:

$$\frac{\partial C_0(x,t)}{\partial t} = D_0 \frac{\partial^2 C_0(x,t)}{\partial x^2} \tag{2.48}$$

Solving the equation gives the limiting current for a constant potential:

$$J = \frac{I}{A} = nFC_0\sqrt{\frac{D_0}{\pi t}} \tag{2.49}$$

When sweeping the potential, oxidation begins and current increases. With potential

continually increasing, reaction is accelerated and molecules at the Helmholtz layer are consumed. Finally, the linear diffusion cannot supply enough molecules, and then the current drops and slowly decays to zero. From the diffusion controlled cyclic voltammetry, no steady-state can be observed when macro electrodes are used.

In the case of micro or nanoelectrodes ($r < 25\,\mu m$). The radial diffusion components arise and the radial diffusion is much faster than unidirectional diffusion. The radial diffusion is given by:

$$\frac{\partial C_0(r,t)}{\partial t} = D_0 \left\{ \frac{\partial^2 C_0(r,t)}{\partial r^2} + \frac{2}{r} \cdot \frac{\partial C_0(r,t)}{\partial r} \right\} \tag{2.50}$$

The limiting current for a spherical electrode is given by:

$$J = \frac{I}{A} = nF D_0 C_0 \left[\frac{1}{\sqrt{\pi D_0 t}} + \frac{1}{r_0} \right] \tag{2.51}$$

which is a constant when the time approaches infinity.

This means that in a diffusion controlled cyclic voltammetry using micro or nanoelectrodes, a steady-state current can be reached. The enhanced mass transport for nanoelectrodes decreases the charging and discharging currents, which enable many applications of nanoelectrodes in electrochemistry [84].

2.2.5. Electrochemical deposition

In an electrochemical reaction, if the metal ions are reduced and deposited on the surface of the electrode, this process is referred to as electrodeposition. If the atoms on the electrode surface dissolve into the solution, this process is electrochemical etching. The extent of the completion of the electrodeposition/etching can be described by Nernst equation.

For the reaction:

$$O + ne \rightarrow S(Solid) \tag{2.52}$$

The materials of the electrodes can be either same as the deposited solid, or different inert materials (Au, Pt, for instance). When more than one monolayer of S is deposited on the electrode, the Nernst equation is given by:

$$E = E^0 + \frac{RT}{nF} \ln[\gamma_O C_i (1 - x)] \tag{2.53}$$

Where γ_O is the activity coefficient of species O, and x is the fraction O reduced to S at potential E.

The actual electrode potential applied on the working electrodes determines the direction of the reaction. If the applied potential is more negative than the equilibrium potential,

the metal ions will be reduced and deposited on the electrode. On the other hand, if the applied potential is more negative than the equilibrium potential E^0, the bulk phase of the electrode is etched and the atoms dissolve in the electrolyte. The deposition of atoms and the etching process usually occurs at preferred sites like surface defects, edges and corners, where the lattice atoms are loosely bound to the crystal.

The thermodynamics of crystal growth in electrolyte are similar as those crystal growth properties in vapor conditions. Therefore, the theoretical treatment of crystal growth in electrolyte is similar as in vapor conditions. The properties of the electrolyte are one of the most important factors which affect the metal/liquid interface, the kinetics of the mass transport, the kinetics of charge transfer process and the electron transfer reactions.

In a potential controlled deposition, the depositing current decays exponentially with time and eventually reaches the background current. The i-t relationship is:

$$i(t) = i(0)\exp(-pt) \tag{2.54}$$

Where $i(0)$ is the initial current and the p is analogous to the first-order rate constant.

The total amount of atoms deposited on the electrode can be estimated by the quantity of total electrons $Q(t)$;

$$Q(t) = \int_0^t i(t)\,dt \tag{2.55}$$

If the mass transfer process is slower than the mass transfer process, the actual speed of electrodeposition process is limited by the diffusion process.

The metal ions can be deposited on electrodes of the same material or electrodes of different materials. If the atoms are deposited on a different substrate, the deposition can begin at potentials more positive than the Nernst values where deposition occurs on same materials. This phenomenon is referred to as underpotential deposition (UPD). If the deposition begins at potentials more negative than the Nernst value, this is called overpotential deposition (OPD). The description of UPD is much more complicated than the homogeneous deposition, since the underpotential deposition depends on the substrate and the adsorption of the oxidants. Usually, the deposited atoms will aggregate on the surface and a dendrite morphology will be formed in the underpotential deposition.

Electrodeposition of metals occurs at the liquid/electrode interface and three stages are involved in this process. The first step is the formation of metal adatoms on the electrode surface; the material of the electrode is either the same as the deposited adatoms or different from the deposited adatoms. The second step is the two dimensional and three dimensional nucleation and cluster growth. The third step is the three dimensional crystal growth of bulk material.

The most important parameters determining the growth mechanism of electrodeposition is the atom-surface binding energy and the crystallographic misfit between the atom and bulk electrode. Three growth modes are introduced here: "Volmer-Weber" mode, "Frank-van der Merwe" mode and "Stranski-Krastanov" mode [85]. The analysis of deposition modes will be discussed in the experimental part.

The "Volmer-Weber" is the case where the binding energy between the atoms and the substrate (E_{A-B}) is lower than the binding energy between the atoms and substrate with the same material (E_{A-A}). The deposited atoms usually form 3D islands.

If E_{A-A} is greater than E_{A-B} and the misfit between the atoms and the bulk electrode is negligible, the "Frank-van der Merwe" mode occurs where the atoms are deposited layer by layer until the electrode is totally covered by the deposited atoms. If the crystallographic misfit is significant, the "Stranski-Krastanov" mode takes place. The atoms prefer to stay together, forming isolated islands on the electrode surface after a 2D layer is formed.

The growth mechanism is mainly determined by the surface structure itself. The texture and morphology of the metal deposits are strongly affected by the crystal properties of the depositing metal as well as by mass and electron transfer across the interface. The texture and morphology formation on the surface is very complex since different crystallographic orientations are involved. In addition, crystal defects, adsorbed molecules, oxide layers, etc., make this problem more complicated.

Using Faraday's law and Fick's equations, the depositing current in the early stage of electrodeposition is given by $i(t) = \alpha t^b$. The values of b are given in Table 2.1 [86, 87] for different nucleation and growth mechanisms. These b values will be used to determine the nucleation mechanism in the electrodeposition experiments performed in this work. Using this table, the resulting equations for instantaneous (Eq. 2.56) and progressive nucleation (Eq. 2.57)are:

$$(i^2/i_m^2) = 1.9524\{1 - exp[-1.2564(t/t_m)]\}^2(t/t_m)^{-1} \tag{2.56}$$

$$(i^2/i_m^2) = 1.2254\{1 - exp[-2.3367(t/t_m)^2]\}^2(t/t_m)^{-1} \tag{2.57}$$

Growth Mechanisms	Shape of Nuclei	Instantaneous nucleation	Progressive nucleation
Kinetically	Cylinder	b=1	b=2
	Hemisphere	b=2	b=3
Diffusion limited	Planar diffusion	b=1/2	b=3/2
	Spherical	b=1/2	b=3/2

Table 2.1.: Values of nucleation parameters for various nucleation mechanisms

3. Experimental Methods

To measure the charge transport properties of single molecule, nanoscale gaps are needed to contact the molecules individually. STM-based break junctions have been successfully employed to assemble molecular junctions and measure physical and chemical properties of single molecules by generating nanogaps between a tip and a substrate. However, since the molecules are usually self-assembled into a monolayer in the STM configuration, the interference from the signals of surrounding molecules to the measurement of the target single molecules cannot be easily excluded. Therefore, nanogaps formed by two nanoelectrodes with small radius of curvature are desirable to measure single molecules. In the following, we introduce the methods to fabricate nanogaps by lithography and the modification of the template nanogaps by electrochemical deposition and etching methods.

Firstly, the procedures of fabricating nanogaps by optical lithography and electron beam lithography are introduced. Then, the electrochemical modification method of the lithography defined nanogap electrodes is described. Secondly, the method of integrating electrochemical deposition and mechanical break junction setup is described. Finally, the protocols of assembling and measuring molecular junctions are presented.

3.1. Nanogap fabrication

Three methods of fabricating nanogaps on silicon chips were used in this work: optical lithography, e-beam lithography and electrochemical deposition/etching. Three types of insulating materials were applied: photoresists, electron beam resists and SiO_x/SiN_x. Two ways of connecting the chip to the external electrical circuits were employed: encapsulating the chips with carriers and directly touching the chips by tungsten needles in probe station.

3.1.1. Layout design

The masks were designed with AUTOCAD. Several notes need to be taken care of when designing patterns with AUTOCAD. Firstly, the native format of AUTOCAD is DWG file, while it needs to be exported to DXF files before sending to the electron beam writer.

Secondly, blocks are preferred when designing the complex patterns, since blocks produce less errors when converting the DXF files the machine file in the electron beam writer. Thirdly, the structures with similar sizes should be bundled into one layer.

Twenty nine pairs of facing electrodes were designed on a rectangular area of 11x11 mm and two additional electrodes are added as the test electrodes. Rectangle shape was exclusively used in the pattern design, with the down scaling of feature sizes below 50 nm. The layout includes the following layers:

- Markers and base line.
- Contact pads and conducting leads.
- Fine nanogap electrodes.
- Access window over contact pads and nanogaps.

3.1.2. Optical lithography

Optical lithography is widely used to fabricate patterns on the surface of silicon wafer [88]. The resolution of the optical lithography is in the order of micrometers and is not suitable to fabricate gaps in nanoscale. However, due to its fabrication efficiency and accessibility, the optical lithography is used to fabricate the structures in the micrometer range such as conducting leads, contact pads, access window, etc.

The substrates for optical lithography are silicon wafers and the wafers are insulated by a layer of SiO_x before use. Silicon oxides can be developed by wet oxidation method or dry oxidation method in an oxidation oven. Both methods have advantages and disadvantages. For dry oxidation, the surface of the oxidation layer is smoother than the wet oxidation, but the thickness of the oxidation layer by dry oxidation cannot exceed hundreds of nanometers. For wet oxidation, the surface is rough but the thickness can be up to 1 µm or more.

In photolithography, a mask with the required structures is placed on the substrate and the same pattern is transfered to the photo resist layers. This process is called pattern transformation. The photo mask is a key component in the photo lithography process. The mask is usually made of UV-transparent glass and a structured layer of chromium is deposited on the surface of the glass. The resolution of the structures on the masks is in the order of microns. The structures on the masks are fabricated by electron beam lithography. The fabrication process is illustrated in Fig. 3.1.

The photoresists are organic polymers prepared in organic solvents and can be spread over the wafer surface by spin coating. The wafer is fixed on a vacuum chuck and the photoresist solution is dropped on the surface of the wafer by a plastic pipette. When the wafer rotates at high speed (2000–6000 rpm), the polymer solution spreads all over the wafer

Figure 3.1.: Optical lithography process for a negative resist. (a) cleaning silicon wafer; (b) insulating silicon wafer by silicon oxides; (c) spin coating photoresist; (d) exposure by UV light; (e) post baking the wafer; (f) flood exposure; (g) development of the structures; (h) sputtering layers of metals; (i) lift-off process to get rid of the unnecessary structures.

surface, forming an even layer of photoresist solution. The volatile solution is evaporated and a layer of photoresist polymer is formed. The thickness of the photoresist layer is related to the properties of the polymers and the speed of the spin coating. The resists are divided into two categories: positive resists and negative resists. For positive resists, exposed area dissolve into the development solution. On the contrary, for the negative resists, those exposed resists stay but unexposed resists dissolve into the development solution. After the development, the wafer is baked on a hot plate to remove the access solvent and make the photoresist photosensitive.

The photoresists are only sensitive to a narrow range of wavelength, thus the output of the light source needs a filter before exposing the resists. The exposure doses also need to be tested to find an appropriate values for the resists. The accurate exposure doses are of vital importance to obtain best structural resolution.

After the exposure, a process called image reversal can be applied which converts the positive photoresists to negative photoresists. The reason for using the image reversal process is that the side wall created in this way is suitable to apply lift-off process. Compared to the normal lithography, a post-bake or reversal-bake is applied after the exposure. This process is aimed to assist the cross-linking of the photoresist at the exposed area. The post-bake temperature is a critical parameter of the image reversal process and it should fall within the range from 115 °C to 125 °C.

After the development, metalization procedures are applied. Materials can be sputtered on the surface of the wafer through the opening of the photoresist (plasma enhanced chem-

ical vapor deposition or simply hot sputtering). Layers of silicon oxides, silicon nitrides, and metals can be deposited by such methods. Metals are usually deposited for structuring the conducting leads and SiO_x/SiN_x are used as insulating layers.

After metalization, the wafers are immersed in the acetone and the portions that have photoresist layers are resolved, leaving the metal structures on the wafer surface. This step is referred to as "lift-off" process. Mega-sound can be used during the lift-off process to facilitate the peeling of the resist layers.

The procedures of optical lithography were as following:

- The wafers were firstly cleaned by piranha solution to remove organic contaminants. The wafers were immersed to the piranha solution for 10 minutes and rinsed by enough amount of water.
- The wafer was then cleaned by wafer cleaner and plasma treatment for 10 minutes at a power of 100 W in plasma oven. This step can remove particular matter as well as any traces of organic ionic and metallic impurities from the surface.
- A layer of SiO_x was generated by dry oxidation in an oxidation oven.
- The mask was cleaned in a mask cleaner before and after every use.
- Before applying photoresists on the surface of the wafer, the wafer was treated in an oxygen plasma oven (100 W, 10 minutes) to increase the adhesion between photoresist and the wafer.
- A layer of photoresist AZ-5214 was evenly spread on the wafer by a spin coater with the spin rate of 4000 rpm.
- Exposure to the photoresist was performed on the mask aligner. The light source with i-line (365 nm) was used. The power of the incident light was usually set to 245 w/cm^2 and the exposure time was varied according to the required exposure doses of the photoresist. Here, exposure time of 4.5 seconds was used. The "soft contact" mode was employed when fixing the wafer on the exposure chuck.
- Image reversal: the wafer was post baked at 115 °C for 5 minutes.
- Flood exposure: 10 seconds exposure on the whole wafer.
- The wafer was then immersed in the development solution for 1 minute.
- Titanium/gold layers with the thickness of 10/50 nm were sequentially deposited on the surface by sputtering.

- Lift off: the wafers were immersed in acetone until the photoresists and the metal layer on the resists were totally dissolved.
- The structures of the chip were examined by SEM.
- The profiles of the nanostructure were checked after development of the photoresist, after the metallization, or after the lift-off process by a profile checker.

3.1.3. Electron beam lithography

The principle of the electron beam lithography is similar as the optical lithography [89]. In optical lithography, the structures on the mask are directly transferred to the wafer in one shot, however, in electron beam lithography, the structures are directly written by moving the focused electron beams. The wavelength of the electrons can be adjusted by the accelerating voltages (1–100 kV) and very small wavelength down to pm range can be achieved. The electron beam can be focused by magnetic apertures to spots of several nanometers. Usually, a Gaussian beam system is used, where the electron beam is focused to circular shaped spot with Gaussian intensity distribution. By moving the electron beam in a controlled way, the electrons accumulate at the area, causing the change of chemical properties of the electron beam resists. In this way, the structures can be directly defined. The electron beam has a spot size of several nanometers; however, the electrons scatter at the surfaces between resists and the substrate, having the neighboring resists exposed. This phenomenon is known as proximity effect [90–92], which lowers the actual resolution of the electron beam lithography. As a result, the electron beam lithography has a resolution of 5–20 nm [93]. The disadvantage of the electron beam lithography is that it is very expensive device and is not accessible for many groups (Tab. 3.1). The electron beam lithography is very time consuming, so usually only a small amount of samples can be fabricated. In this work, nanogaps with the gap size of several nanometers are needed, which cannot be fabricated by normal optical lithography, therefore, electron beam lithography is used to fabricate the nanoscale gap structures.

	Resolution	Time consumed	Access to device	Reproducibility
Optical lithography	Micrometer	Short	Easy	Media
E-beam lithography	Nanometer	Long	Very difficult	High

Table 3.1.: Comparison between optical lithography and e-beam lithography

The process of electron beam lithography is demonstrated in Fig. 3.2. Electron beam resists like PMMA are first spin coated on the properly insulated wafers. Since the PMMA has much lower viscosity than the optical photoresist, thus very thin PMMA layer (about 200 nm) can be spread on the surface of wafer. The height of the PMMA layer also determines the resolution of the structures since high respect ratio structures cannot easily obtained.

The development process of the e-beam lithography is similar to that in the optical lithography. No image converting steps are needed in e-beam lithography. The following metalization and lift-off are similar as the optical lithography.

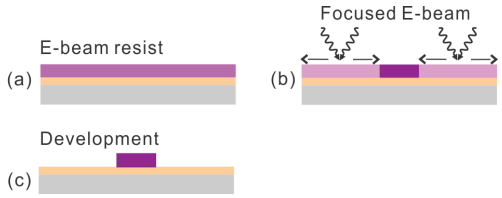

Figure 3.2.: Scheme of electron beam lithography. (a) Electron beam resists are spin coated on the wafer. (b), The resists are exposed directly by moving the electron beams. (c) The development of resists is similar as the steps in photolithography.

The general methods to fabricate nanogap electrodes by electron beam lithography were as following:

- Electron beam resist PMMA 600k was spin-coated on the silicon wafer at a speed of 6000 rpm.
- The wafer was then baked on hot plate at 180 °C for 2 minutes.
- The electrode array pattern was written by the electron beam writer. The voltage was 50 kV. The beam sizes and step sizes were chosen according to the designed pattern. For the nanogap electrodes, the main beam size is 2 nm and the step size is also 2 nm. The block size was 320 µm and the pattern size was 1.1 mm.
- Standard development procedures were applied for 1 minute.
- Ti/Au layers of 5/50 nm were sputtered on the wafer.
- Lift-off process was applied.

3.1.4. Insulation and connection of nanoelectrodes

Since the silicon chips are assumed to measure molecules in liquid environment, the electrodes on the surface of wafer needs to be insulated before use. Two types of dielectric

materials are commonly used: inorganic material like SiO_x/SiN_x or organic material like photoresist/electron beam resists.

Inorganic dielectric materials SiO_x/SiN_x can be applied on the surface of the wafer by chemical vapor deposition (CVD). The structuring of the SiO_x/SiN_x layer can be performed by reactive ion etching (RIE, see Fig. 3.3). In RIE, the wafer is placed in the chamber where the ions are produced. Different ions are selected according to the material, for instance, CF_4/O_2 ions can be used to etch into silicon oxides. The advantage of RIE is the uniform anisotropic etching which creates structures with little undercutting edges. This property is especially critical for high-fidelity pattern transfer.

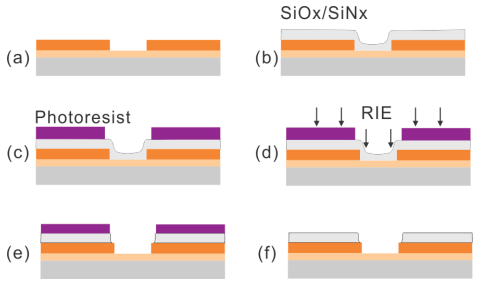

Figure 3.3.: RIE process: if inorganic materials are used to insulate the electrodes, firstly a layer of photoresist is deposited on the nanogap chip by spin coating. Then the access window can be opened by lithography and RIE.

For the inorganic material based insulation:

- SiO_x/SiN_x was deposited on the surface of the wafer by PECVD.
- The structuring of the SiO_x/SiN_x layer was performed by reactive ion etching, CF_4/O_2 ions were used to etch into silicon oxides.

For photoresist based insulation:

- The methods were same as optical lithography.

For electron beam resist based insulation:

- Three layers of electron resists (PMMA 600k/900k/600k) were covered on the nanogap chip by spin coating at 6000 rpm.
- The access windows were opened by e-beam lithography.

The nanostructures are supposed to be used in electronic applications, thus, the electrical characterization of the nanostructures including conductance, capacitance, and leakage

current is needed before further investigation. Then it is necessary to connect the nanogap structures to the external measuring circuits. Two routines are usually applied: one is to encapsulate the silicon chip into a chip carrier and to fit the chips into a chip socket which is connecting the external circuits (Fig. 3.4); In this method, the contact pads are opened on the insulating layer (either SiO_x/SiN_x or photoresist), then the chip are encapsulated into a chip carrier by a flip machine. The second method is to contact the nanostructures through the contact pad directly by tungsten needles in a probe station. These tungsten needles are connected to the external measuring circuits. In both cases, the whole setup is placed in a Faraday cage to insulate from electromagnetic waves.

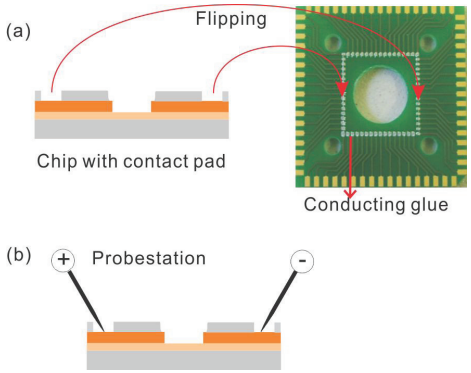

Figure 3.4.: A silicon chip connected to the external circuit either by encapsulating to a chip carrier (a) or by a pair of tungsten needles mounted in a probe station (b).

3.2. Electrochemical experiments

Electrochemical deposition is a flexible and effective method of structuring and modification of solid state surface. This is because that: 1, the electrochemical phase formation can be easily controlled by the electrochemical potential and current; 2, the electrochemical process is usually performed at room temperature, which is desirable since at high temperature different materials will diffuse and contaminations will occur; 3, different kinds of material such as metals, semiconductors and conducting polymers can be deposited with corresponding solution. Due to the above mentioned reasons, nanofabrication by electrochemical deposition and etching become of increasing interests for both academic research and industry application [94–97].

The electrochemical deposition and etching is suitable to fabricate nanostructures since the process is reversible and can be performed until the desirable structures are made. The reduction reaction can occur spontaneously when certain reduction reactants are presents, and this process is refereed to “electroless deposition” [98, 99]. However, the deposition

process take place under open circuits in the electroless deposition, thus, measuring the electrochemical current and controlling the morphology of the deposited materials are difficult. The other situation is that the reduction process occurs under the external potential control. In this case, the controlling and measuring the potential become feasible and detailed study of deposition process can be performed.

With the gold atoms depositing on the nanogap electrodes, the electrodes approach to each other, and the distance between the electrodes is decreased [20]. On the other side, with the gold atoms on the electrode dissolving into the solution, the electrodes recede and the distance between the electrodes becomes larger. Therefore, by switching the potential between the deposition range and the etching range, the gap size of the predefined nanogaps on silicon chip can be adjusted reversely.

The deposition rate and the morphology of deposited material can be also controlled by the potential and current. In the nanogap fabrication, the gap size can be monitored by the feed back signals such as tunneling current, impedance or the potential drop at the electrochemical double layer. Various metals can be employed to deposit to a predefined gap template, creating nanoscale gap from 1 nm to 100 nm. Atomic point contacts can be also created if enough atoms are deposited, closing the nanoscale gap and forming a connection in the atomic scale. This atomic scale connections show discrete conductance and have potential application in single atom transistor and sensors.

Individually addressed nanogaps can be bridged by carbon nanotubes, conducting polymers and even single molecules, forming nano-junction structures. By applying a bias to the nano-junctions, the charge transport properties can be investigated. Provided with appropriate conditions, such as vacuum chamber and cryostat, charge transport at low temperature and high vacuum conditions can be studied. Even the optical properties of the nanoscale object can be probed by adding a spectroscopic instrument.

3.2.1. Electrochemical investigation of macroelectrodes

- Before experiments, the electrochemical cell, all the glass and Teflon attachment were cleaned by boiling in nitride acid and thoroughly rinsing with Milli-Q water.
- The gold electrodes were flame annealed before use and rinsed by Milli-Q water.
- The General Purpose Electrochemical System (GPES) (Eco Chemie B.V. Utrecht, Netherlands) was used to control the potentiostat.
- For cyclic voltammetry, “cyclic voltammetry method (staircase)” was used. The first conditioning potential was chosen to be the starting potential for 1 second. The number of scans was set from 3 to 10 depending to the stability of the curves. The option

of "cell off" after measurement was chosen. The start potential and end potential were chosen as required. The principle was that the potential ranges should be large enough to cover the redox potentials but not too large to induce electrolysis of water. The scan rate was set to 100 mV/s.

- For deposition/etching experiments, the "chrono methods" (interval time > 0.1 s) were used. The potential and duration time was set as required. The potential of the second working electrode was also set. A cut-off value of current was set to 1 µA, and when the recorded current reaches the cut off value, the operation would be stopped.

3.2.2. Electrochemical investigation of nanoelectrodes

- The operations of potentiostat and the GPES software were similar as the investigation of macroelectrodes.
- The chips were mounted on probe station which connected the nanoelectrodes to the Autolab potentiostat by coaxial cables.
- After the nanogap chip was fabricated, a glass O ring was glued on the surface of the chip by PDMS and a micro electrochemical cell was formed.
- The chip was placed on the holding stage in the Faraday cage by a vacuum chamber and illuminated by optic fiber illuminator with a maximal intensity of 70,000 lx.

3.2.3. Electrochemical break junction setup

Adjusting the gap size by electrochemical deposition and etching requires a deposition solution. However, most of measurements of molecules are performed in air, vacuum, or a moderate liquid like phosphate buffer. To overcome this limitation, mechanical break junction mechanism is combined with the electrochemical deposition/etching techniques to generate adjustable nanogaps in liquid.

- A nanogap electrode chip was fabricated.
- The size of the nanogap was adjusted to the desired value or to atomic scale junctions by the electrodeposition/etching.
- The chip was mounted on a mechanical controlled break junction setup and the depositing solution was removed. Then the gapsize of the nanogap was adjusted by mechanically bending the substrate in air or in moderate solutions.

3.3. Molecular junction assembly and measuring

The metal/molecules/metal junctions can be divided into two types according to the number of molecules between the metal electrodes: single molecule junction and ensemble molecule junction. Each type of molecular junction can be implemented in several forms [100].

The single molecular junction is mainly realized by scanning tunneling microscopy (STM), conducting probe atomic force microscopy (cpAFM) and mechanical controlled break junctions. One of the earliest works on STM related techniques appeared in 1996 [74], in which isolated phenylethynyl thiolate molecules diluted in a less conducting dodecanethiolate monolayer was investigated. Then many STM-based break junction experiments have been reported to observe transport behavior through single molecules by incorporating single molecules between two nanoscale contacts [101, 102]. The molecular junctions are formed when a molecule in solution bridges a newly formed gap between the conducting tip and the metal surface. The imaging ability of the STM provides the atomic scale information of the chemical bonding and the conformation of the molecular junctions.

One example of ensemble molecular junctions is the liquid-metal junction formed by suspending an Hg drop over a metal surface (Ag for instance) in a solution of thiol molecules [103]. Another example is crossbar junctions made by evaporating or imprinting a top electrode onto a molecular layer covalently bonded to a bottom electrode [104].

It is a critical step to bond molecules to conducting substrates used in both single-molecule and ensemble junctions. The type of the molecule/metal bond determines the degree of electronic coupling between the molecule and conductor and thus has a great influence to the transport properties since the bonds determine the potential barriers in the overall electronic properties of the device. The molecular orbitals are often broadened due to the orbital mixing with metallic orbitals in the contact. If the coupling between the molecules and the electrode is very strong, the electronic behavior of the molecular junctions may be interface-dominated, and then the molecular structure has little influence on the properties of the junctions. The common routines of bonding molecules to metal surface include metal-sulfur [105, 106], Langmuir-Blodgett [107, 108], and covalent silicon-carbon bonds [109, 110]. The coupling strength of these bonding is different and listed in the Table. 3.2.

Bond type	Langmuir-Blodgett	Si-C and Si-O	C-C
Bond	0.5 eV	3.5-4 eV	3.5-4 eV

Table 3.2.: The bond type and the corresponding surface energy.

The gold-thiolate bonds have been one of the most widely used approaches for making single molecular junctions largely because they have stable coupling between the molecules and the metal electrode, and Au-S bonds have been thoroughly characterized with spectroscopy, SPM, etc. The electrostatic bonds also find wide application in self-assembled monolayers since the relatively weak bond energy allows the diffusion of molecules to an ordered monolayer form. The Si-C and C-C bonds have much higher energy and are less commonly used since they are generally less ordered. The covalent bonds can produce strong electronic coupling between the metal electrode and molecules, which makes them more advantageous for useful devices. However, in some fields like designing sensors, the strong covalent bonds are not always appropriate. For example, if graphene is used as the sensing material, the strong C-C bond would damage the structure of graphene and the device will lose the functions.

Most of the molecular junctions involve only one type of bond (Au-S, for instance), a few molecular junctions include more than one type of bond. For example, in the work of Wu et al., molecules with thiol group at one end and aromatic groups at the other end were used. Two such molecules were involved in the molecular junctions: the molecules were bond to the gold electrode by the Au-S bond and molecule-molecule coupling was achieved by the aromatic coupling [41]. The unique advantage of the heterogeneous molecular junctions is that the charge transport properties through intermolecular coupling can be investigated. The intermolecular charge transport mechanism is of fundamental importance for designing sensors or understanding the electron pathway in the biological system.

3.3.1. Au/Benzenedithiol/Au junctions

- After the electrodeposited nanogaps are fabricated, the depositing electrolyte was removed, and rinsed several times with Milli-Q water.
- Subsequently, the chip was immersed into the ethanol solution containing 1 mM benzenedithil (BDT) for 10 minutes.
- The chip was rinsed by pure ethanol and blown dry with Argon gas.
- The chip was connected to the measuring instrument by tungsten needles and the setup was placed in a Faraday cage to decrease the interference from the environmental electromagnetic waves.

3.3.2. Au/cysteamine/ferrocene/cysteamine/Au junctions

After thorough testing of electrodeposited nanogaps by the model molecule benzenedithiol, the mechanical break junction mechanism was introduced and an electrochemical break

junction setup was established. This setup was used to investigate the intermolecular charge transport through electrostatic interface by assembling molecular junctions based on intermolecular electrostatic interactions. The assembly and characterization of electrostatic molecular junction were performed in aqueous solution. The establishment of an electrochemical break junction experiment was a key to this study since electron transport across electrostatically linked molecules can be only studied in solvents and not obtainable under cryogenic and/or vacuum conditions.

To evaluate the appropriate pH range, cyclic voltammetry of cysteamine modified gold electrodes with/without electrostatically adsorbed 1,1-ferrocene dicarboxylic acid (FDA) molecules was examined at different pHs. The procedures were as below:

- Gold electrodes defined on a chip with exposed area of $0.02\,\mathrm{mm}^2$ were used as working electrodes (see Fig. 3.5).
- A gold wire with a diameter of 0.5 mm and an Ag/AgCl electrode (WPI inc., Germany) were employed as counter electrode and reference electrode, respectively.
- The working electrode was firstly incubated in 0.1 mM cysteamine aqueous solution for 10 minutes to form a cysteamine monolayer.
- The electrodes were subsequently rinsed with Milli-Q water (Millipore Co., 18.2 MΩ) to remove the excess cysteamine molecules.
- The cysteamine modified electrode was incubated in 40 mM Britton-Robinson buffer containing 0.1 mM 1,1-ferrocene dicarboxylic acid molecules for 10 minutes
- The modified electrode was then rinsed with bare buffer to dissolve excess 1,1-ferrocene dicarboxylic acid molecules. Note that this step can be omitted to perform cyclic voltammetry with the presence of 1,1-ferrocene dicarboxylic acid molecules.
- The cyclic voltammograms (CVs) were recorded by means of an Autolab potentiostat (Metrohm B.V., Netherland) at different pHs
- The potential ranges of the cyclic voltammograms were set according to the applied pH to avoid the interfering of gold oxidation at anodic potentials.

To reveal the charge transport process on single molecule level, measurements were performed on a home-made electrochemical break junction setup, which was tailored for measuring molecules in aqueous solution.

- Briefly, pairs of facing nanoelectrodes were fabricated on silicon chip and encapsulated by PMMA layer

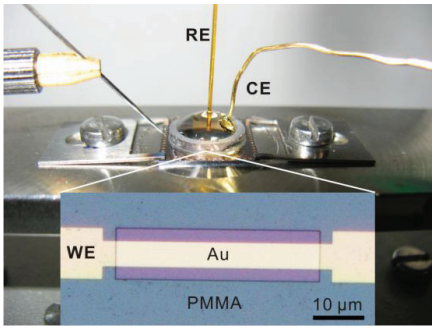

Figure 3.5.: Performing cyclic voltammetry on chip. Working electrode (WE): gold electrode defined on silicon chip encapsulated by PMMA with exposed area of $0.02\,\mathrm{mm}^2$. Counter electrode (CE): gold wire with melting tip. Reference electrode (RE): Ag/AgCl microelectrode. The leads are used to provide electrical connections to the working electrode.

- The two electrodes were initially separated by a 150 nm gap and subsequently narrowed by electrochemical deposition until a gold junction was formed.
- The electrode surface morphology was tuned by the deposition potential to generate a dendritic surface, which results in smaller contact area between the electrodes and better stability.
- The nanoelectrodes were incubated in 0.1 mM aqueous cysteamine solution for 10 minutes and then rinsed with Milli-Q water.
- Afterwards, it was immersed in 40 mM Britton-Robinson buffer containing 0.1 mM 1,1-ferrocene dicarboxylic acid molecules and subsequently broken/closed by moving the piezo.
- For the electrical characterization of the junction, a bias was applied by setting one electrode at 0 V and the other at 0.13 V with respect to Ag/AgCl electrode.

4. Results and Discussions

The first part of the results describes the fabrication of nanogap electrodes with fixed nanogap size on silicon chips. Firstly, arrays of facing micro-scale electrodes with initial separation of 10 µm were fabricated by optical lithography, which were used as conducting leads and contact pads. Secondly, nanoscale electrodes with separation varying from 2 nm to 100 nm were fabricated by electron beam lithography on the bases of the micro-scale electrodes, which can be used as template electrodes for later electrochemical modification. Finally, the surface morphology of the nanogap electrodes was modified and the size of the nanogap was fine tuned by electrochemical methods. Needle-like nanogap electrodes were obtained by electrodeposition at low overpotentials and the size of the nanogap was tuned down to sub nanometer. The needle-like electrodes are more suitable to contact and measure charge transport properties through molecules at single molecule level.

In the second part, simple molecular junctions Au/benzenedithiol/Au were assembled on the electrodeposited needle-like nanogaps. The I-V curves of the Au/benzenedithiol/Au were obtained but no definite conclusions were drawn from the I-V curves due to the limitations of the fixed nanogap when measuring charge transport properties through molecules. Theses limitations made it necessary to fabricate adjustable nanogaps that can be used in solutions.

The third part illustrates the fabrication and characterization of an in-situ electrochemical break junction setup, which can generate nanoscale gaps up to 4 nm in aqueous solution with low electrochemical leakage current.

The last part includes assembling and characterization molecular junctions based on intermolecular electrostatic coupling. Junctions Au/cysteamine/ferrocene/cysteamine/Au were dynamically formed and the conductance through the molecular junctions was measured on the electrochemical break junction setup. Since the ferrocene junctions were repeatedly formed and broken, statistical analysis could be employed, which made the results robust and convincing. The formation of the ferrocene junctions was based on intermolecular coupling, in this way, the intermolecular charge transport across the electrostatic interfaces was investigated on this well designed ferrocene junctions.

4.1. Nanogap chip fabrication

This section starts with the pattern design of the nanoelectrodes. Rectangle-shaped nanoelectrodes or triangle-shaped nanoelectrodes were employed in the electron beam lithography. The fabrication results showed that the triangle-shaped nanoelectrodes had better stability and were more suitable for the following fabrication processes. The impact of the exposure dose on the gap size is discussed and the relationship between the exposure dose and gap size is employed to fabricate nanogaps with various gap sizes. The radius of curvature of the nanoelectrodes fabricated by electron beam lithography was measured as 50 nm, which would be a disadvantage when measuring single molecules with this electron beam lithography fabricated nanogaps. Focused ion beam etching was also tested to create nanogaps by directly etching through a nanowire; however, the nearly parallel geometry of the electrode tip would not be appropriate for measuring single molecules, since large number of molecules would be incorporated between the nearly parallel nanogap electrodes. The nanogaps are supposed to be used in aqueous solution, the insulation of the electrodes is of vital importance. Due to the resolution of the optical lithography, misalignments were found between the nanogap electrodes and the access windows structured on the insulating layer that should be right on top of the center of nanogaps. This misalignment caused asymmetrical electrochemical responses. Electron beam lithography has high accuracy and can create access window over nanogap electrode with fine alignment. So, electron beam lithography was used for structuring the insulating layer covered on top of the nanogap electrodes. Besides the organic insulating material, inorganic material SiN_x was also tested. SiN_x demonstrated better insulating properties than organic materials; however, several technical problems were found which hinder its applications in this work.

4.1.1. Micro-scale structures fabricated by optical lithography

Pattern design of micro-scale structures

The layout of conducting leads and contact pads was designed by AUTOCAD(Sec. 3.1.1). Twenty nine pairs of facing electrodes with electrode width of 10 µm and interval distance of 100 µm between the neighboring electrodes were designed on a 11 x 11 mm silicon chip as in Fig. 4.1. Most groups placed one or two pairs of electrodes in their chip design because of the easy of use [14, 111–113]. In our work, the design of multiple electrodes arrays allowed continuous experiments without stopping to replace the chip after the measurement of one pair of electrodes. Using multiple pairs of electrodes also allows parallel fabrication of nanogap electrodes as illustrated in the work of Johnston et al. [114] and Zhang et al. [115], where large numbers of nanogaps were fabricated in a single process by using a feedback

controlled electromigration. Square contact pads of 400 x 400 µm were placed on the edge of the chip (Fig. 4.1, right inset). Through these contact pads, connection between the nanogap electrode and external circuits can be established by tungsten needles mounted in probe station or chip carrier encapsulation. Test electrodes were provided for testing the chip after fabrication. Conducting leads with a width of 10 µm were evenly distributed and the distance between the facing electrodes was set to be 10 µm (Fig. 4.1, left inset). Two markers were designed for aligning the following lithography. The first marker was a cross used in the alignment of optical lithography and the second marker was a series of squares of 20 x 20 µm arranged in "L" shape, which was mainly used for the alignment in electron beam lithography.

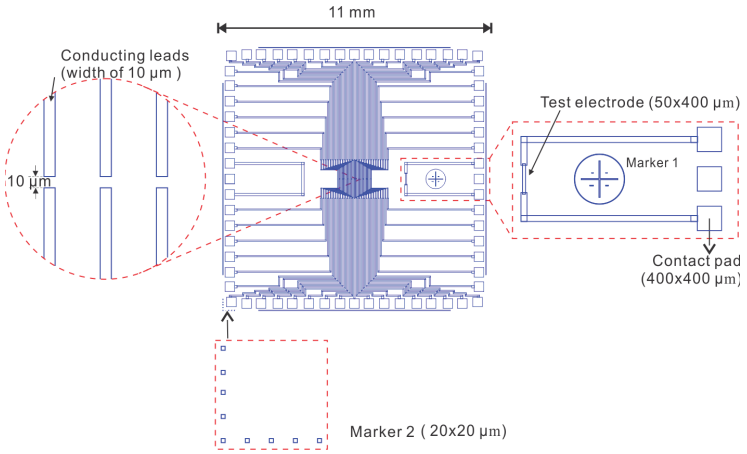

Figure 4.1.: Layouts of contact pads, conducting leads, and markers on a silicon chip.

Micro-scale structures

The detailed fabrication process by optical lithography is described in the experimental section (Sec. 3.1.2). The micro-scale structures including contact pads, conducting leads are presented in Fig. 4.2.

The micro-scale structures of electrodes were successfully fabricated and no obvious structural defects on the electrodes were observed. The surface was clean and no visible contaminations were found. The sizes of contact pad (400 x 400 µm) and test electrodes (50 x 400 µm) were as designed. Note that the contact pads were already insulated and an access window was opened right on top of the contact pads. The markers for both optical lithography and electron beam lithography were also fabricated with fidelity. The results indicated that the optical fabrication process was success and parameters used for optical lithography were well optimized.

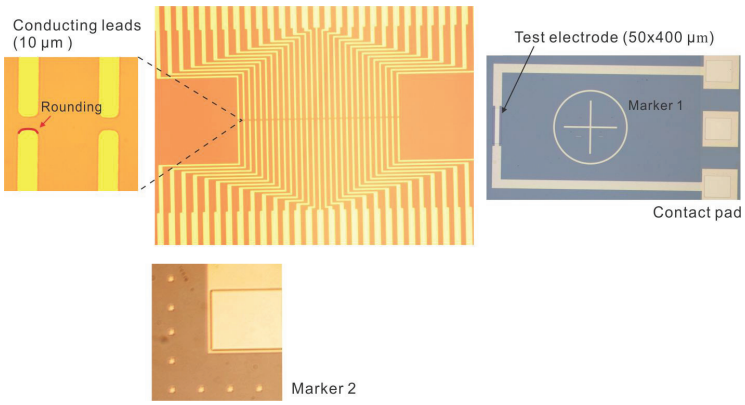

Figure 4.2.: Micro-scale structure (contact pads, leads, markers) fabricated by optical lithography

One problem of the structures fabricated by optical lithography was that the edge of the electrodes was rounded (Fig. 4.2, left inset). The rounding effect at corners is a common problem for photolithography [116]. In the exposure process, the UV light scatters at the interface between the resist and the mask, and exposes the resist in proximity. The wafers are placed on a vacuum chuck and contact with the mask by a pressure. The contact modes can be chosen as soft contact mode or hard contact mode. In the "soft contact" mode some space is left between the wafer and the mask, but in the hard contact mode the wafer and mask is tightly pressed together. In this work, soft contact mode was used since the structures on the surface of mask would damage the surface smoothness of the resist in the hard contact mode. The space between the wafer and mask in soft contact mode also enlarges the scattering effect of UV light. The lift-off process also contributes to the rounding effect. Resist residues often accumulate at the corners, especially at acute angles and right angles, which causes insufficient deposition of metal atoms when sputtering and results in rounded corners. Several structure transfer steps were involved during the lithography and each step introduced a deviation of structures from the last pattern. The deviation accumulated and finally the rounded corners were observed. The exposure time of 4.5 s was not the reason of the rounding corner, since if the exposure time was increased; the rounding effect was not be removed. Although the rounded corner were observed, the pattern fidelity of the structures was sufficient to use the micro-scale structures as conducting leads and contact pads.

4.1.2. Nanogap fabricated by electron beam lithography

Nanoelectrode design

The fine structures like pairs of facing nanoelectrodes were fabricated by electron beam lithography. Rectangular electrodes were firstly designed and tested since the rectangle shapes can be easily handled in the electron beam writing system (Sec. 3.1.1). The pattern of rectangular electrode arrays was designed as a series of rectangles with decreasing electrode width from 5 µm to 50 nm (Fig. 4.3). The rectangle shape was exclusively used in the e-beam lithography design since the rectangle shape has the best structural resolution and fidelity [117]. An overlay area between the nanoelectrodes and the conducting leads was set to ensure proper electric connection. In each pair of electrodes, two rectangular electrodes were arranged face to face, forming a nanoscale gap of 150 nm (Fig. 4.3, right). A nanowire pattern was also designed (Fig. 4.3b) in order to create nanogaps by electrochemical etching or ionic beam etching. Creating nanogaps was reported by Shi et al. [118] and Blom et al. [119].

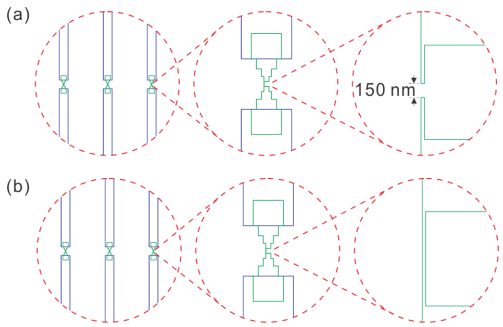

Figure 4.3.: (a) Arrays of facing nanoelectrodes with a 150 nm nanogap between the electrodes. (b) Arrays of facing nanoelectrodes with a nanowire between them.

We found that one of the factors affecting the fidelity of the fabricated structures is the acute or sharp corners in the nanostructures. As discussed in Sec. 4.1.1, the resist residues accumulate at the corners and result in rounded corners during the lift-off process. Therefore, in the structural pattern design, the number of corners of acute/right angles should be reduced to a minimum to obtain high fidelity structures.

For example, the tip of the rectangular electrodes in Fig. 4.3 was placed at the edge of the electrode instead of in the middle of the electrode. This design can reduce the number of right corners from 4 to 3 (Fig. 4.4a). The number of the corners was further reduced to 1 in a triangular electrode design (Fig. 4.4b). The tip angle was set to 42° and a 0.1 µm overlap lead was designed to obtain electric connection between the tip electrode and the conducting leads.

In the following, the fabricated nanogap electrode is presented and the effect of corners on the nanoelectrodes structures is discussed.

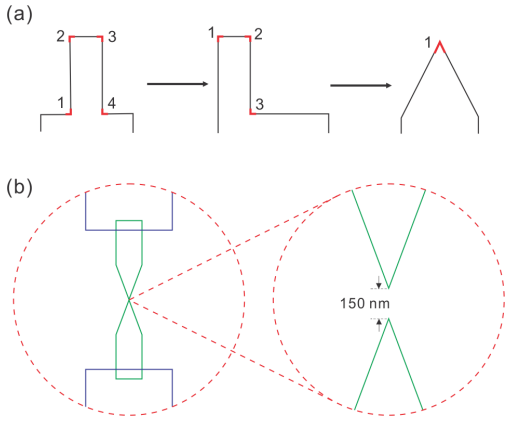

Figure 4.4.: (a) Reducing the number of right corners by placing the rectangular tip electrode at the edge instead of in the middle or by using triangular nanoelectrodes. (b) a nanogap design formed by a pair of facing triangular nanoelectrodes.

Fabrication of nanogap electrodes

The experimental details of fabricating nanogap electrodes are described in Sec. 3.1.3.

Arrays of facing rectangular nanoelectrodes were successfully fabricated on chip. The overall structure were examined by SEM and shown in Fig. 4.5. From the image, it can be seen that clean nanoelectrodes were obtained and a nanoscale gap of 150 nm between the facing nanoelectrodes was formed. The width of the tip electrode was estimated to be 50–60 nm. This values are similar as those in the work of Li et al., in which a pair of rectangle-shaped electrodes with width of 60 nm and a gap of 60 nm were fabricated [113]. The initial gap of 150 nm is much narrower than the initial gap size (5 µm) in the work of Chen et al. [120]. The height of the side wall, which represented the thickness of the gold layer, was estimated to be 60 nm. This value was consistent to metal sputtering parameters (Sec. 3.1.3), which was 10 nm titanium and 50 nm of gold. The surface of the electrode was not smooth and grainy particles of 10 nm were observed, which can be explained by the cluster effect in the metal sputtering process. The surface roughness was measured to be 4 nm by conductive AFM measurement [121]. This value was relative large compared to the size of the nanogap (150 nm), which made it necessary to perform further treatment like electrochemical surface modification. The rounding corners effect was also observed but it was difficult to quantify the effect due to the resolution of the SEM images.

A major problem was found in the fabrication of rectangular nanoelectrodes, that the tips of the rectangular nanoelectrodes were rather fragile and did not withstand further

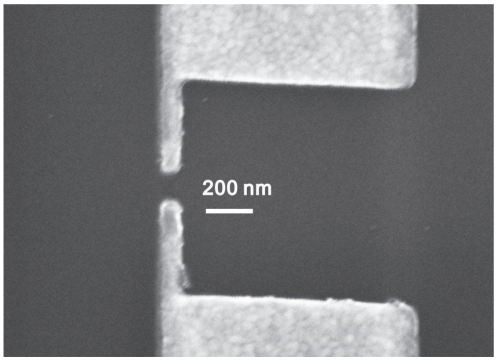

Figure 4.5.: SEM image of the rectangular nanogap electrodes fabricated by electron beam lithography.

treatment like lift-off process. About half of the twenty nine pairs of electrodes were damaged after the lift-off process and the entire tips were lost (Fig. 4.6).

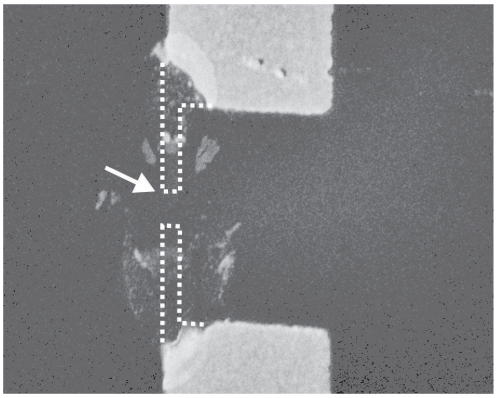

Figure 4.6.: The tips of the nanoscale electrodes were damaged after lift-off process.

The damage of the electrode tips can be explained by the side wall effect in the electron beam lithography. When using electron resist like PMMA, the boundary between the exposed area and unexposed area is not vertical, but tilts with an estimated angle of 70° against the substrate (Fig. 4.7). When sputtering metals, the atoms fill in the exposed area, forming nanowires with wedge-shaped cross-section. Thus, the actual width at the bottom of the nanowire is less than the width at the top of the nanowire, resulting in a very weak adhesion between the nanowires and the substrate. In addition, there are three right corners in the design of rectangular electrodes and the resists accumulate easily at these corners, which would in turn enhance the side wall effect, resulting in the weakest points at the corners. It can be seen that the tip electrodes always break at the corner sites (Fig. 4.6). This side-wall effect can be kept minimum by using two layers of resists with

different solubility in developer. This method was used in the work of Zotti et al. [122] and Kang et al. [28]. However, we did not continue to test two layer resist system.

Another consideration about the rectangular electrodes is the Joule heating produced when a bias is applied between the electrodes. Since the width of the nanowire is around 50 nm and the width is smaller at the corners due to the side wall effect, the local heating at the corners may have caused the structure fragile during the measurements. A example of the structural failure was illustrated in the work of Hadeed et al. [123]. The electro-migration study of gold nanowire has revealed that the electromigration is thermally assisted [124]. The electromigration and thermal runaway of the nanowire occur if the cross section area of the junction is very small. It was also reported that at temperature over 100 °C, the gold electrode will self break [125]. Due to these reasons, triangle-shaped nanoelectrodes were used in the electromigration experiments [126, 127], and feedback circuits were integrated into the electromigration processes to lower the bias when the cross section areas of the junctions decreases. To prevent the thermal runaway, structures with small cross section area should be avoided. In the electron transport study, bias potential as high as 1 V is usually used to obtain the *I*-*V* curves through molecules. To avoid the thermal runaway at the acute corners, the rectangular nanoelectrode were not used furthermore in this work.

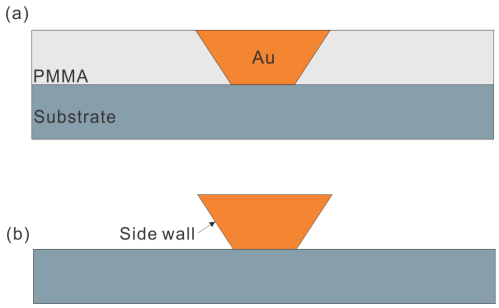

Figure 4.7.: Side wall effect during electron beam lithography, which caused a wedge-shaped cross-section of the electrodes.

Considering the problems of using rectangular nanoelectrodes, the electrode geometry was redesigned and triangular electrodes were tested as shown in Fig. 4.8. The experimental procedures were the same as the fabrication of the rectangular electrodes except the pattern design was different.

The triangular nanoelectrodes demonstrated better mechanical stability than the rectangular nanoelectrodes and nearly no tip electrodes were damaged during the lift-off process. The reason was that the number of acute/right corners was reduced to 1 (see nanoelectrode design) and no weak points were left in the whole structures. In addition, the width of the

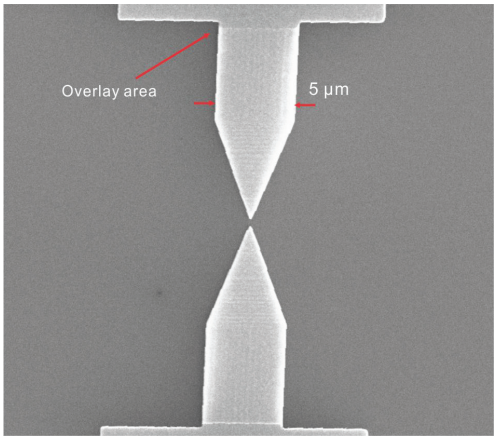

Figure 4.8.: A pair of facing triangular nanoelectrodes fabricated by electron beam lithography.

nanoelectrodes (5 µm, as indicated in Fig. 4.8) was designed much larger than the rectangular nanoelectrodes (50 nm) so that the side wall effect did not weaken the adhesion between the nanoelectrodes and the substrate. A similar triangle-shaped nanogap electrodes ready for electrochemical modification was obtained by Qing et al. [128] and Strachan et al. [129].

We have discussed in the previous part that small radius curvature is desirable when using nanogap electrodes to contact molecules. Using triangular nanoelectrodes, radius of curvature of the tip of the electrode were measured at 20 nm (Fig. 4.8). The tip angle was set to 42° and further minimizing the tip angle would possibly decrease the radius of curvature but it would be difficult to remain the mechanical stability of the nanoelectrodes. The thickness of the PMMA resist also determined the structure resolution. In this work, the thickness of PMMA is around 200 nm, and it is very difficult to achieve radius of curvature smaller than 5 nm. In the following, electrochemical methods were employed to obtain tip electrode with tip angle smaller than 42° and radius of curvature smaller than 5 nm (Sec. 4.2).

From the SEM image, a line of high intensity was observed at the bottom of the nanoelectrode, which was the overlay area between the tip electrode and the conducting leads. The overlay area was designed to ensure the electric connection between the tip and the leads (see nanoelectrode design), however, the thickness at the overlay area (120 nm) is twice higher than the thickness at other area (60 nm).

Tune the gap size by exposure doses

Due to the scattering of the electrons at the resist/substrate interface and the internal scattering within the resist, proximity effect always exists in the electron beam lithography.

An illustration of the scattering of incident electron beam at the interfaces of PMMA/SiO_2, SiO_2/Si was given in the work of Fischbein et al. [130]. If higher exposure doses are applied, the proximity effect becomes more prominent and the actual exposed area would be much larger than the designed pattern, resulting in over exposed structures. On the contrary, if low exposure doses are used, under exposure structures would be created. Therefore, appropriated exposure doses are required to generate structures with high fidelity. However, in this work, we utilized this property to fine tune the separation distance between the facing nanoelectrodes. The following part describes the relationship between the exposure doses and the gap sizes.

Firstly, the exposure doses were tested over a relatively large rang from 180 µC to 360 µC with a dose increase of 20 µC. The gap size between the two facing electrodes was observed to vary from 50 nm to total connection (Fig. 4.9), reflecting the impact of the exposure doses to the nanostructures. Only three images were presented (180 µC, 200 µC, and 220 µC), since from 220 µC, all the nanogap electrodes were connected. With exposure dose of 180 µC, the gap size was equal to the designed 50 nm (Fig. 4.9a). With increased dose, each electrode became larger and then the gap size was decreased to 25 nm. If higher dose (200 µC) was used, the nanogap came into total connection (Fig. 4.9c). The edge of the nanoelectrodes was not straight and some residues of gold were observed, which was caused in the lift-off process. The variations of gap size against the exposure doses indicated that the exposure doses can be utilized to fine tune the gap sizes.

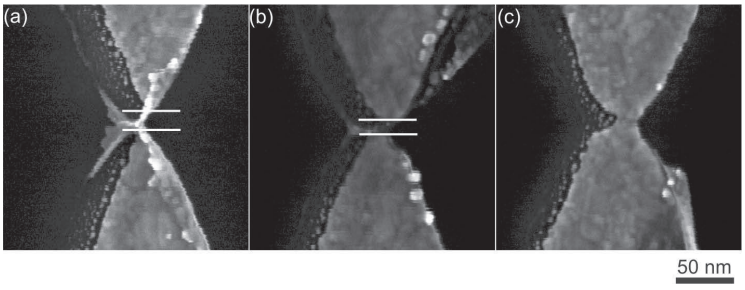

Figure 4.9.: A pair of facing nanoelectrodes fabricated by electron beam lithography under the dose of 180 µC (a), 200 µC (b), and 220 µC (c), forming open nanogap (a), (b), or a total connection (c).

Secondly, the exposure doses were tested within a narrow ranges from 170 µC to 205 µC with an increase step of 5 µC. The SEM images of first six doses (170 µC to 195 µC) were shown in Fig. 4.10, which demonstrated the nanogap sizes varying from 20 nm to total connection. For the 200 µC and 205 µC, the nanoelectrodes were totally connected as for the 195 µC. A nanogap of 2 nm was obtained when the dose was set to 190 µC. The relationship between doses and nanogap sizes was listed in the table below the images.

From the table, it was estimated that every dose increase of 5 µC could induce a decrease of nanogap size of 3–5 nm. Therefore, tuning the nanogap sizes by the exposure doses was achieved. This method of tuning nanogap size by exposure doses has not been reported before.

However, it was difficult to predict the sizes of the nanogap by the exposure doses, since the electron beam writing system was not exactly same for each writing batch due to the slight change of writing conditions, such as the drift of the electron beam, local heating effect caused by the electrons, or electron resists properties. Although the writing conditions remained same in the same batch of writing, variation from batch to batch was observed. For example, at 180 µC, the nanogap size of 50 nm was generated in the wide range exposure dose test (Fig. 4.9), but only 10 nm was observed in the narrow exposure dose test (Fig. 4.10). This variation from batch to batch made it difficult to fabricate nanogaps with faithful sizes, since it would be necessary to do dose series test all the time, which means that the majority of the chips cannot be used.

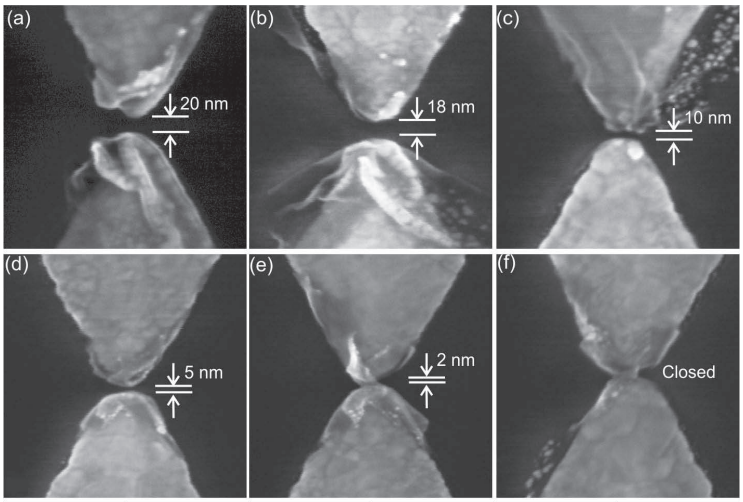

a	b	c	d	e	f
170 µC	175 µC	180 µC	185 µC	190 µC	195 µC
20 nm	18 nm	10 nm	5 nm	2 nm	Closed

Figure 4.10.: Fine tuning nanogap size by the exposure doses in electron beam lithography.

Radius of curvature of the electrode tip

Another problem which limits the use of nanogaps directly fabricated by the electron beam lithography is the radius of curvature of the electrode tip.

Although 2 nm nanogaps can be fabricated, which in principle can be directly used for measuring molecules with similar size, the radius of the curvature of the electrode tip was measured at 50 nm (Fig. 4.11a), which was one order larger than the gap size.

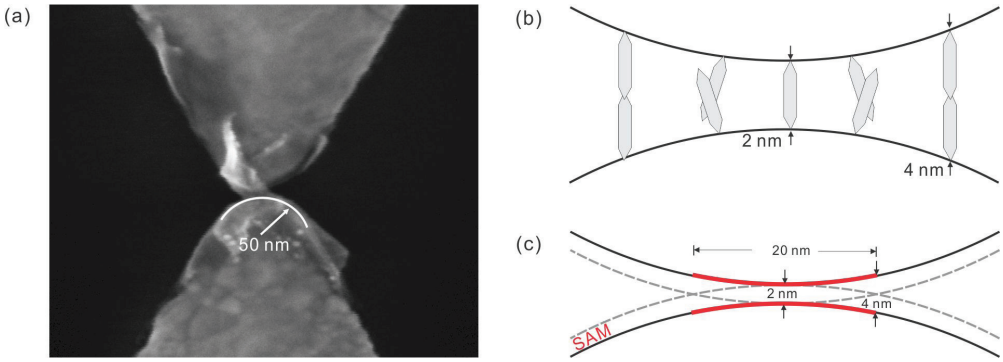

Figure 4.11.: (a) The radius of curvature of the nanogap electrode fabricated by electron beam lithography. (b) Multiple molecules would be involved in the charge transport process. (c) Estimation of the number of involved molecules by a simple model.

Supposing the target molecules have a length of 2 nm and a layer of self-assembled monolayer is formed on the electrode surface (Fig. 4.11b), the molecules are assembled into molecular junctions at the narrowest part of the nanogap. To fit the size of the 2 nm long molecules, two nanoelectrodes with separation of 2 nm at the narrowest part are required. Since molecules are adsorbed to the electrode surface, it is inevitable that the molecules will get touch into each other at other part of the nanogap beside the narrowest portion. It is possible that two molecules are aligned in a chain and form molecular junction with a 4 nm gap (indicated in the Fig. 4.11b). Thus, the measured currents through the junctions in this configuration actually are composed of currents through many molecules.

The number of the involved molecules in the molecular junctions can be estimated by a simple model (Fig. 4.11c). Considering the configuration where rod-like molecules are incorporated between a pair of facing nanoelectrodes and supposing the molecules are 2 nm long, the narrowest part of the nanogaps should be as the same size as the molecule (Fig. 4.11b). At the area where the gap distance varies from 2 nm to 4 nm, one single molecule dose not exactly fit into the gap, thus, electron transport pathway can not be established across single molecule. However, electron transport pathway can be possibly formed between the neighboring molecules. At the area where gap distance is larger than 4 nm, the molecules will absorb on either side of the electrodes and will not influence each other. The area where molecules influence each other (the red area in Fig. 4.11c) can be estimated as 314 nm^2. If the molecules are rod like with a diameter of 5 Å, then the surface of the cross section of the molecules is 0.2 nm^2. Therefore, over 1000 molecules can be ad-

sorbed on the electrode surface and will be involved in the charge transport when a bias is applied on the junction. This scenario is contrary to the aim of our experiment, which is to measure single molecules properties and make it necessary to modify the surface morphology to get appropriate electrode tip geometry. Thus, the geometry of the nanoelectrode needs to be modified before use and sharp electrodes with small radius of curvature are desired.

Another reason to obtain a small radius of curvature is that the size of the electrode affects the conductance of the nanogap. If electrode with large radius of curvature are used, the nanogap resistance switching effect will be more pronounced because of the atom electromigration at multiple local sites on the metal surface [131].

Based on the above mentioned reasons, it is concluded that the nanogaps fabricated by the electron beam lithography are not appropriate to use in measuring charge transport properties of single molecules. Further modification methods are required to obtain nanogaps not only with reproducible and consistent sizes, but also with a small radius of curvature under 3 nm.

4.1.3. Fabricating nanogaps by focused beam etching

In the above mentioned sections, the fabrication of micro-scale structures by optical lithography and nanogap electrodes by electron beam lithography are discussed. In this part, the generation of nanogaps by cutting a nanowire by ionic etching is introduced.

Following the design of nanowire (Fig. 4.3), a nanowire was fabricated by electron beam writer on the bases of conducting leads fabricated by optical lithography. The nanowire was etched in the middle by focused ion beam and a nanogap with the size of 100 nm was generated (Fig. 4.12a). The exposed area of the etched electrodes was symmetric and very small about 0.01 μm^2. The electrodes were covered by three layers of PMMA for insulation (Sec. 5.1.4), and the measured thickness of the insulating layer was 400 nm (Fig. 4.12b). The ionic beam etching was also used in the work of Shi et al. [118], where a similar 100 nm gap was generated by the ion beam etched nanoelectrode. Blom et al. also employed the focused ion beam milling to fabricated highly reproducible 50 nm nanogaps [119].

Insulated nanowire was used in this work instead of bare gold electrodes used in the work of Blom et al. [119]. The advantage of using ionic etching is that the exposed area of the nanogap electrodes only depends on the cross section of the electrodes. This value is much smaller than the exposed area generated by an access window (5.8 μm^2, Sec. 4.1.4) and much lower electrochemical current can be expected from such small exposed area, which is desirable when measuring the low level current through molecules. However, the disadvantage of using focused ion beam is that it only cut the nanowire one by one, which is very time-consuming. Another problem is that the etched nanowire does not

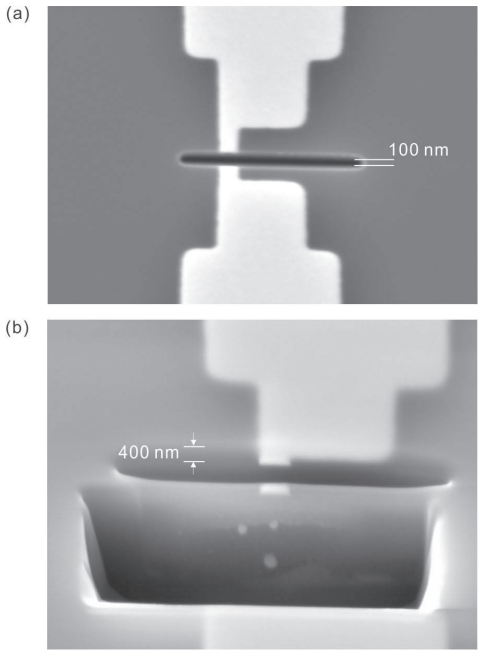

Figure 4.12.: Top view (a) and side view (b) of the nanogaps generated by etching into a nanowire.

have a sharp tip, which is not a favorable configuration for the following electrochemical modification as discussed in Sec. 4.1.2. Although the focused ion beam has the ability to shape the electrode to any geometry; much more effort is needed than the common lithography techniques. Therefore, this technique has not been used anymore in this work.

4.1.4. Insulation of the electrodes

Structuring insulating layer by optical lithography

In the above sections, the fabrication of micro-scale structures by optical lithography and nanogap electrodes by electron beam lithography were discussed. In addition, the nanogaps created by ionic beam etching were also demonstrated. The nanogaps fabricated by electron beam lithography were used for further electrochemical modification. Using electrochemical deposition/etching, the sizes of the nanogap can be fine adjusted and the surface morphology of the electrodes can be modified.

Before further treatment by electrochemical method, all the surface of metal electrodes need to be covered by organic or inorganic dielectric materials except the very tip of the nanogap electrodes and the contact pads. If the electrodes are not insulated well, the

electrochemical current will be very huge and cannot be used in any aqueous environment. Several groups fabricated nanogaps for using in liquid environment, but no insulating layer or no proper insulation was found on these nanogap electrodes. For instance, in the work of Kiguchi et al. [27], the electrodes were covered by hand with wax, and the whole notched area was exposed, which resulted in an electrochemical leakage current of 0.5 µA. Tian et al. used SiO_2 to insulate electrodes and access window with dimention of 50 µm was opened on top of the electrodes [132], while the electrochemical leakage current was not characterized. Kang et al. did not use any insulation procedures for the nanoelectrodes [28].

The maximum exposed area of the exposed surface can be estimated as following steps. Supposing tunneling current as low as 1 pA is measured, the capacitance current cannot exceed 1 pA, otherwise the electrochemical current would interfere with the tunneling current. According to Eq. (2.45) , the steady state capacitance current is vC_d and the maximum capacitance is 10^{-5} µF, given that the potential sweeping rate is set to 0.1 V/s. Considering the capacitance at gold/electrolyte [133] is in the order 10 µF/cm^2, the maximum exposed area should not exceed 100 µm^2.

In this work, both organic and inorganic materials were tested to insulate the electrodes. To open an access window on top of the nanoelectrodes, lithography techniques were used.

One possible option is using photoresist AZ 5214 as the insulating layer. The experimental procedures were same as Sec. 3.1.2 except that a different mask was used. Firstly, a layer of photoresist AZ 5214 was applied on the chip, on which the conducting leads and nanogap electrodes were already fabricated. Then an access window was opened by standard optical lithography procedures (Fig. 4.13).

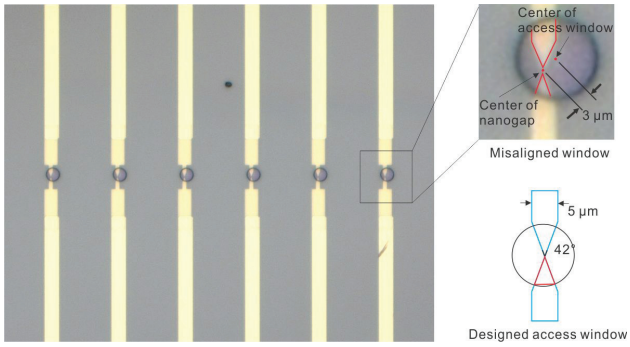

Figure 4.13.: Insulating metal electrode by photoresist (AZ 5214). Inset picture shows the access window on top of the nanogaps with misalignment between the access window and the nanogap center.

The access window for the nanogap was designed to be a circle right on top of the nanogap center with a diameter of 10 µm and an exposed electrode area of 2.9 µm^2 for each electrode which can be estimated from the designed pattern (Fig. 4.13), right lower,

red triangles). However, from the graph shown in Fig. 4.13, a misalignment between the center of the access window and center of the nanogap was observed. A displacement was measured at 3 µm between the center of the access circle and the center of the nanogap. A misalignment between the insulation layer and the tip of the electrode was also observed in the work of Tian et al. [132] and the displacement was estimated around 2 µm from the SEM images. For the work of Kiguchi et al. [27], the alignment between the insulating layer and the electrodes were not clear due to the lack of the data.

The alignment between the two structures has been achieved by the marker alignment (Fig. 4.2). The mask and the substrate have the same marker structure on the surface and to make alignment, the position of the markers on mask and substrate is required to coincide. However, several reasons made it difficult to obtain accurate alignment between the markers on the wafer and the markers on the masks. Firstly, the markers on the wafers were fabricated by optical lithography and the edge of the markers was rounded, which hindered the accurate alignment between markers. Secondly, the adjustment of positions of mask/substrate was performed under the optical microscopy. The focus depth of the microscopy at high magnification used in the mask aligner was very shallow, which made it very difficult to clearly observe the markers on the wafer and the markers on the mask at the same time. Another reason was that several mechanical operations were needed to perform the exposure, which would produce displacement between the wafer and the mask and generated misalignment between the center of opening window and the tip of the nanogap electrodes (Fig. 4.13).

The misalignment observed in Fig. 4.13 resulted in an exposed area of 5 μm^2 at one electrode and 0.5 μm^2 at the other electrode. Which makes it difficult to measure molecular properties in liquid since the electrochemical response of the two electrodes would be different. The electrochemical current can be examined by cyclic voltammetry. The cyclic voltammetry of the nanogap electrode with misalignment insulation is presented in Fig. 4.14.

From Fig. 4.14, it can be seen that the reduction peak value for the first electrode (0.08 nA) is five times smaller than the second electrode (0.4 nA). From the cyclic voltammograms, the electrode surface can also be estimated [134]. By integrating the reduction current peak over time, the total charge transferred at the electrode surface were calculated as 1×10^{-11} C and 1.1×10^{-10} C. Since the theoretical charge transfer density at gold surface is 448 $\mu C/cm^2$, the actual electro-active surface can be estimated to 2 μm^2 for the first electrode and 20 μm^2 for the second electrode. The surface area value calculated from the cyclic voltammograms was 4 times larger than the surface area calculated from the SEM images, which reflected the roughness of the electrode surface.

The result of the different exposed electrode area is that the electrochemical current

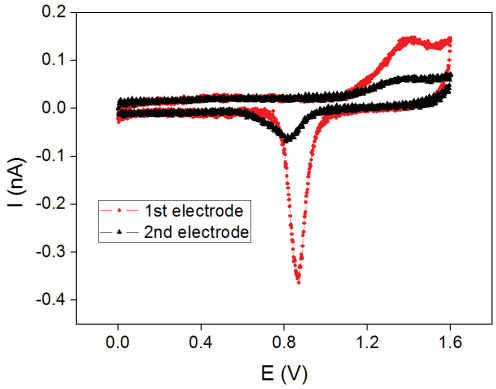

Figure 4.14.: Cyclic voltammograms from nanogap electrodes with misaligned access window.

through each electrode is different from each other even if the potential applied on each electrode is kept at the same level. An example of the asymmetrical electrochemical current is the asymmetrical deposition caused by different depositing current. When the two electrodes were immersed in aqueous solution, performing electrodeposition, the different exposed electrode surface would cause asymmetrical deposition: more gold atoms were deposited at one electrode than the other electrode. One instance of asymmetrical deposition is shown in Fig. 4.15, which demonstrated that more gold atoms were deposited to the left electrode than the right electrode. This situation was also appeared in the work of Tian et al. [132], where more atoms were deposited on one electrode.

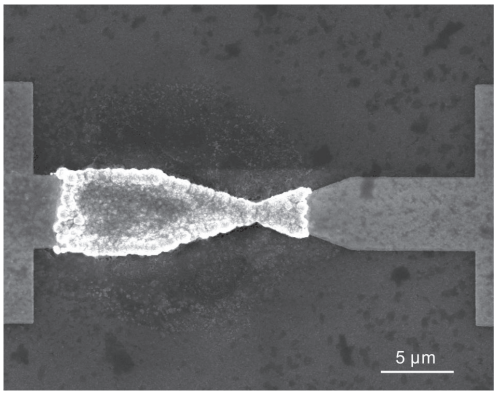

Figure 4.15.: Asymmetrical deposition caused by the different exposed surface area of the electrodes.

In molecular electronics, measuring the I-V curves through molecules is usually required. In aqueous environment, the measured current contains the electrochemical current at electrode/electrolyte surfaces of both electrodes. If the electrochemical current is different

for each electrode at the same potential, the total electrochemical current is different when the bias between the two electrodes changes directions, causing asymmetric I-V curves. For instance, the electrochemical current for a configuration of 5 μm^2/1V, 0.5 μm^2/-1V is different from the opposite configuration 5 μm^2/-1V, 0.5 μm^2/1V (here, "5 μm^2/1V" refers to an electrode with exposed areas of 5 μm^2 and the potential applied on this electrode is set to 1 V). This situation is not desirable for measuring I-V curves through molecules since the electrochemical current imposed to the tunneling current would be different for the forward sweeping and backward sweeping and the resulting I-V curves will be very difficult to explain. For instance, asymmetric I-V curves were observed in the work of Tian et al. [132], but no satisfactory explanation was provided.

Since the misalignment problem was difficult to eliminate, the structuring of insulating layer by optical lithography was not appropriate in this work. Thus, more accurate method like electron beam lithography was used.

Structuring insulating layer by electron beam lithography

To minimize the misalignment problem, electron resists PMMA was used as insulating layer and electron beam lithography was used to form the access window. Since the thickness of single PMMA layer (PMMA 600k, 6000 rpm) is around 200 nm, it is not enough to insulate the electrode. Thus, three layers of PMMA (600k/900k/600k, Sec. 3.1.4) were spin coated on the wafer then the normal electron beam lithography procedures were applied (Sec. 3.1.3).

The PMMA is resistant to common acid electrolytes (sulfuric acid up to 10%) and base electrolyte (potassium hydroxide 40%). In our experiments, only electrolytes with pH value from 2.0 to 10.0 were used, so the PMMA layer could provide enough chemical resistance. The representative structures are shown in Fig. 4.16.

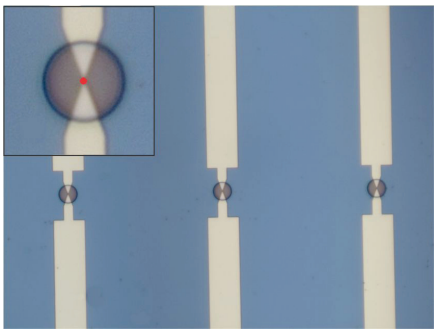

Figure 4.16.: Insulating electrode by PMMA layers. An access window with diameter of 10 µm is right on top of the center of the nanogap.

Using PMMA as the insulating material, the alignment between the nanogap and the

access window was fairly good and the position of the nanogap center and the circle center nearly coincided. The size of the exposed area in both nanogap electrodes was equal under the resolution of optical microscope, with a total exposed area of $5.8\,\mu m^2$($2.9\,\mu m^2$ for each electrode), which agreed with the designed value (Fig. 4.4). The electric characterization of the insulating layer will be discussed in the next chapter.

During the encapsulation, the overlay area between the optical lithography fabricated structures and the electron beam lithography fabricated structure were found to easily introduce insulating failure and produce unexpected electrochemical leakage current. The reason was that the height of the overlay area was twice as high as the height over other area, which resulted in a thinner insulating layer at the overlay area than at other part. To deal with this problem, one-step electron beam lithography was used to fabricate both the conducting leads and the nanogap electrodes. In this way, overlay area was eliminated and the height of the insulating layer was the same elsewhere. This treatment lowered the probability of generating electrochemical leakage current caused by uneven covering of PMMA layers.

Inorganic insulating materials

In above sections, the insulation of nanoelectrodes by optical lithography and electron beam lithography was introduced and the material is either photoresist AZ 5214 or electron resist PMMA. In next part, the inorganic material SiO_x/SiN_x as insulating material is described.

SiN_x is a widely used insulating material and has good resistance to the aqueous solution or organic solution [112,135–137]. Here, a layer of 200 nm SiN_x was applied on the nanogap chip by PECVD (Sec. A.4). The thickness of the SiN_x was chosen as 200 nm. The next step was to open the access window in the SiN_x layer. If the 200 nm SiN_x needs to be etched, very thick resists are required, since the plasma also etches the resists. Thus electron resist PMMA is not suitable here, since the thin layer of PMMA would be etched away in RIE. Therefore, photoresist AZ 5214 was used and the access windows were opened by optical lithography.

Firstly, AZ 5214 was applied on the chip and an access window was opened by optical lithography. Then the chip was etched by RIE (Sec. 3.1.4) and an access window in the SiN_x layer was opened on the nanogap electrodes (Fig. 4.17).

From Fig. 4.17, it can be seen that the very tips of the nanogap electrodes were lost during the fabrication process which was discussed in the previous chapter (Fig. 4.6). The RIE process was successful: the nanogap electrodes were exposed and the SiO_x substrate was not been damaged. The edge of the access window was smooth but under-etching was observed. This type of under-etching was also observed in the word of Howell et al., where one-dimensional silicon nanogaps were fabricated by top-down methods [138]. The

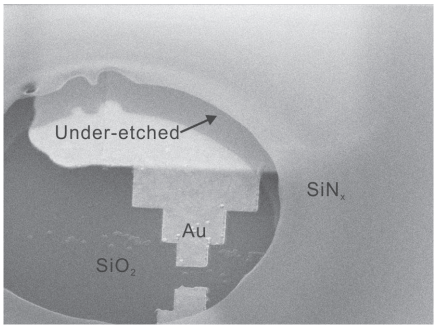

Figure 4.17.: Silicon Nitride insulated chip, an access window was opened on the nanogap.

misalignment between the access window and the nanogap center was also observed. This was clear because of the optical lithography.

Although Tian et al. used SiN_x to insulate the gold electrodes [132], in our work, we found SiN_x is not a suitable material for insulating electrodes. The problem of using SiO_x/SiN_x as insulating material is the weak adhesion between the gold electrodes and the SiN_x layer. It was found that even slight mechanical force applied by probe station needles can make the SiN_x layer peeled off from the silicon substrates. Thus, the SiN_x insulating layer was not further used and PMMA insulating layers were employed. The mechanical stability of PMMA layer is quite good and no peeling off of the PMMA layer was observed during our experiments. Besides, the electrolyte used in this work is ordinary inorganic acid or base and PMMA layer showed resistance to such electrolytes.

Summary

In summary, gold nanogap arrays consisting of 29 pairs of facing electrodes were fabricated by electron beam lithography on a silicon wafer (Fig. 4.18a). The wafers were encapsulated by PMMA layers with an opening window above the electrode tip, allowing a small area exposed to the electrolyte (Fig. 4.18b). The insulating PMMA cover was aimed to reduce the parasitic current from electrode/liquid interface. The triangle shape of the electrode tip provided a template for the electrochemical deposition, and supported the fabrication of nanoelectrodes with sharp tips. The conducting leads had a width of 10µm, ensuring low feed line resistance (100 Ω) and little joule heating. The SEM image of the electrode tip with a gap size of 150 nm was shown in Fig. 4.18c.

From the SEM image, the electrode surface does not show obvious residuals from the fabrication processes and the roughness of the surface is homogeneous on the nanoscale; although, some residue particles exist on the edge of the electrode, which were possibly generated during the lift-off process. We did not see any influence from such residue

particles during the electrodeposition process.

An initial gap size of 150 nm was chosen as a compromise between fabrication efforts and deposition time. Since larger electron beam size can be used in larger structures. Using electron beam lithography smaller electrode gaps down to 20 nm could be generated; however, the processing time and defecting rates would increase also. On the other hand, wide electrode distance would lead to very long deposition time due to the very small deposition rates we used in our experiments.

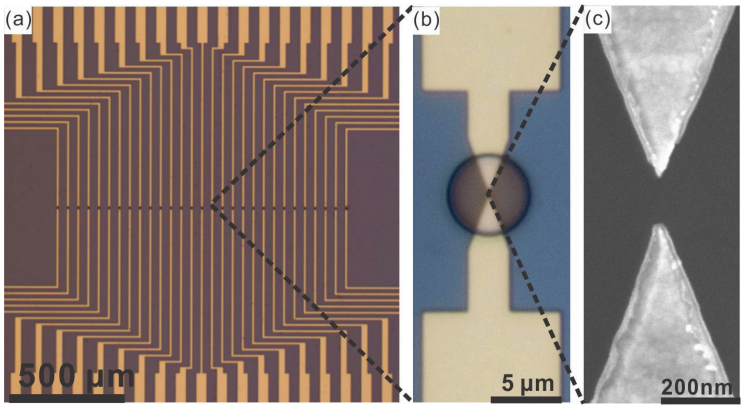

Figure 4.18.: Summary of the fabricating nanogap electrode by electron beam lithography.

4.2. Electrochemical modification of nanogap electrodes

In last chapter, the fabrication of nanogap electrodes by electron beam lithography was discussed. The size of the nanogap cannot be adjusted reproducibly and the radius of curvature at the electrode tip was too large for the incorporation of single molecules. To overcome the problems, electrochemical modification methods were applied for the modification of the nanogap electrodes.

In this chapter, the results of modifying surface morphology of nanogap electrode and fine tuning the gap size by electrochemical methods are described. The cyclic voltammetry was firstly investigated on both macro-scale electrodes and nanoscale electrodes. The CV of nanoscale electrode showed a steady state electrochemical response. Since the electroless deposition is lack of control so that the surface morphology is difficult to modify [139], this technique was not used in this work. Here, potentiostatic deposition techniques were employed to deposit atoms on the predefined nanogap electrodes. The mechanism of nucleation and crystal growth was studied by transient current analysis. The surface morphology modification by the deposition potential was also investigated. Potentiodynamic deposition

was tested but this deposition routine was not further used in this work due to the lack of morphology control. The gap sizes were conveniently tuned by potentiostatic electrodeposition and etching. Atomic scale junctions can be formed and quantized conductance was observed. Nanogaps with the size of down to sub 1 nm can be deposited, which were stable at least in 25 seconds.

4.2.1. Cyclic voltammetry

Choosing electrolytes for electrodeposition

Many factors influence the electrodeposition process such as overpotential, current density and buffer composition.

Different electrolytes containing copper [140] and platinum [113] have been employed in the electrodeposition process. Nanogaps fabricated from gold containing electrolyte are typically not stable due to the high mobility of gold atoms; although gold is an important material for the fabrication of molecular devices because of its ability to be polarized at large potential ranges. In molecular electronics, large voltage biases between electrodes allow for the electrical addressing of molecular orbitals with larger energy separation from the Fermi level. This is difficult to achieve for copper and catalytically active platinum. Furthermore, there exists a well established surface chemistry, which is based on thiol and amino linker residues and can be utilized when attaching functionalized molecules to electrodes. Recently, stable gold nanogaps were fabricated using iodine-containing medium which featured slow electrodeposition rates [118]. However, iodine is known to adsorb strongly into gold surfaces and might affect the binding of target molecules [141].

The simple cations of gold are not stable in aqueous medium and only complex form of metal ions can be employed in the electrochemical deposition process. Typical gold deposition solutions are $[Au(CN)_2]^-$, $[AuCl_4]^-$, $[Au(SO_3)_2]^-$, $[Au(S_2O_3)_2]^{3-}$. The gold cyanide buffer is very easily to generate toxic gas, so it was not used here. The sulfite thiosulfate solution is a new type of gold deposition solution developed during the last decade [142,143]. The pH of sulfite thiosulfate buffer is in neutral range so it is compatible with the photoresist layer and produces little damage to the photoresist. However, during the preparation of sulfite thiosulfate buffer, the pH value needs to be strictly kept in a narrow range and this process is not easy to control, so this type of depositing buffer was not used in this experiment.

In our experiment, a conventional chloride-containing gold (III) solution was employed to fabricate nanogaps. The solution has been studied for many years [144, 145] and the preparation of such solution is very simple. In this systems, the active metal ions are $[AuCl_4]^-$ and the overall deposition reaction can be expressed as the following steps [146]:

$[AuCl_4]^- + 3e^- \rightarrow Au + 4Cl^-$

Detailed studies indicate that the reduction of gold complexes $[AuCl_4]^-$ to gold atoms includes several steps:

$[AuCl_4]^- \rightarrow [AuCl_2]^+ + 2Cl^-$

$[AuCl_2]^+ + 2e^- \rightarrow [AuCl_2]^-$

$[AuCl_2]^- + e^- \rightarrow Au + 2Cl^-$

High concentration of lithium chloride was added in order to inhibit the disassociation of the $[AuCl_4]^-$ complex to the $[AuCl_2]^+$ complex.

Cyclic voltammetry for both macroelectrodes and nanoelectrodes

Usually, performing cyclic voltammetry (CV) is the first step of electrochemical analysis, since the CV provides information about the diffusion mode, redox potentials and so on.

Firstly, cyclic voltammetry in macro-scale setup was performed (Sec. A.6) and the results were shown in Fig. 4.19.

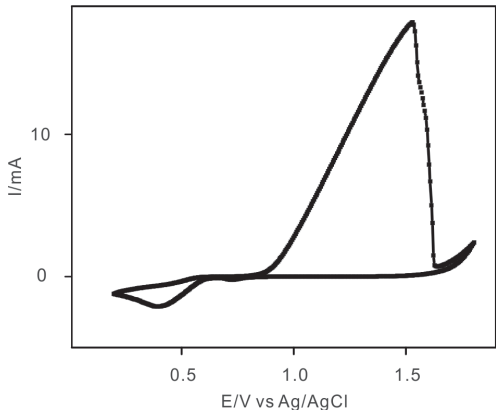

Figure 4.19.: Cyclic voltammetry of gold deposition solution with macro gold electrodes

For the macro electrode (Sec. A.6), cyclic voltammetry was performed and a reduction peak was observed at 0.4 V. The overall shape of the CV of macro electrodes is similar as the CV of stationary glassy carbon electrodes [145]. The oxidation of the gold wire started at 0.8 V and had a maximum at 1.5 V. At potentials more negative than 0.7 V, the cathodic current increase sharply which indicate the crystal growth in three dimensions. At potential 0.4 V, the cathodic current reached the maximum and deposition process was then controlled by diffusion at potential more negative than 0.4 V. The diffusion limited deposition process also reflected in the limiting diffusion current during the reversed anodic scan.

Since the tuning of gap size and modification of the electrode morphology is performed on the nanoscale electrodes and the diffusion mode in the nanoscale is different from the diffusion in macro-scale, it is necessary to investigate the cyclic voltammetry of nanogap electrodes directly on chip in order to obtain the required potential for deposition or etching.

The CV of a gold nanoelectrode in chloroauric acid depositing solution was shown in Fig. 4.20. For the nanoelectrodes, the peak reduction current (10 nA) was five orders of magnitude smaller than that of the macro wire (1 mA) due to the very small surface area exposed to the electrolyte (see Fig. 4.16). This value is in the same order as in the work of Meszaros et al. [140], where small access window was also used in insulating layers. However, the reduction current of electrodes were not characterized in the work of Chen et al [120], Kervennic et al. [147]. The oxidation range of the nanoelectrode was not measured because the nanoelectrode would be dissolved very easily at anodic potentials (the dissolved electrodes were not shown here). The CV shape of the nanoelectrode is different from that of the macro electrode, because the diffusion mode for the nanoelectrode is semi-spherical (Eq. 2.51), whereas a unidirectional diffusion can be assumed for the macro electrodes. The difference between the unidirectional diffusion and radial diffusion has been discussed in Sec. 2.2.4.

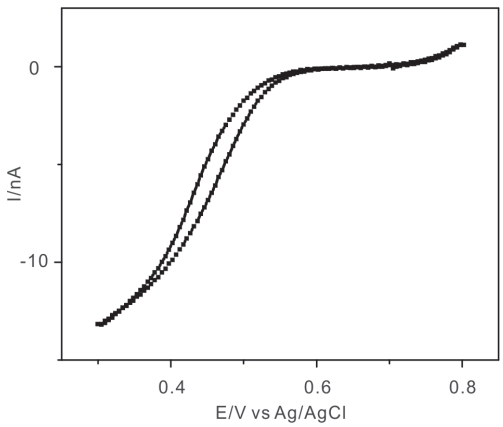

Figure 4.20.: Cyclic voltammetry of gold deposition solution with nanoelectrodes

In the following part, the relation between overpotential and electrode morphology was investigated and the morphology of the deposited material was found to be directly related to the overpotential. Using this dependency, we established a routine to fabricate nanogaps with needle-like surface on predefined facing electrodes and investigated organic molecules incorporated in the electrodeposited nanogaps.

4.2.2. Potentiostatic deposition and morphology modification

One of the used deposition methods is the potentiostatic deposition. In this method, the applied potential is set constant and the depositing process is monitored by the electrochemical current. The deposition process can be described by nucleation on the surface and the following crystal growth. The mechanism of nucleation has been intensively studied on macroscale electrode like carbon or highly oriented pyrolytic graphite. However, the mechanism of nucleation and crystal growth on gold nanoelectrode has not been studied yet. Therefore, the mechanism investigation of electrodeposition on the nanoelectrode is first presented in the following part.

Mechanism of nucleation and crystal growth

The mechanism of nucleation and crystal growth in nanoscale was investigated by the transient current analysis. Fig. 4.21 shows depositing current curves recorded at different potentials in the range from 0.52 V to 0.60 V. The current transient exhibits a shoulder for potentials smaller than 0.58 V. As the applied potential was lowered, the current maximum became more pronounced and its height increased and position shifted negatively as the potential became more cathodic, which is typical nucleation current and can be explained by classical nucleation theory [148–150]. After about 5 s, the current reached a plateau and the depositing current was mainly determined by the overpotential according to Butler-Volmer equation (Sec. 2.2.3). Then the increase of the electrochemical current can be observed due to the increasing surface area with the proceeding deposition process. At larger overpotentials (the potential between the applied potential and the equilibrium potential, Sec. 2.2.3), the depositing rate was much higher than the rate at small overpotentials. Thus the electrochemical current increased more quickly at 0.52 V than at 0.56 V. Therefore, choosing the right potential in the potentiostatic deposition method is very important, since the potentials not only control the mode of nucleation but also the total deposition. Furthermore, different deposition modes result in very different surface morphology, and the nanogap morphology is an important parameter when incorporating the molecules between the nanogaps. The relation between deposition potential and the surface morphology of the deposited material will be discussed in the next parts.

After simple analysis, the peak position (i_{max}, t_{max}) in the depositing curves (Fig. 4.21) can be obtained. Then, the transient current curve $(i \,\text{vs.}\, t)$ can be easily converted to dimensionless $(i/i_{max})^2 \,\text{vs.}\, (t/t_{max})$ plots. Two representative transient curves at 0.52 V and 0.54 V were transformed to dimensionless plots (Fig. 4.22). The theoretical curves corresponding to ideal progressive and instantaneous nucleation were also presented in the same plot for comparison (Fig. 4.22) according to Eq. 2.56 and Eq. 2.57. In this figure,

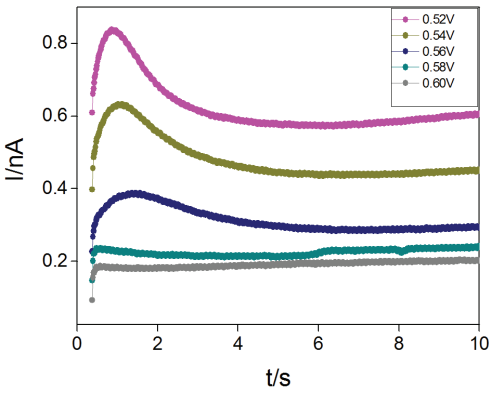

Figure 4.21.: Initial current during depositing gold atoms on a gold nanoelectrode at different potentials.

if the experimental curves fit into the theoretical progressive nucleation curves, then the actual nucleation progress is assumed to be in progressive mode; if the curves fit into the theoretical instantaneous nucleation curves, then the actual process is supposed to be in instantaneous mode [86, 151]. From Fig. 4.22, it was seen that the transient current obtained at 0.52 V and 0.54 V do not fit either of the theoretical curves. This is typical for all chronoamperometric curves obtained for Au (III) deposition with high concentration of LiCl [145]. In the longer time, the curves approach instantaneous deposition. The curves at other potential have similar features. The deviation of dimensionless plots from the ideal models indicates that it is difficult to categorize the nucleation mechanisms as purely instantaneous or purely progressive.

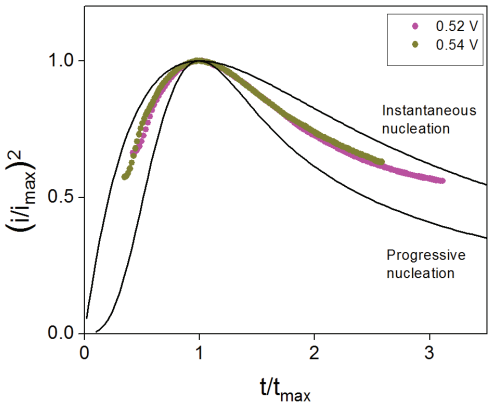

Figure 4.22.: Non-dimensional $(i/i_{max})^2$ vs. (t/t_{max}) plots of potentiostatic transient current for deposition of gold compared to the theoretical curves corresponding to the models of progressive nucleation and instantaneous nucleation.

The growth modes can be determined by analyzing the rising part of the transient current (0–1 s). The i vs. t^b plots give information about the deposition kinetics according to b value (Table 2.1) [86, 87]. For the transient current at 0.52 V, the relationship was plotted with different b values for comparison (Fig. 4.23). It can be seen that when b is 3/2, plot is linear in the range from 0.6 s to 1 s, which indicates the deposition was progressive nucleation and diffusion limited growth, according to table 2.1. It is unclear whether the diffusion mode is planar or spherical from the i vs. t^b plots.

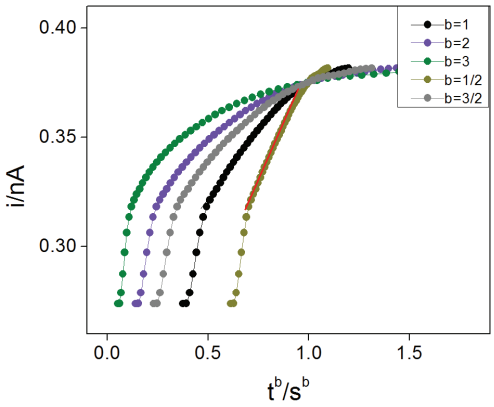

Figure 4.23.: i vs. t^b plots with different b values to investigate the mechanisms of nucleation and growth.

The fitting of Cottrell equation (Eq. 2.47) of the current time transient is displayed in Fig. 4.24. It can be seen that the early stage of the deposition (the first 6 seconds) fit the Cottrell equation well, which indicates that the deposition was diffusion-controlled at the initial stage but in longer time the deposition was not diffusion limited anymore. This result agrees with the work of Martin et al. [13], where the first 7 seconds deposition was under diffusion control.

From the transient current curves (Fig. 4.21), it can be seen that the deposition current reaches a plateau after about 5 s, the plateau was at different current values for different deposition potentials. The difference of the plateau values can be explained by the Butler-Volmer equation: the $\log i$ vs. η (η is the overpotential) plot, which is also known as Tafel plot (Fig. 4.25), exhibits a linear relationship, which agrees with the Butler-Volmer equation (Eq. 2.41) and indicates that the deposition at this stage was charge transfer controlled. Otherwise, if the deposition is diffusion controlled, the deposition current at different depositing potential would converges to same value. The diffusion controlled deposition was observed in the work of Komsiyska et al. [152].

In summary, the analysis of transient current indicates that at first stage of deposition, the nucleation is progressive and the growth is diffusion limited (Fig. 4.22 and Fig. 4.23),

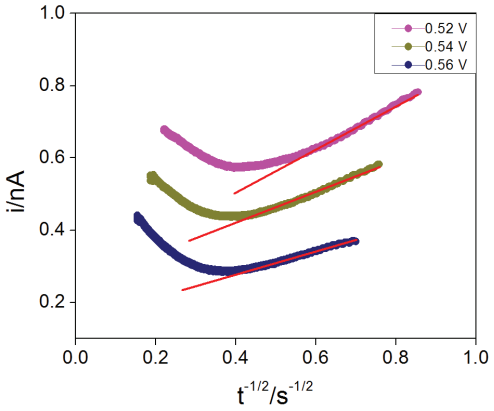

Figure 4.24.: Cottrell fitting to the transient current. The first stage of the deposition is almost linear (the red line).

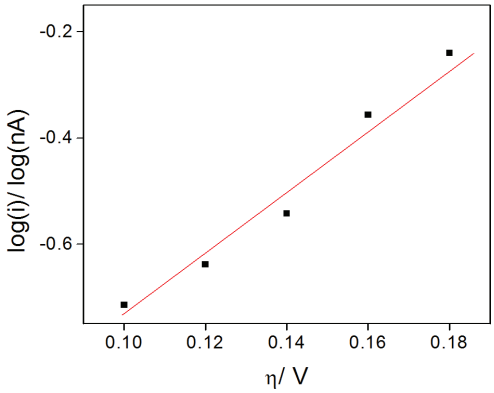

Figure 4.25.: Linear relationship between $\log i$ and overpotential in the steady state indicates that the deposition follows Butler-Volmer equation.

however, in the long times, the growth turns into kinetic controlled (Fig. 4.24).

Dependency of the surface morphology on the depositing potentials

To investigate the relationship between the deposition potential and the surface morphology, a series of deposition experiments was performed at potential from 0.4 V to 0.6 V. A electrochemical setup with four-electrode electrochemical configuration was used: the facing nanoelectrodes were used as two independent working electrodes. An Ag/AgCl micro electrode was used as the reference electrode and a platinum wire was used as counter electrode. The potential of the two working electrodes were set to a bias of 13 mV in order to monitor the tunneling current between the two electrodes when they were getting closed enough.

The presence of multiple parallel pairs of nanoelectrodes on the chip provides a convenient environment for performing series of deposition. After deposition at one pair of electrodes, simply electrically connect the next pair of electrode to the potentiostat by placing the tungsten needles in the probe station and adjust the deposition potential accordingly. Part of the deposited chip was shown in Fig. 4.26.

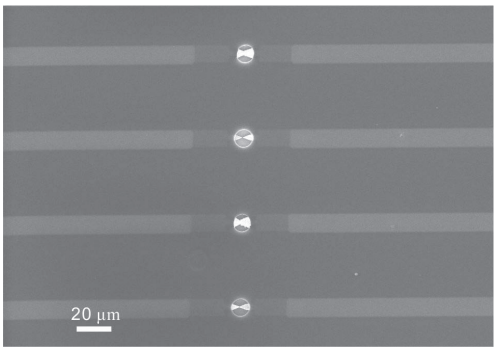

Figure 4.26.: Potentiostatic deposition at different potentials performed successively on nanogap electrode arrays.

A close look by SEM revealed the influence of the deposition potentials on the morphology of the deposited gold material (Fig. 4.27). Typical SEM images (Fig. 4.27a, b, c) represent the nanogaps deposited at potentials around 0.45 V (a), 0.55 V (b) and 0.6 V (c), respectively. By comparing (a) and (c), it is observed that high overpotentials produce smooth, bump-like gold depositions between the nanogaps and low overpotentials produce jagged gold depositions between the nanogaps.

The smooth nanogap has very grainy structure. The radius of the surface curvature of various tips was estimated to 500 ± 50 nm, which formed quasi-parallel contact between electrode pairs. Nanogaps with such planar morphology would incorporate thousands of molecules at once when forming metal/molecule/metal junctions (see Fig. 4.11). The radius of surface curvature in Fig. 4.27b was around 50 ± 5 nm, which was very close to the nanogap electrodes fabricated by electron beam lithography. The radius of curvature of the sharpest gold needles was smaller than 5 nm. The difference of morphology between the facing electrodes at one electrode pair was almost negligible in all the deposition potentials, although a small bias (13 mV) was applied between the facing electrodes.

Radius of curvature of needle-like electrodes

The electric field between the two nanogap electrodes is very high, especially in the configuration of needle-like nanoelectrode. It is known that the strong electric field can affect the electrodeposition processes [153] and one possible reason for the growth of needle-like

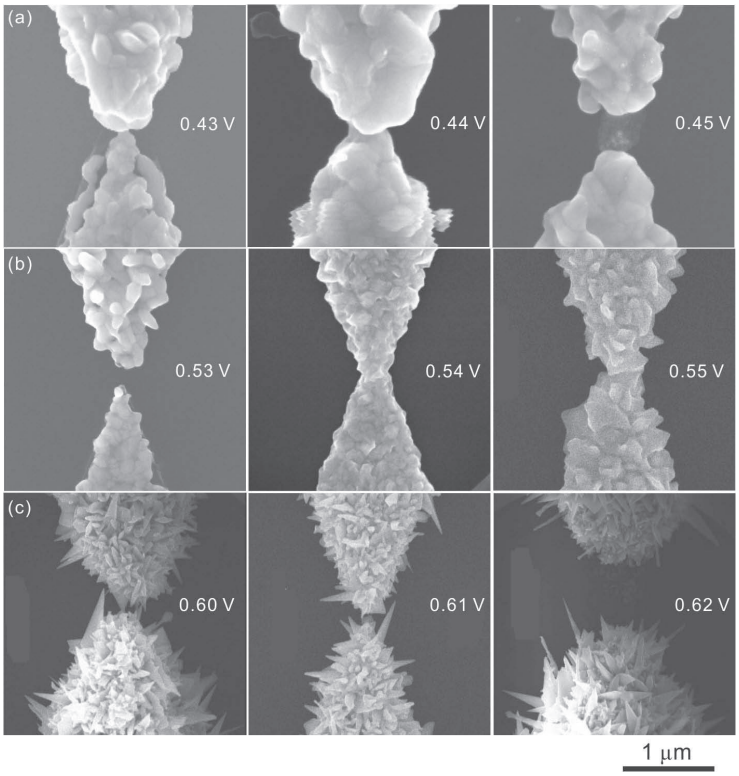

Figure 4.27.: Typical electrode morphology under different deposition potentials, which demonstrates the morphology dependency on the potentials.

electrodes is due to the high electric field. To verify this reason, we deposited the electrodes without the influence of the strong electric field by depositing only one of the two electrodes (Fig. 4.28). It can be seen that needle-like electrodes are still formed, which indicates the mechanisms of forming needle-like electrodes is not electric field induced.

The tip angle of the extruding needles was measured from the SEM images and the average angle was 19°, which is much smaller than the tip angle of the nanoelectrode fabricated by electron beam writer. More importantly, the radius of curvature at the tip of the extruding needle was very small and was estimated to 1–2 nm (due to the limitation of SEM resolution, the standard error is difficult to estimate), which would incorporate less than 10 molecules as estimated from the model (Fig. 4.11). Accurate measuring the radius of curvature was very difficult since the radius of curvature was out of the SEM resolution. This level of sharpness of the nanoelectrodes was much better than the electrodeposited nanoelectrodes obtained by other groups [120, 128, 154], where the radius of curvature was in the order of several hundreds of nanometers.

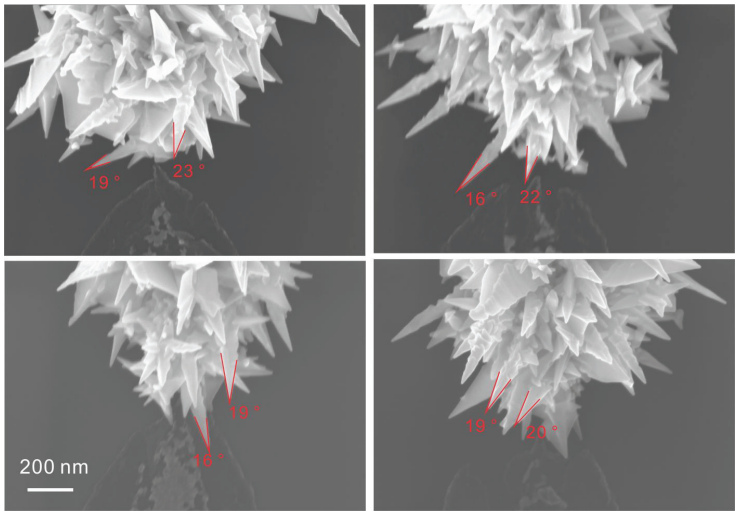

Figure 4.28.: Depositing needle-like nanoelectrode on one electrode to eliminate the influence of electric field between the two electrodes.

For the deposition of sharp nanogaps at low overpotential, a non-equilibrium mechanism can be assumed. The nucleation process is progressive and the initial growth is diffusion limited (see previous part), which leads to deposition on energetically favorable sites (step edges, defects). The following crystal growth is actually kinetic controlled, where the growth is potential limited. Low overpotential as well as low concentration of electrolyte results in low nucleation rates. Therefore, three dimensional nucleation growths would turn into anisotropic nucleation growth at low overpotential [13]. Furthermore, the diffusion of gold atoms across step edges is of significant importance for the actual shape of generated mounds. Suppressed interlayer diffusion as presumably present for low deposition overpotentials leads preferably to tapered mounds while strong diffusion across step edges results in rounded deposits [155]. The suppressed interlayer diffusion leads to a narrowing of the terrace diameter of each addition layer deposited, which resulted in the needle-like structures.

4.2.3. Potentiodynamic deposition

Besides the potentiostatic deposition, the potentiodynamic deposition was also tested, in which the potential was swept dynamically during the deposition process. Fig. 4.29 shows an example of potentiodynamic deposition where the potential was swept from 0.5 V to 0.51 V. The potential started from 0.51 V and swept negatively to 0.5 V with a speed of 50 mV/s. It can be seen that the electrochemical current increases continually with the potential cycling.

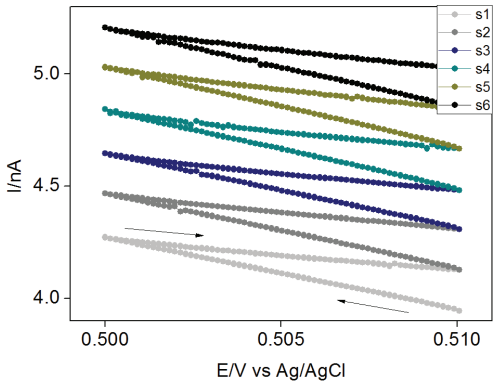

Figure 4.29.: Increased current in the potentiodynamic deposition process.

The potentiodynamic deposition technique is widely used in depositing organic polymers such as Polyaniline(PANI) since with this method the deposited PANI films have high electrochemical stability [156]. However, in this work, the morphology of the deposited material is a more important factor to consider when measuring the molecules between the electrodes. The SEM images of electrodes by the potentiodynamic deposition showed rather smooth surface and large radius of curvature (Fig. 4.30). Thus, the potentiodynamic deposition method was not further used in modifying predefined nanogap electrodes.

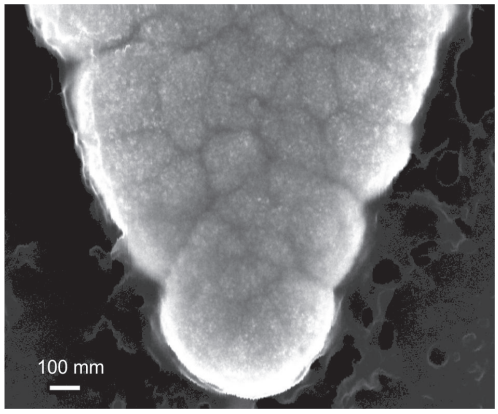

Figure 4.30.: Nanoelectrode with large radius of curvature by potentiodynamic deposition.

4.2.4. Fine tuned nanoscale gaps and atomic scale junctions

In the last part, the morphology modification by potentiostatic deposition was discussed. Another important aspect to use nanoelectrode for contacting single molecules is the stability and reproducibility of generating desired gap sizes. The following part introduces the

stability of the electrodeposited nanogaps or atomic scale junctions as well as the ability of generating nanogaps with desired gap sizes by potentiostatic deposition.

Electrodeposited nanogaps and the stability

When gold atoms deposited on the predefined nanogap electrodes, the size of the nanogap will be decreased and finally connected. During the electrodeposition, the deposition process can be stopped at the preset conductance value, creating nanogaps with preset sizes.

The conductance of three exemplary nanogaps fabricated by electrodeposition is shown in Fig. 4.31, where the deposition was stopped and hold stable at $1\,G_0$, $0.3\,G_0$, and $0.06\,G_0$ in solution over 25 seconds. This order of stability is not as good as the electrodeposited Cu nanogap [113], in which a molecular-scale gap was stabilized within 1000 seconds. It is mainly because the gold atoms are more mobile than the copper atoms so that the gold nanogap is more difficult to stabilize than the copper nanogap. The current was measured immediately after stopping the depositing process at the preset value of $1\,G_0$, $0.3\,G_0$, and $0.06\,G_0$, which corresponded to a gap size of sub 1 nm. The current fluctuations around $1\,G_0$ have been observed before [113] and were possibly caused by the gold atom rearrangement. Such stability characterization can be performed at any gap size. The atom point connection status ($1\,G_0$), which represents the transition between nanogap and connection, was more difficult to hold and displayed more noise than other nanogaps.

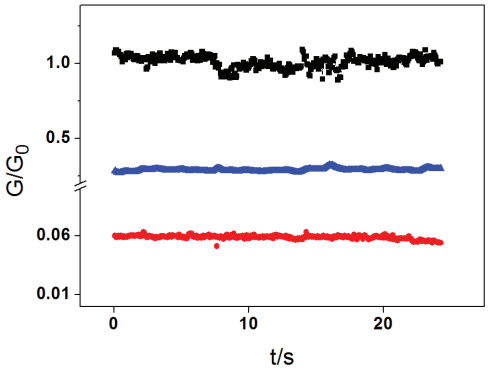

Figure 4.31.: The nanogaps fabricated by electrodeposition are hold stable over 25 seconds in solution.

Exemplary SEM images of deposited nanogaps under high overpotential and low overpotential are displayed in Fig. 4.32, respectively. The gap size is decreased to sub 1 nm by monitoring the tunneling current. From the SEM images, the gap size is small but difficult to measure due to the resolution of the microscopy.

Note that for the needle-like nanogap electrodes, the nano-needles extrude from the

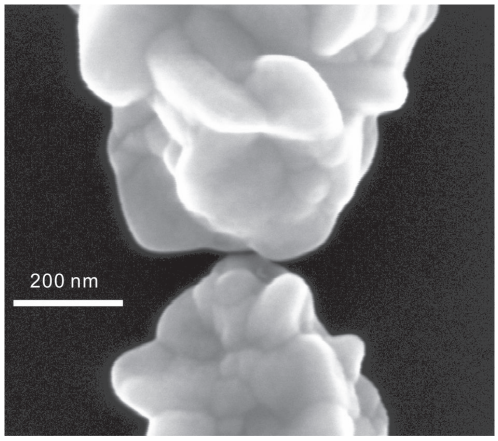

Figure 4.32.: Sub 1 nm nanogap formed by electrodeposition under high overpotential.

surface randomly, and the actual contact sites are randomly formed. In other words, the nanogaps may not be formed between the tips of the nano-needles, but possibly between the tips and the edges of the nano-needles as labeled in the Fig. 4.33.

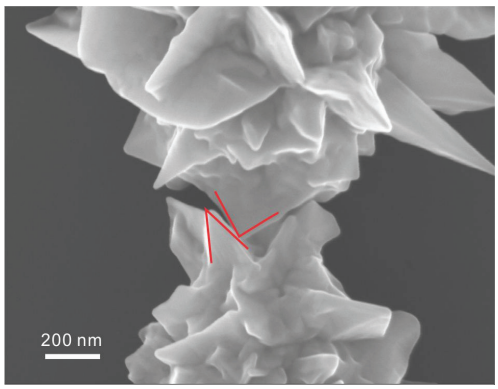

Figure 4.33.: Sub1 nm nanogap formed by electrodeposition under low overpotential.

After generating a nanogap of a predefined size (predefined conductance), the gold solution can be removed and the chip can be operated under conditions appropriate for respective tasks. For instance, the nanogap can be operated in solution, in vacuum, as well as under ambient conditions. However, during changing the experimental conditions, certain variation in the gap distance would occur due to the absence of potential control. This distance variation affects the tunneling current and demands an evaluation of the nanogap before incorporating any molecules. In most cases the variation of the conductance of the nanogap was within two orders of magnitude which corresponds to a change of the distance by several Ångströms. This kind of accuracy is difficult to achieve by employing only

lithography techniques.

Here, 80% of the deposited nanogaps can be maintained within the molecular scale after stopping the depositing process. 10% of the deposited nanogaps recede to large gap sizes (transient conductance lower than $10^{-4}\,G_0$) and 10% would jump to total connection (transient conductance larger than $50\,G_0$). Practically, if the nanogaps recede to wide gap, the gold deposition can be started again until the optimum gap size is obtained [1].

Quantized conductance of the atomic scale junctions

When depositing gold atoms onto the nanogap electrodes, the distance between the two facing electrodes decreases continually and the gap is finally closed by single or several gold atoms; then more gold atoms are deposited and the connection gets thicker and thicker. The special connection state where the two facing electrodes are bridged by only one or several atoms is referred to as atomic scale junction. The formation of the atomic scale junction process can be monitored the appearance of the quantized conductance.

One example of the conduction traces recorded during the fabrication process is displayed in Fig. 4.34. The quantized conductance was observed when atomic scale junctions were formed (Fig. 4.34 inset). The potential of one working electrode was set to 0.6 V and the other was set to 0.613 V. The current between the facing electrodes was recorded after a droplet of electrolyte was put on top of the electrodes and the potential were applied on both electrodes. The overall depositing time was about 30 minutes. Only the last 25 seconds of the deposition process are shown in Fig. 4.34. At first stage of the presented curve (until 20 s), the tunneling current was nearly zero. The current measured at this stage can be assigned to the electromagnetic noise and the electrochemical depositing current. With more gold atoms deposited on the electrodes, the distance between electrodes was narrowed and the conductance began to rise. At the last stage, the tunneling current increased sharply as the electrodes came into contact.

Quantized conductance appeared when the electrodes are bridged by several gold atoms, forming thin neck structures. The small steps below $1\,G_0$ can be explained by the relaxation of gold atoms and have been reported [157]. This steps in the tunneling region also indicates the discrete nature of atoms, which leads to a discrete change in the gap size [113]. A canonical Monte Carlo simulation with embedded atom potentials was performed to explore the reasons for stepwise changes in the tunneling current during the electrodeposition [158]. This model indicated that the change of distance depends on the relative orientation of nanoelectrode and the low-index plane (jkl) of the nanoelectrodes.

The depositing process can be stopped by the potentiostat at the moment when the current reaches a preset value. The preset value of tunneling current can be chosen as the electrode distance is approximate to the size of the molecule that would be integrated into

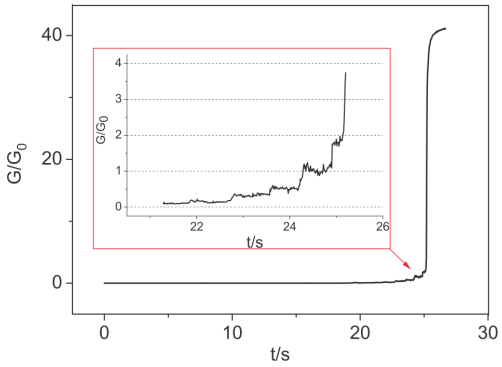

Figure 4.34.: Conductance plateaus are observed during the deposition and the plateau as $1\,G_0$ can be assigned to the formation of atomic scale junction.

the nanogap subsequently. In this example, the deposition process was stopped when the gap was totally connected to illustrate the whole depositing process.

It was, in general, difficult to observe quantized conductance for the smooth nanogaps which can be further obtained by depositing at high over potentials. Usually the deposited atomic scale junctions collapsed right after stopping the deposition process. Keeping the gap at atomic scale junctions was almost impossible. This situation was probably caused by the large radius of curvature, which leads to quasi-parallel interface between electrodes, making it difficult to form thin-neck structures.

If the deposited nanogaps jump to total connection, electrochemical oxidation can be applied on the junction in the same depositing buffer, then the gold atoms on the surface of the electrode will dissolve into the buffer and the connection can be opened again. By simply setting the potential applied on the working electrode to the anodic potential (for example 0.8 V vs. Ag/AgCl reference electrode) as shown in Fig. 4.35, the deposited gold atoms dissolved into the electrolyte and the connection opened, resulting in the exponential decrease of the conductance. A tilted current plateau around G_0 was observed which can be assigned to the conductance quantum. The tilting of the current was caused by the interference of electrochemical current. The etching rate can be controlled by the potential: more positive potential will cause faster etching rate and more negative potential will generate slower etching rate. In this work, low etching rate was preferred in order to get a better control. The extent of the etching can be monitored by the electrochemical current and the etching process can be stopped when desired value is reached. The etching can be used with the electrodeposition and tuning the gap size in the electrolyte can be achieved [113]. In our work, the etching were usually stopped at very low conductance ($10^{-6}\,G_0$) to totally open the connection and then close the gap by deposition again. However, since the etching of atoms occurred at multiple sites, the morphology of the electrode surface after etching

process is difficult to control. A more advanced technique combining electrochemical and chemical etching was introduced in the work of Kervennic et al. [147]. By this method, the grains generated during the electrochemical etching were kept minimal. In this work, we did not continue to optimize the etching process.

The adsorption of molecules has an influence on the stability of the atomic point connection and the introduction of molecules will greatly increase the stability of the deposited atomic scale junctions. This is because the adsorption of molecules to the surface of gold atoms decreased the mobility of the gold atoms. However, the adsorbed molecules are difficult to remove after the deposition process and become a source of contaminants for the following measurements.

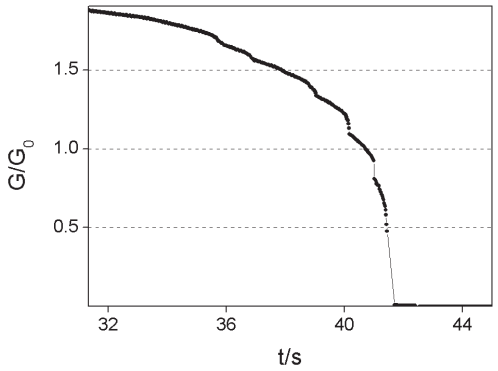

Figure 4.35.: Etching process: the atomic scale junction was broken since the atoms on the electrodes dissolve into solutions.

In summary, needle-like nanogaps were fabricated by electrochemical modification of the nanogap electrode template. The size of the nanogap can be adjusted to sub 1 nm with stability and reproducibility.

4.3. Benzenedithiol junction assembled on fixed nanogaps

In the previous chapter, nanogaps on chip were fabricated on chip and needle-like nanogap electrodes were obtained by electrochemical modification. In this chapter, electron transport through molecules was tested. Firstly, the simple organic molecule 1,4-benzenedithiol (BDT) was tested on the electrodeposited needle-like structures and the I-V curves of the Au/benzeneditiol/Au were measured.

1,4-Benzenedithiol(BDT) was chosen as the testing target since this molecule has been intensively studied by several groups. However, despite the simple atomic structure and intensive studies, there exists discrepancy about the conductance of BDT among experiments

as well as between theory and experiments. Both low conductance ($10^{-4}\,G_0$ [159]) and high conductance ($0.011\,G_0$ [34], $0.1\,G_0$ [160, 161]) were reported. This conductance diversity was generally explained by the different molecule/electrode contact configurations.

The assembly of Au/benzeneditiol/Au junctions was described in Sec. 3.3. The *I-V* curves were obtained in the range from -0.5 V to 0.5 V (Fig. 4.36a). Compared to the work of Dong et al., where mercaptopropionic acid (MPA) molecules were studied by only recording single *I-V* curve and the work of Hatanaka et al. [162], where Oligothiophene molecules were studied in a similar method, several *I-V* curves were continuously recorded in this work in order to observe the reproducibility of the results [163]. The *I-V* curves shared similar features and were nearly linear within the potential range, however, the slope of the *I-V* curve increased gradually during the consecutive potential sweeping and reached twice higher at the last cycle. This variation can be explained by the change of molecule configurations or by the change of the number of molecules involved in the charge transport. The conductance calculated from the *I-V* curve at the last cycle was around $1\,x\,10^{-4}\,G_0$.

After recording the *I-V* curves within -0.5 V–0.5 V, the *I-V* curves within -1 V–1 V were immediately recorded and displayed in Fig. 4.36b. It can be seen that the *I-V* curves became unstable at high potentials, which is commonly observed in the molecular junction measurements at high potentials. Even within the same sweeping cycle, the conductance abruptly changed around zero potential. From the *I-V* curve, the conductance can be estimated to $1\,x\,10^{-6}\,G_0$.

The discrepancy of conductance with different potential range can be explained by the configurations of the molecular junctions or it can not exclude that the molecular junction Au/BDT/Au was already broken. Usually, a molecule with conjugated molecules consisting of methylthioacetate termini and short alkoxy side chains like OPV molecules are very stable in the molecular junctions [164]. It is difficult for the BDT molecules to determine if the measurement is based on a single molecule or multiple molecules, or if the molecular junctions are broken. It is also difficult to determine the specific configurations between molecules and electrodes. Another possible reason for the changes in the *I-V* curves of BDT junctions is the evolution of the nanogap size after deposition. It is known that nanogaps generated by electromigration experience long-term evolution so that the nanogap size gets larger during this process [165]. The electrodeposited nanoelectrodes are composed of gold clusters and it is more mobile than the gold electrode fabricated by sputtering. So, it is reasonable to believe the electrodeposited nanoelectrodes are more easily to experience the structural evolution.

In the scope of this work, *I-V* curves with conductance as high as $0.1\,G_0$ were also observed. The discrepancy in the conductance obtained from the *I-V* curves reflects the

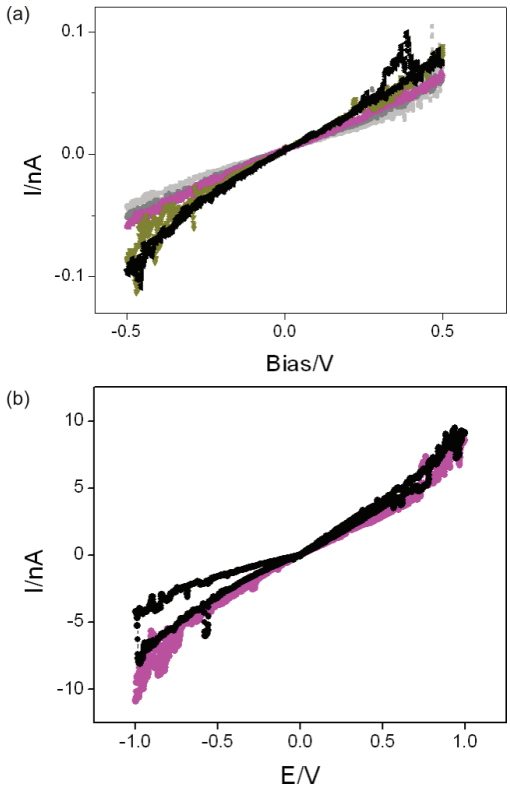

Figure 4.36.: Consecutive *I*-*V* curves of the Au/Benzenedithiol/Au junctions under potential (-0.5 V–0.5 V) (a) and (-1 V–1 V) (b).

fact that even though the nanogap electrode is very sharp and the gap size can be controlled with a resolution down to sub 1 nm, it is difficult to obtain single molecular junctions on such fixed nanogap. This disadvantage makes it difficult to use electrodeposited fixed-sized nanogap to investigate charge transport across molecules.

Thus, in the following part, electrodeposition was combined with mechanical controlled break junction techniques to generate nanogaps with adjustable sizes. The advantages of both techniques were combined that the morphology of the nanogap electrode can be modified and the size of nanogap can be adjustable. In this way, nanogaps were dynamically created and closed, and molecular junctions were formed and broken again.

4.4. Electrochemical mechanical controlled break junction (MCBJ)

In the last part, fabrication of nanogaps by electrodeposition was introduced and needle-like electrodes with radius of curvature smaller than 2 nm were obtained. The size of the nanogap can be tuned to sub 1 nm with very high accuracy. However, adjusting the nanogap size by deposition is in ex-situ manner, which means that the adjustment of gap size can be only achieved in the depositing solution, not in the electrolyte for measuring molecules.

Mechanical controlled break junction creates nanogaps by breaking a micro-scale wire and tuning the gap size by moving piezo rod. The adjustment of gap size in mechanical controlled break junctions does not need an electrolyte, thus it become a flexible method to generate nanogaps and has the ability to form metal/molecule/metal junctions dynamically and repeatedly. Using mechanical break junctions in electrochemical environment is a challenge since the electrochemical leakage current interferes with the tunneling current across molecular junctions.

In this work, several approaches were combined to realize a highly stable electrochemical break junction setup with low electrochemical leakage current. Firstly, during chip fabrication, a flexible insulating layer (PMMA) was used which adapts better to deformations than rigid SiO_x/SiN_x layers. Secondly, only a small access window was opened on the electrode, resulting small area of liquid/electrode interface and low level of electrochemical background currents. Thirdly, stable electrodeposited atomic point contacts were established and used as bridge in lieu of the conventional micro wires in the mechanical breaking setup. Very little mechanical deformation of the chip was needed to break the atomic point to separated electrodes. Thus, the probability of damaging the silicon chip and producing cracks in the insulating layer by mechanical strain was kept minimal. The parasitic electrochemical leakage current caused by the failure of chip structure was also controlled.

4.4.1. Electrochemical mechanical break junction setups

In this part, the basic configuration of an electrochemical mechanical break junction setup is described.

The electrochemical break junction setup is shown in Fig. 4.37. The setup is made of stainless steel and can be assembled and disassembled easily by screws. A nanoelectrode chip ($1\,\mathrm{x}\,1\,\mathrm{cm}^2$) is mounted on a stage and fastened by two stainless steel springs. On the chip, an O-ring was glued by PDMS. Appropriate electrolytes can be filled, forming a

micro electrochemical cell, in which the insulated nanogap electrodes are used as working electrodes and external one or two electrodes can be inserted into the electrolyte and used as reference electrode or counter electrode. According to the requirements, different electrode configurations can be established. In the Fig. 4.37, one of the facing nanogap electrodes is used as working electrode. Micro Ag/AgCl electrode and gold wire are used as reference electrode and counter electrode, respectively. In the inset images, the two facing nanogap electrodes are set to source and drain electrode, and an inserted Ag/AgCl electrode is set to gating electrode.

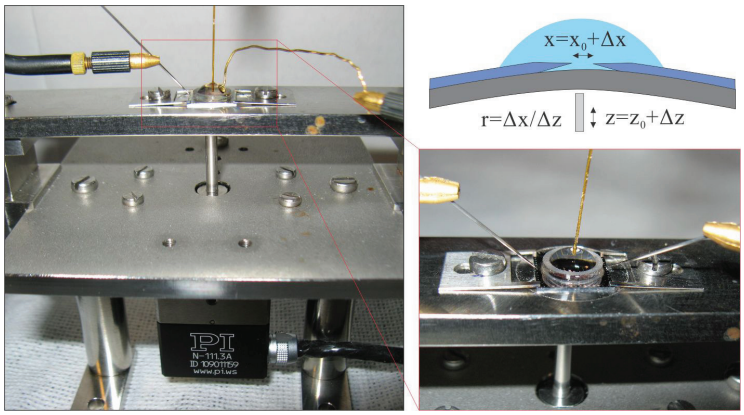

Figure 4.37.: Electrochemical break junction setup. The electrodes arrangement can be adjusted according to the requirements.

A piezo motor (PI GmbH, N-111.3A) was placed under the silicon chip, forming a three-point bending mechanism together with the fixing steel springs. When the piezo rod moves upwards, a displacement in the axis direction of Δz can be expected. Then the silicon chip bends with extension of the gap size Δx. The ratio $\Delta x/\Delta z$ is referred to as the reducing factor and can be calculated from the tunneling current curves (Sec. 4.4.3).

Tungsten needles were used to touch the contact pads on the chip edge, connecting the nanoelectrodes to the external measuring circuits. In this work, Keithley 4200-SCS semiconductor analyzer (Keithley Instruments Inc.) was used to control the electrochemical potential and monitor the transient current between the nanoelectrodes. A ground cable was connected to one of the screws on the setup.

4.4.2. In-situ deposition and breaking

The micro electrochemical cell mounted on the setup allows electrodeposition and the mechanical break junction has ability to adjust the gap size. Therefore, the deposition and breaking process can be performed in-situ.

The nanoelectrode chip was fabricated by electron beam lithography and the surface of the chip was covered by three layers of PMMA (200k/600k/200k) to insulate the gold nanoelectrodes (Sec. 4.1.2) [1]. The chips had a thickness of 230 µm. The silicon chips should not be too thick since thick silicon chip should not stand too much mechanical deformation. The chips cannot be too thin since the handle of thin silicon chip is very difficult, especially in the spin coating process. An access window was opened right over the electrode tips (Fig. 4.38a). The initial gap between the facing nanoelectrodes was set to 150 nm (Fig. 4.38b). This initial gap size was a compromise between effort of fabrication and the deposition time. More importantly, a space between the nanogap electrodes was needed to allow the growth of the needle-like structures. The relatively large gap of this template structure was reduced from 150 nm to atomic point contact by gold electrodeposition (Fig. 4.38c). Four examples of such electrodeposited nanobridges are displayed as insets. Such point connections were subsequently used as nanobridges for the following breaking process in the mechanical break junction setup.

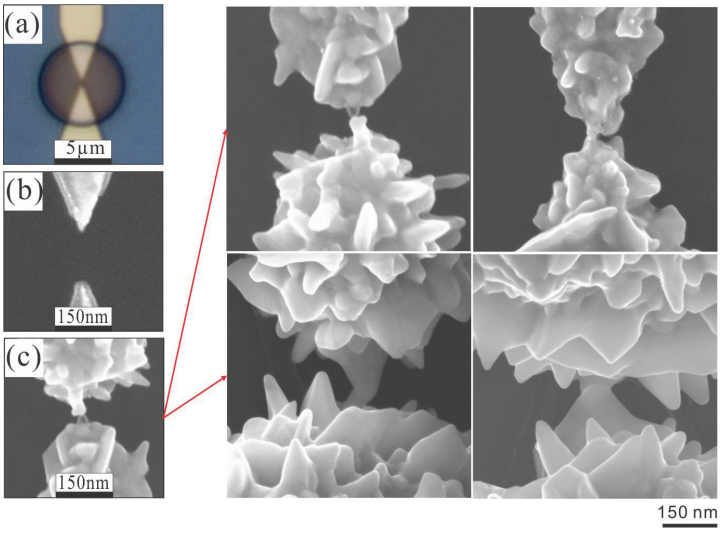

Figure 4.38.: Narrowing nanogap to atomic scale junctions by electrodeposition. Four deposited nanojunctions are displayed as examples.

The electrodeposition was performed on chip. A three-electrode configuration was employed. Two nanoelectrodes were set as source and drain electrode. A micro-scale Ag/AgCl electrode inserted in the electrolyte was set as gate electrode. The deposition was performed until an Au bridge was established and the process was controlled by monitoring the source/drain current. A main challenge of this routine lies in the precise control of electrodeposition process. The fabrication of nanogaps by the electrodeposition method had been carefully studied and the deposited nanogaps were found stable when the overpotential

was set as small as possible during the electrodeposition (Sec. 4.2.2). Here, electrodeposition was performed at 0.6 V (depositing current starts at 0.7 V) with respect to Ag/AgCl reference electrode [1], and protruding extensions were generated on the surface with a tip curvature of 10 nm (Fig. 4.38 insets). Compared to the work of Tian et al. [132], where the deposited electrodes have a radius of curvature of hundreds of nanometer, this modified electrodes are more suitable to be used for contacting molecules.

The conductance changes during the in-situ electrodeposition process are described in Fig. 4.39. The nanogap electrodes were immersed in electrolyte during the whole process to protect the systems from air-born contaminates. Different electrolytes were used in the electrodeposition phase (Chloroauric solution) and in the mechanical breaking process (dilute sulphuric acid). Here, gold atoms were deposited on the nanogap electrodes and the electrodeposition was stopped when point contact was formed. The deposition includes mainly three regimes: the ion conduction regime, the tunneling regime and the quantum conductance regime. A similar process was also observed in the work of Dong et al. [163]. An exponential increase of conductance between the source and drain electrode was observed (Fig. 4.38, I). After the electrodeposition was stopped, the conductance jumped from 1 G_0 to approximately 4 G_0 then returned to a value between 2 and 3 G_0. This conductance fluctuation occurred during the potential change from deposition range to non-deposition range. This fluctuation period lasted about 2 minutes, then the conductance was settled down and has stabilized at this conductance for more than 5 minutes. During this period, several operations can be performed in-situ. Here, the chip was rinsed by water and the depositing solution was replaced by diluted sulphuric acid. The conductance did not change much when the buffer was replaced (approximately at 400 s). This property is in particular of importance for in-situ measurements of single (bio-) molecules in buffer solution of different compositions. The atomic point contact was subsequently broken by the mechanical bending of the chip and exponential decay of conductance was obtained (Fig. 4.39, IV). Only slight mechanical bending (10–30 µm, vertically) of silicon chip was required to break the junction.

If the electrodeposition continued after the atomic contacts were formed, massive bridge (over 10 nm in width) would be formed, which could also be used as bridge for mechanical breaking. However, the massive bridges were very difficult to break and most of the chips were ruined during the breaking process, due to the brittleness of silicon. Using the deposited point contact as bridge, the yield was significantly increased and 90% of the chips remained intact after the breaking process. A maximum vertical displacement of 400 µm can be applied on the chip before the chip is destroyed, which allows generating tunable nanogaps from 0 to 4 nm separation, calculated from the reducing factor of this setup (10^{-5}, calculation procedures see Sec. 4.4.3)

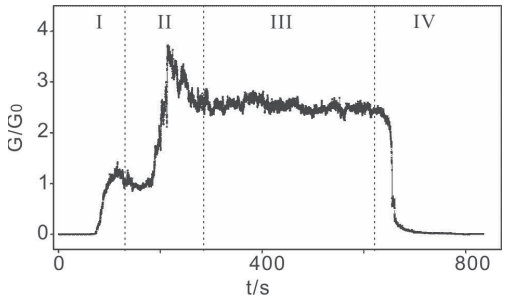

Figure 4.39.: In-situ deposition and breaking. (I) electrodeposition from a nanogap to point contact. (II) Conductance fluctuation after deposition is stopped. (III) Stable gold point contact over 5 minutes. (IV) Breaking gold contact into nanogaps by mechanical force

4.4.3. Characterization of the electrochemical break junction setup

As discussed in the beginning of this chapter, the purpose of combing the in-situ electrodeposition and mechanical break junction techniques is to control the electrochemical leakage current and increase the usability of the setup. In this part, the characterization of the setup is described which showed that the above purpose can be achieved.

Directly tunneling and calibration

After the point contacts were formed by deposition, the junctions can be broken and closed mechanically as in a conventional mechanical break junction setup. Three representative conductance traces recorded during the breaking process are displayed in Fig. 4.40a. Quantized conductance at $1\,G_0$ was observed in the conductance traces which indicated the functionality of the setup. The typical exponential decay of conductance demonstrated the pure tunneling response between the two electrodes and a reducing factor of $1.7\,\mathrm{x}\,10^{-5}$ can be calculated from the tunneling traces. To calculate the reducing factor, the change of gap size Δx can be estimated by the tunneling currents according to the Eq. (2.27). For instance, the conductance traces in Fig. 4.40a drops suddenly from $1\,G_0$ to $10^{-4}\,G_0$ and then decreases linearly to $10^{-6}\,G_0$. The linear decrease of conductance from $10^{-4}\,G_0$ to $10^{-6}\,G_0$ versus the gap distance in the log scale fits perfectly to the tunneling equation (2.27). The change of the gap size was then estimated according to the equation. The displacement of the piezo rod was recorded from the control software of the piezo motor (PI GmbH, N-111.3A). Thus, the reducing factor can be calculated.

A maximum vertical displacement of 400 µm was applied on the chip before the chip was destroyed, which allowed generating tunable nanogaps from 0 to 4 nm separation, calculated from the reducing factor of this setup. Here, the conductance histogram was calculated

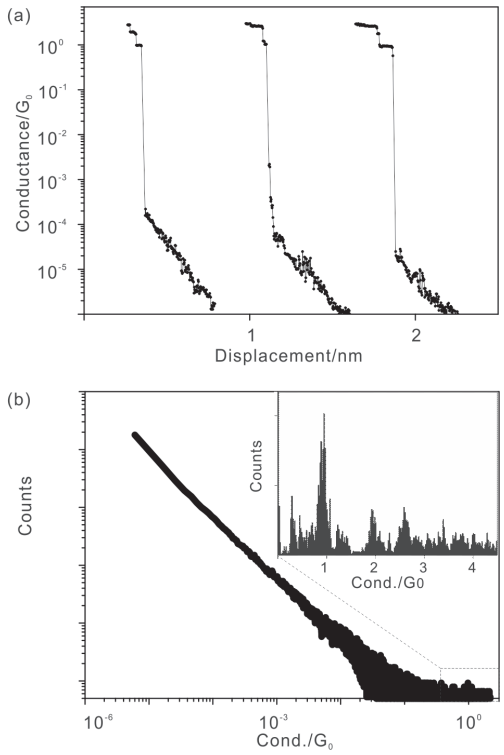

Figure 4.40.: Representative conductance traces recorded during junction breaking process and the corresponding histogram constructed from more than 200 curves.

over 200 breaking curves. A bin size of $5 \times 10^{-6}\,G_0$ was used for the histogram construction. The linear histogram in log-log scale confirmed the pure tunneling response between the bare electrodes (Fig. 4.40b). The histogram is represented in log scale since data points over large range can be displayed (from 10^{-6} to $1\,G_0$). However, the log scale axis is not appropriate to reveal the features in a relatively narrow range. Thus, a histogram around $1\,G_0$ is displayed in linear axis as shown in the Fig. 4.40 inset, in which peaks at multiples of $1\,G_0$ have been revealed.

I-V curves of nanogaps with different gap sizes were studied in aqueous solution (Fig. 4.41). The potential of one electrode was set to 0 V and the potential of the other electrode was swept from 0 V to 0.7 V, with respect to the Ag/AgCl electrode. The potential sweeping range needs to be carefully chosen, because the accessible potential range is restricted by the potential range where the gold electrode is ideally polarizable. More positive potential would cause gold oxidation and more negative potential could induce hydrogen evolution reaction. The potential was cycled from 0 V to 0.7 V instead of from -0.35 V to 0.35 V, in order to provide the largest potential range and test the stability of the nanogap under

relatively high potential. In Fig. 4.41, each curve includes 3 consecutive recordings and no significant current increase with the number of cycles is observed, which indicates that the nanogaps generated in aqueous solution are stable. The gap sizes were estimated at 6 Å and 9 Å by Simmons fitting.

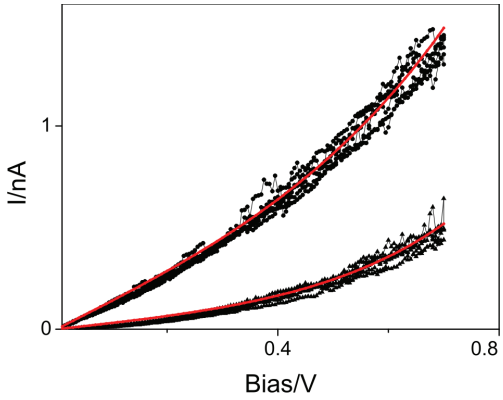

Figure 4.41.: I-V curves of nanogaps at different gap sizes recorded in aqueous solution (black). Simmons fitting (red) was performed on the bases of I-V curves.

The I-V curves within the range from 0 V to 0.7 V fit well with the Simmons equation, indicating the charge transport mechanism is direct tunneling. The charge transport mechanism can be also revealed by the $\ln(I/V^2)$ vs. $1/V$ plot (Fowler Nordheim plot) which can be obtained from I-V curves. A characteristic linear decrease of $\ln(I/V^2)$ with respect to $1/V$ will be observed if the charge transports through field emission (see Eq. (2.29)). Here, the Fowler Nordheim plot (Fig. 4.42) did not show any feature belonging to field emission transport, which indicates the charge transport through the nanogap was simple tunneling.

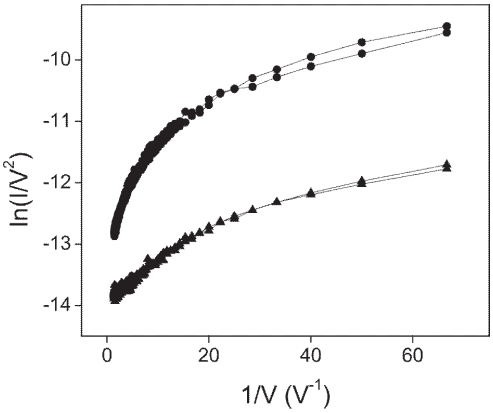

Figure 4.42.: Plots that indicate the electron transport through simple tunneling.

Electrochemical leakage current during breaking process

To evaluate the electrochemical leakage current of the electrochemical break junction setup, a series of cyclic voltammograms were recorded in-situ at different gap sizes during the mechanical breaking process. The electrodeposited nanobridge was set as working electrode. Micro Ag/AgCl electrode and Au wire immersed in dilute sulphuric acid were used as reference and counter electrode. Here, two CVs were recorded at the atomic point contact state and 2 nm gap state (Fig. 4.43). All potentials were denoted with respect to Ag/AgCl reference electrode. The electrochemical current was about 20 pA measured at potentials where gold is ideal polarizable (below 0.9 V). This value is much lower than the electrochemical leakage current of 0.5 µA obtained by Kiguchi et al. [27]. At higher potentials gold oxidation/reduction occurred. Even under these aggressive conditions, the change of reduction peak current between first CV curve (black line) and the second CV curve (red line) was within 1%, which indicated that the insulating layer remained nearly intact and the cracks related to electrochemical leakage current had no significant influence on the system. The electrode surface calculated from the reduction peak was around 4 μm^2, which was very close to the designed value (2.9 μm^2, Sec. 4.1.4). A similar work about combining electrodepostion and mechanical break junction techniques were described by Tian et al. [132]. However, considering the brittle insulating materials SiN_x used in their work and the lack of a characterization of the electrochemical leakage current during the closing and closing process, our setup would be more suitable to used in the real measuring of molecules.

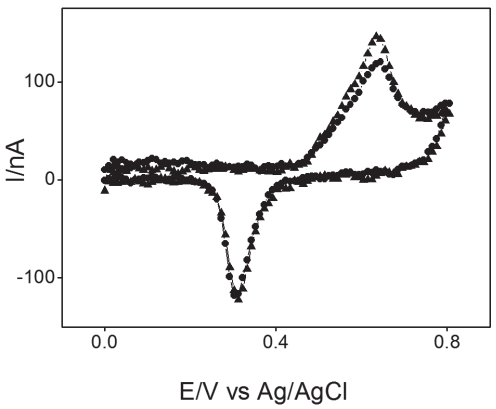

Figure 4.43.: Cyclic voltammograms of the electrodes recorded at different gap sizes (100 mV/s).

4.5. Electrostatically linked Ferrocene junctions assembled on MCBJ

In the Sec. 4.2 and Sec. 4.3, nanogaps on chip were fabricated on chip and needle-like nanogap electrodes was obtained by electrochemical modification. By measuring the Au/benzeneditiol/Au junctions, it was demonstrated that the fixed nanogaps were not suitable to be used as a tool for investigating charge transport across single molecules. Then, an electrochemical break junction setup was fabricated which was based on the electrodeposited nanobridges and featured low electrochemical leakage current. In this chapter, electron transport through molecules was tested on such electrochemical electrochemical break junction setup. Molecular chain based on intermolecular electrostatic coupling was assembled on the electrochemical break junction setup and the conductance of molecular junctions at single molecule level was successfully determined.

The electron transport across electrostatic interface was studied by measuring conductance of molecular junctions based on electrostatic coupling. First of all, the importance of intermolecular electrostatic interface in the charge transport chain was introduced. Then, the method of assembling molecular junctions based on intermolecular electrostatic coupling was described. The method was first verified on 2 dimensional gold surfaces by running cyclic voltammetry. Then molecular junctions were assembled on the electrochemical break junctions and the conductance of single molecular junctions was determined.

Intermolecular electrostatic coupling

Here, the principle of intermolecular electrostatic coupling was introduced. The coupling was in an aqueous environment and based on the protonation and deprotonation of organic molecules. Simple organic molecules cysteamine and ferrocene were used since their structures are much simpler than the complex structures of proteins and the covalently counterpart cysteamine-ferrocene-cysteamine has been studied [166].

The intermolecular electron transport was investigated across a molecular junction containing two electrostatic interfaces. The electrostatically linked conjugates were assembled by entrapping negatively charged redox active 1,1-ferrocene dicarboxylic acid (FDA) between two positively charged cysteamine modified gold electrodes in aqueous solution (Fig. 4.44a). For assembling ferrocene junctions, the pH of the buffer solution has to be carefully adjusted with respect to the pK_a of the involved functional groups. At the employed pH, the carboxylic groups of 1,1-ferrocene dicarboxylic acid have to be deprotonated in order to let the molecule carry negative charges. At the same time, the amine group of the cysteamines has to be protonated in order to accumulate positive charges on the

electrodes (Fig. 4.44b).

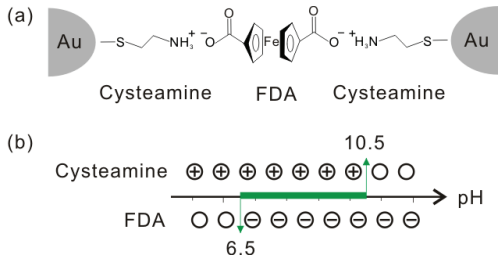

Figure 4.44.: (a) Assembling molecular junctions based on intramolecular electrostatic interactions. (b) Illustration of the appropriate pH range (green) where 1,1-ferrocene dicarboxylic acid is deprotonated and cysteamine is protonated

Intermolecular electrostatic coupling on surface

To evaluate the appropriated pH window, cyclic voltammetry of cysteamine modified gold electrode with/without electrostatically adsorbed 1,1-ferrocene dicarboxylic acid molecules were examined at different pHs. Considering the pK_a of the first and second carboxylic group of 1,1-ferrocene dicarboxylic acid (6.5 and 7.6) [167] and the pK_a of the amine group of cysteamine (10.5) [65], buffers with pH values of 4.0, 6.0, 8.0, and 10.0 were used to cover all protonation/deprotonation statuses of FDA/cysteamine molecules. The experimental details were described in Sec. 3.3.

The potential ranges of the cyclic voltammograms were set according to the applied pH to avoid the interference of gold oxidation at anodic potentials, since the redox potential shifted with the pH value as seen in Fig. 4.45.

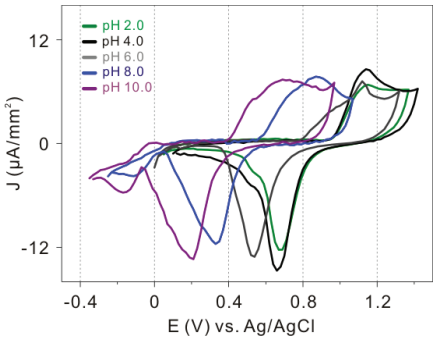

Figure 4.45.: CVs of bare gold electrodes recorded in Britton-Robinson buffer at pH values from 2.0 to 10.0 to evaluate the pH induced potential shift.

From the Fig. 4.45, it becomes obvious that the gold reduction peaks shifted negatively from 0.7 V to 0.2 V when the pH was increased from 2.0 to 10.0. The reduction peak

position vs. pH value plot (Fig. 4.46) showed nearly linear dependence of the shifted value on the pH values. From the linear fitting, it can be calculated that the reduction position decreased by 62 mV when the pH value increased by 1, which agrees with the Nernst equation (2.39).

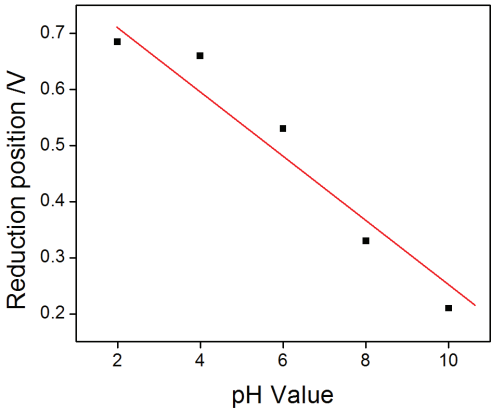

Figure 4.46.: The relationship between reduction peak position and the pH values.

For different pH values, different potential ranges were chosen for the cyclic voltammetry. For example, at pH 4.0, a relatively large potential range (0.1–0.9 V) can be used, however, at pH 10.0, a narrower potential range (0.1–0.55 V) was used, since at 0.6 V, gold oxidation would occur.

Before performing cyclic voltammetry of electrostatically linked monolayer, The background current was studied by running cyclic voltammetry of gold electrodes on chip and cysteamine modified electrodes at pH 4.0 (Fig. 4.47). The potential was chosen in the range where no redox reaction occurs. It can be seen that the main background current is the capacitance current at the level of 0.4–0.8 $\mu A/mm^2$. The capacitance current is caused by the relatively large conducting lead and reducing the capacitance current needs further optimization of the chip structures. For example, increase the thickness of the insulating layers, or decrease the width of the conducting leads may help reduce the capacitance current from the insulated leads.

In the following, the cyclic voltammetry of electrostatically-linked molecules are investigated.

Firstly, the cyclic voltammetry was recorded with the presence of 1,1-ferrocene dicarboxylic acid molecule as shown in (Fig. 4.48a), where the electrochemical current is diffusion controlled. At pH 4.0, there are no redox peaks in the CV curve can be observed, indicating there is almost no interaction between 1,1-ferrocene dicarboxylic acid and the cysteamine monolayer at this pH. With pH 6.0, 8.0 and 10.0, redox peaks can be observed

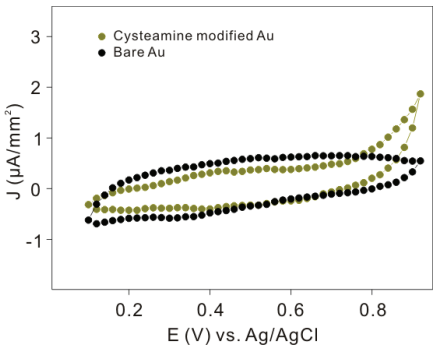

Figure 4.47.: CVs of bare gold electrodes and cysteamine modified electrodes.

that causes the diffusion of 1,1-ferrocene dicarboxylic acid molecules to the electrode surface and the following charge transfer process at the solid/liquid interface. The peak value of the CV curves increases with respect to the pH, and the peak value at pH 10.0 is about twice high as the peak value at pH 8.0, which can be explained by the increased net charge of 1,1-ferrocene dicarboxylic acid molecules from HOOC-Fe-COOH to HOOC-Fe-COO^- and $^-$OOC-Fe-COO^- upon two step deprotonation process.

Secondly, the cyclic voltammetry was recorded without the presence of 1,1-ferrocene dicarboxylic acid molecule by rinsing the electrode after ferrocene was immobilized. The CVs (Fig. 4.48b) demonstrate different features compared with the CVs of the covalently linked system. Firstly, reversible redox peaks of oxidation and reduction of 1,1-ferrocene dicarboxylic acid molecules can be only observed in the CV curve at pH 8.0, but not at pH 4.0, 6.0, or 10.0. The pH dependence of the surface confined redox responses is consistent with the assumption that the 1,1-ferrocene dicarboxylic acid molecule can be adsorbed on the cysteamine monolayer only within a certain pH window.

At pH 8.0, the oxidation peak was found at 0.46 V and the reduction peak at 0.4 V with a full width at half-maximum of 90 mV, which suggests a single electron redox process [168]. The peak to peak potential separation is 60 mV at the sweeping rate of 100 mV/s, which is larger than the nearly zero potential separation observed in the covalently linked counterpart as reported earlier [166]. This potential separation indicates that the electron transfer rate through the electrostatically linked system is slower than that of the covalently bond systems. The capacitance current of 0.4-0.8 $\mu A/mm^2$ is composed of the capacitance current from the molecular monolayer and the PMMA insulated lead electrodes.

On the other hand, the CVs of the electrostatically linked system shared some similarities with its covalently linked counterpart. The total charge of the oxidation peak is estimated to be 30 $\mu C/cm^2$ and the corresponding coverage of adsorbed molecules is 1.9×10^{14} molecules/cm^2, which is very close to those of the covalently linked ferrocene

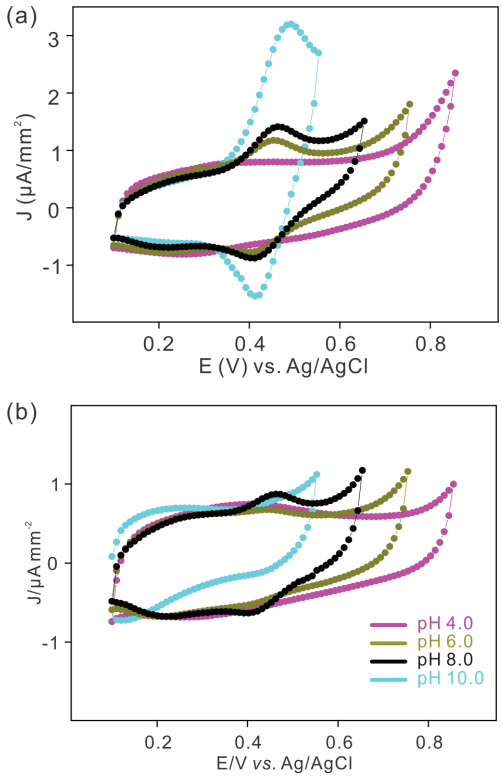

Figure 4.48.: Cyclic voltammograms of cysteamine modified electrode with (a) or without (b) the presence of ferrocene molecules in Britton-Robinson buffer ($100\,\mathrm{mV\,s^{-1}}$).

molecules ($2.2\,\mathrm{x}\,10^{14}$ molecules/cm^2) [166].

In situ break junction experiments were performed for bare metal electrodes, after adsorption of cysteamines on their surface, and after addition of ferrocene molecules at different pH values. Representative conductance traces under different conditions are displayed in Fig. 4.49.

In all curves, quantized conductance at $1\,G_0$ was observed, indicating that the mechanical break junction setup was well controlled. Cysteamine modified gold junctions in pure buffer were used as reference (1_{st} line, orange) since the molecule binds tightly only to one of the two nanoelectrodes, which results in an exponential decay of conductance. For cysteamine modified electrodes in 1,1-ferrocene dicarboxylic acid containing buffer at pHs of 4.0 and 10.0, similar tunneling responses were observed (2_{nd} line, magenta; 4_{nd} line, cyan, respectively). However, for cysteamine modified electrodes in 1,1-ferrocene dicarboxylic acid containing buffer at pH 8.0, conductance plateaus at low conductance (around $10^{-4}\,G_0$) were revealed, which can be assigned to the transport of electrons across 1,1-

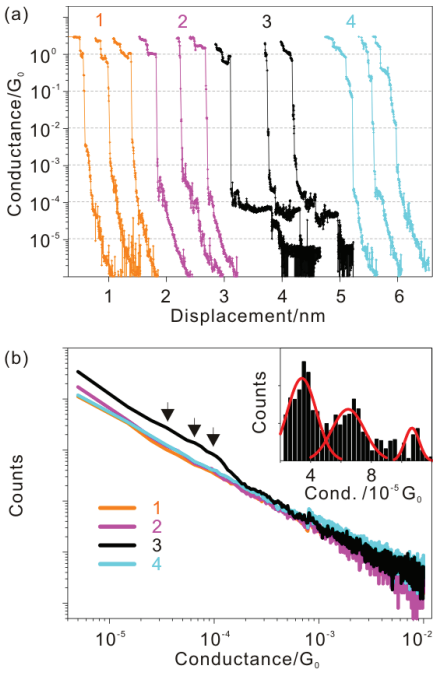

Figure 4.49.: (a) Conductance traces recorded during breaking cysteamine modified gold junctions in pure buffer (1st) and in buffers with the presence of FDA at pH 4.0 (2nd), 8.0 (3rd), and 10.0 (4th), respectively. (b) The corresponding histogram constructed from over 200 curves and the Gaussian fitting of the peaks for pH 8.0 (inset).

ferrocene dicarboxylic acid molecules entrapped between a pair of cysteamine modified electrode during the breaking process. This pH dependent appearance of conductance plateaus coincides with the observations of the CVs that the 1,1-ferrocene dicarboxylic acid and cysteamine molecules could be electrostatically coupled at pH 8.0. Several hundred conductance traces were collected for each experimental condition at different time on different chips. More than 200 consecutive curves were used to construct a conductance histograms for each situation without curve selection (Fig. 4.49b). For 1,1-ferrocene dicarboxylic acid free experiment as well as 1,1-ferrocene dicarboxylic acid containing solution at pH 4.0 and 10.0, similar linear histogram in log-log scale were obtained (Fig. 4.49b, 1_{st} line, 2_{nd} line, 4_{th} line, respectively), which confirmed a pure tunneling response between the electrodes. It can be assumed that no molecule chain was formed across the gold nanojunction. For the cysteamine modified electrodes in 1,1-ferrocene dicarboxylic acid solution at pH 8.0, 60% of all collected conductance traces displayed conductance plateaus and two clear peaks deviating from the background were observed in the histogram (Fig. 4.49b, 3_{rd} line, black). The peak positions were retrieved by subtracting the background histogram (1_{st}

line, recorded from a cysteamine modified gold junction without 1,1-ferrocene dicarboxylic acid molecules) from the histogram at pH 8.0 (3_{rd} line) and Gaussian fitting (Fig. 4.49b inset). The peak with the lowest conductance was observed at $0.34\,\mathrm{x}\,10^{-4}\,\mathrm{G_0}$, which can be assigned to the conductance of a single molecular junction. The second peak appeared at $0.65\,\mathrm{x}\,10^{-4}\,\mathrm{G_0}$, which is twice as the basic value and can be assigned to two parallel aligned single molecular junctions. A third peak at $1.07\,\mathrm{x}\,10^{-4}\,\mathrm{G_0}$ was observed but not sufficiently supported by the recorded amount of data, which can be explained by the low probability and stability of formation of three parallel aligned single molecular junctions [166].

The conductance of electrostatically linked single molecular junction is one order of magnitude lower than the covalently linked ferrocene molecules ($3\,\mathrm{x}\,10^{-4}\,\mathrm{G_0}$), which indicates that the electrostatic coupling is strong enough to form an electron transport pathway, but the electron transfer rate across electrostatic interfaces is lower than across the covalent bond. A similar conductance difference between inter- and intra-molecular electron transport pathway was observed by Wu et al. for aromatic molecules, where the conductance of aromatic molecule systems linked by π-π coupling is about one order of magnitude smaller than the conductance across a single covalently linked molecule [41]. One possible reason for the lower electron transfer rate might be the localized character of the molecular orbitals at the electrostatic interface, which presumably lead to an additional barrier within the electron transport pathway compared with the delocalized overlapping electron states in intra-molecular electron transfer pathways. In addition, it cannot be excluded that the low electron transfer rate across electrostatically linked molecular junctions is related to an increase of the reorganization energy during the electron transfer process according to the Marcus theory.

As introduced at the beginning of the chapter, the intermolecular electrostatic interfaces were very important to the electron transport reactions between cytochrome *c* and succinate-cytochrome *c* reductase or cytochrome oxidase. The spectrophotometric techniques revealed that the kinetic parameter for the electron transfer reaction decreased rapidly as the ionic strength was increased [169]. Our experiments showed that the conductance across the electrostatic interface was lower than the covalent coupling, however, the quantitative analysis of intermolecular charge transfer rates have not been studied, which need differential capacitance vs. potential and current density vs. potential measurements [170]. Such measurements can be performed in the future research.

Conductance histogram calculation

Each histogram in Fig. 4.49b was constructed from 200 conductance curves. The conductance trace was actually a data sheet with two columns of data, the first column is the conductance and the second is the displacements between the two electrodes. The con-

ductance data from 200 conductance traces were extracted and combined to one data set and the histogram of the combined dataset was determined. A bin size of $5 \times 10^{-6}\,G_0$ was used to calculate the histograms. The histogram analysis generated a data set with two columns: probability and the conductance values. This histogram was represented in log scale to obtain an overview of the conductance distribution over a large conduction range of five orders of magnitude. Moreover, in log scale, the conductance histogram of pure tunneling appears as a straight line, which makes it is easier to distinguish the histograms with peaks from histograms of pure tunneling.

To calculate the position of the peaks observed in the conductance histogram, the histogram with peaks was firstly subtracted by the histogram of pure tunneling to eliminate the background effect; then, the peaks of the subtracted histogram was positioned by Gaussian fitting, according to the work of Schönenberger. The configurations of the molecular junctions are similar: same electrodes, same adsorbed molecules and same buffer, except that the pH of buffer is different. Therefore it is reasonable to assume the parameters in the tunneling equations do not vary a lot and the tunneling current can be subtracted. This assumption was also confirmed by the same slope of the histograms curves shown in Fig. 4.49b.

Summary

In summary, the intermolecular electron transport across electrostatic interfaces was investigated by cyclic voltammetry and in-situ break junction experiments on the molecular level. Both techniques revealed that the 1,1-ferrocene dicarboxylic acid molecules can be electrostatically bound to cysteamine modified electrodes only within a small pH range, where the two molecules are oppositely charged. However, within this pH range, it was possible to bridge two opposing nanoelectrodes by electrostatically linked cysteamine/ferrocene/cysteamine junctions in aqueous solution and to determine corresponding conductance histograms. The observed single molecule conductance of the electrostatically linked junction was one order of magnitude smaller than the conductance of the covalently linked cysteamine-ferrocene-cysteamine, which indicates that the intermolecular electron transport through electrostatic interfaces has lower efficiency compared to intramolecular electron transport. This finding will be of relevance for the understanding of electron transport mechanisms in biological systems as well for the designing of biosensors employing electrostatically linked biomolecules.

5. Conclusions and Outlook

In this work, nanogap electrode arrays were successfully fabricated on silicon chips. Triangular nanoelectrodes were fabricated by electron beam lithography and were more suitable to be used as electrodes for contacting molecules than rectangular nanoelectrodes. The nanogap size between the facing nanogap electrodes can be adjusted by the exposure doses down to sub 5 nm; however, due to the large radius of curvature of nanoelectrode tip, they were not appropriate to form single molecular junctions. Other techniques like focused ion beam etching were also employed to create nanogaps, but the geometry of the etched electrode was almost parallel and thus not suitable for forming single molecular junctions. The results showed that further electrochemical modification were necessary to obtain sharp nanoelectrodes with small radius of curvature.

The nanoelectrodes insulated by PMMA layers were modified by electrochemical methods. The mechanisms of potentiostatic electrodeposition in traditional gold (III) electrolyte in nanoscale were investigated by current transient analysis. It was found that the nucleation process was diffusion controlled progressive nucleation but the crystal growth was potential controlled. The SEM examination found that the potential controlled crystal growth generated materials of different morphology. Either needle-like nanogaps at low overpotentials or smooth nanogaps at high overpotentials were obtained. The needle-like electrodes were still formed on one electrode deposition, which indicated that the needle-like structure was not related to the high electric field between the nanogap electrodes. We found that the sharp nanogaps had better stability and the quantized conductance was easier to achieve for sharp nanogaps. In conclusion, the electrochemical modified needle-like nanogaps with radius of curvature as small as 2 nm were more suitable to contact single molecules.

The measurements of molecular transport were first carried out on the electrodeposited nanogaps. The model molecule 1,4-benzenedithiol was used as the testing molecules. *I-V* curves of Au/Benzenedithiol/Au junctions exhibited discrepancy between different measurements and even in the same potential sweeping cycle, which can be explained the complicated molecule/electrode configurations. This discrepancy indicates it is generally difficult to realize single molecular junctions on the fixed size nanogaps.

An electrochemical break junction setup with low and constant electrochemical leakage current was fabricated to realize adjustable nanogaps. Electrodeposited nano-junctions were used as the bases of the mechanical break junction, which was much easier to break than traditional micro-wires fabricated by optical/electron lithography and the rates of successfully breaking without ruining the chips were greatly increased. I-V curves and cyclic voltammetry characterization showed that the chip structure could be kept intact during the breaking process and the electrochemical leakage current caused by structural failure of chips was kept minimal. This electrochemical break junction setup would be useful in investigating transport properties of nanoscale objects where aqueous environment is required.

Then the measurements of molecular transport were performed on the electrochemical break junction setup. The measurements were successful and proved the ability of the electrochemical break junction to measure transport properties of molecules in aqueous solutions. Two kinds of molecules, cysteamine and ferrocene, were used and a molecular chain based on intermolecular electrostatic coupling was established. The intermolecular electron transport across electrostatic interface was investigated by cyclic voltammetry and in situ break junction experiments on molecular level. Both techniques revealed that the ferrocene molecules can be electrostatically bound to cysteamine modified electrodes only within a small pH range, where the two molecules are oppositely charged. However, within this pH range, it was possible to bridge two opposing nanoelectrodes by electrostatically linked cysteamine(+)/(-)ferrocene(-)/(+)cysteamine junctions in aqueous solution and to determine corresponding conductance histograms. The observed single molecule conductance of the electrostatically linked junction was one order of magnitude smaller than the conductance of the covalently linked cysteamine-ferrocene-cysteamine molecules, which indicates that the intermolecular electron transport through electrostatic interface has lower efficiency compared to intramolecular electron transport. This finding will be of relevance for the understanding of electron transport mechanisms and pathways in biological systems as well for the designing of biosensors employing electrostatically linked biomolecules.

Further works can be anticipated on the base of current results. For example, for redox molecules, the transport properties change with the gating potential. Thus, a third electrochemical potential can be applied when measuring the conductance of electrostatically linked ferrocene junctions, forming a prototype electrochemical transistor. Another interesting topic is to combine the surface enhanced Raman spectroscopy in the molecular charge transport measurement. Raman spectroscopy has the ability to detect the molecular configurations, which are very important factors determining the molecular transport properties. In addition, investigating some physical or chemical phenomena such as surface plasma, magnetic in the single molecular level is also a fascinating project. In the writer's

understanding, another important topic is to investigate the charge transport between the proteins, especially between the proteins involved in an electron transfer chain. This topic has been conventionally studied by biophysical methods such as spectroscopic techniques, but it is generally difficult to investigate the transport between proteins at single molecule level because of the lack of appropriate tools. The writer believes that the electrochemical break junctions would become a useful tool in investigating the electron transport across proteins.

A. Materials and Devices

This part listed the materials and devices used in this work.

A.1. Optical lithography

The materials and devices for optical lithography are listed below:

- Clean room: class 100 clean room with permanent control of particle number, temperature and humidity.
- Wafer: phosphor doped N-type silicon wafers from Wacker Chemie AG. The wafer has resistance of 70–130 Ohm/sq, thickness of 280 µm and diameter of 2 in.
- Piranha solution: three parts of H_2SO_4 and one part of H_2O_2. The mixed solution is heated up to 60 °C.
- Wafer Cleaner: SSEC 3300ML Wafer Cleaner.
- Plasma oven: TePla microwave plasma system 300M.
- Oxidation oven: Tempress oxidation oven.
- Mask: glass mask fabricated by electron beam writer.
- Mask cleaner: APT 915 mask cleaning station.
- AZ-5214: negative photoresist, 28%, ALLRESIST GmbH.
- Mask aligner: Karl Suss MA-6 mask aligner, The UV source is a mercury lamp and the g-line (435 nm), h-line (405 nm) or i-line (365 nm) can be chosen.
- Developer: AZ 351B (ALLRESIST GmbH), 1:4 diluted.
- Nitrogen gas: 99.8% nitrogen gas.
- Scanning Electron Microscope: Zeiss Gemini 1550.
- Physical Vapor Deposition: Pfeiffer PLS 500.
- Profile check: Dektak 3030 (Sloan/Veeco).

A.2. Electron beam lithography

- Electron beam resist: PMMA 600k (ALLRESIST AR-P).
- Electron beam writer: Leica Vistec EBPG-5000 plus Lithography System.
- Developer: AR 600-55 (ALLRESIST GmbH).
- Megasonic device: 2 MHz transducer system (Sonosys).

A.3. Focused Ion Beam (FIB)

- Zeiss Auriga TM Crossbeam, dual beam system with Gemini electron column with Schottky field emitter.
- Orsay Physics Cobra FIB ion column with variable acceleration voltage from 1 kV to 30 kV.
- Changeable ion source (Ga-source, AuSi and other ion sources).

A.4. Electrode Insulation

- PECVD: Oxford Plasma Technology.
- Reactive ion etching: Oxford RIE.

A.5. Chip encapsulation

- Flip machine: Fineplacer@ Lambda, FINETECH GmbH, Germany.
- Probe station: PM5 probe station, SUSS Microtec, Garching.
- External measuring circuits: 4200 Semiconductor Analyzer, Keithley Instruments; Cleveland, OH, USA.

A.6. Electrochemical experiments

Electrochemical investigation on the macroelectrodes:

- Electrochemical cell: conventional macroscopic electrochemical cell with three-electrode configuration (Fig. A.1).

- Working electrode: gold single crystal or gold wire (1 mm diameter) with a melting tip.
- Counter electrode: Gold or Platinum wire.
- The reference electrode: saturated calomel electrode.
- Potentiostat: Autolab potentiostat PGSTAT 302 (Eco Chemie B.V., Utrecht, NL) with an additional module (BIPOT) which allows using a second working electrode, forming a four-electrode configuration.
- Deposition solution: 0.01 mM Chloroauric acid (Aldrich, 99.999%) with 0.5 M Lithium chloride (Aldrich).
- Faraday cage: home-made Faraday cage to shield the electrochemical cell from external electromagnetic wave.

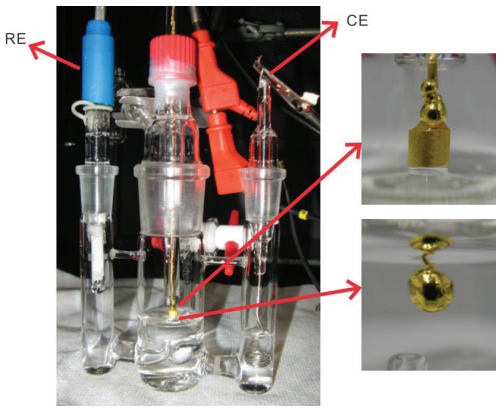

Figure A.1.: Conventional electrochemical cell with three-electrode configuration. The working electrode can be either gold single crystal (right up) or gold wires with melting tip (right down). The counter electrode is a platinum wire and the reference electrode is a saturated calomel electrode.

Electrochemical investigation on the nanoelectrodes:

- Two nanoelectrodes fabricated by electron beam lithography used as working electrodes.
- Flame annealed platinum wires acted as counter electrode.
- Reference electrode: Ag/AgCl micro Dri-Ref reference electrode (WPI, Inc.).

- Potentiostat: Autolab potentiostat with Bipot module was used to control the working electrode potentials independently.
- pH meter: SevenMulti S47 (Mettler-Toledo; Giessen, D)
- Milli-Q water: Millipore Co., 18.2 MΩ.
- Britton-Robinson buffer: 0.04 M H_3BO_3, 0.04 M H_3PO_4 and 0.04 M CH_3COOH are mixed and then titrated to the desired pH with 0.2 M NaOH.

B. Publication lists

(1) Z. W. Yi, M. Banzet, A. Offenhausser, and D. Mayer. "Fabrication of nanogaps with modified morphology by potential-controlled gold deposition." *Physica Status Solidi-Rapid Research Letters*, 4(3-4):73–75, 2010.

(2) Z. W. Yi, S. Trellenkamp, A. Offenhausser, and D. Mayer. "Molecular junctions based on intermolecular electrostatic coupling." *Chemical Communications*, 46(42):8014–8016, 2010.

Bibliography

[1] Z. W. Yi, M. Banzet, A. Offenhausser, and D. Mayer. "Fabrication of nanogaps with modified morphology by potential-controlled gold deposition." *Physica Status Solidi-Rapid Research Letters*, 4(3-4):73–75, 2010. 1, 85, 92, 93

[2] Z. W. Yi, S. Trellenkamp, A. Offenhausser, and D. Mayer. "Molecular junctions based on intermolecular electrostatic coupling." *Chemical Communications*, 46(42):8014–8016, 2010. 2

[3] A. Aviram and M. A. Ratner. "Molecular Rectifiers." *Chemical Physics Letters*, 29(2):277–283, 1974. 5

[4] N. J. Geddes, J. R. Sambles, and A. S. Martin. "Organic molecular rectifiers." *Advanced Materials for Optics and Electronics*, 5(6):305–320, 1995. 5

[5] S. Kubatkin, A. Danilov, M. Hjort, J. Cornil, J. L. Bredas, N. Stuhr-Hansen, P. Hedegard, and T. Bjornholm. "Single-electron transistor of a single organic molecule with access to several redox states." *Nature*, 425(6959):698–701, 2003. 5, 22

[6] D. Mayer, Y. Q. Liu, and A. Offenhausser. "Electrochemical current rectification at bio-functionalized electrodes." *Bioelectrochemistry*, 77(2):89–93, 2010. 5, 7, 21

[7] R. Baron, O. Lioubashevski, E. Katz, T. Niazov, and I. Willner. "Logic gates and elementary computing by enzymes." *Journal of Physical Chemistry A*, 110(27):8548–8553, 2006. 5

[8] M. Sarikaya and C. Tamerler. "Genetically Designed Peptide-Based Molecular Materials." *Acs Nano*, 3(7):1606–1615, 2009. 5

[9] N. J. Tao. "Electron transport in molecular junctions." *Nature Nanotechnology*, 1(3):173–181, 2006. 5, 8

[10] K. H. Muller. "Effect of the atomic configuration of gold electrodes on the electrical conduction of alkanedithiol molecules." *Physical Review B*, 73(4), 2006. 6

[11] B. Q. Xu and N. J. J. Tao. "Measurement of single-molecule resistance by repeated formation of molecular junctions." *Science*, 301(5637):1221–1223, 2003. 6, 8

[12] J. Liu, J. L. Duan, E. Toimil-Molares, S. Karim, T. W. Cornelius, D. Dobrev, H. J. Yao, Y. M. Sun, M. D. Hou, D. Mo, Z. G. Wang, and R. Neumann. "Electrochemical fabrication of single-crystalline and polycrystalline Au nanowires: the influence of deposition parameters." *Nanotechnology*, 17(8):1922–1926, 2006. 6

[13] H. Martin, P. Carro, A. H. Creus, S. Gonzalez, R. C. Salvarezza, and A. J. Arvia. "Growth mode transition involving a potential-dependent isotropic to anisotropic surface atom diffusion change. Gold electrodeposition on HOPG followed by STM." *Langmuir*, 13(1):100–110, 1997. 6, 77, 81

[14] T. Li, W. P. Hu, and D. B. Zhu. "Nanogap Electrodes." *Advanced Materials*, 22(2):286–300, 2010. 6, 52

[15] G. Philipp, T. Weimann, P. Hinze, M. Burghard, and J. Weis. "Shadow evaporation method for fabrication of sub 10 nm gaps between metal electrodes." *Microelectronic Engineering*, 46(1-4):157–160, 1999. 6

[16] H. Park, A. K. L. Lim, A. P. Alivisatos, J. Park, and P. L. McEuen. "Fabrication of metallic electrodes with nanometer separation by electromigration." *Applied Physics Letters*, 75(2):301–303, 1999. 6

[17] N. J. Tao, C. Z. Li, and H. X. He. "Scanning tunneling microscopy applications in electrochemistry - beyond imaging." *Journal of Electroanalytical Chemistry*, 492(2):81–93, 2000. 6

[18] Z. J. Donhauser, B. A. Mantooth, K. F. Kelly, L. A. Bumm, J. D. Monnell, J. J. Stapleton, D. W. Price, A. M. Rawlett, D. L. Allara, J. M. Tour, and P. S. Weiss. "Conductance switching in single molecules through conformational changes." *Science*, 292(5525):2303–2307, 2001. 6

[19] J. Reichert, R. Ochs, D. Beckmann, H. B. Weber, M. Mayor, and H. von Lohneysen. "Driving current through single organic molecules." *Physical Review Letters*, 88(17), 2002. 6

[20] J. Xiang, B. Liu, S. T. Wu, B. Ren, F. Z. Yang, B. W. Mao, Y. L. Chow, and Z. Q. Tian. "A controllable electrochemical fabrication of metallic electrodes with a nanometer/angstrom-sized gap using an electric double layer as feedback." *Angewandte Chemie-International Edition*, 44(8):1265–1268, 2005. 6, 45

[21] Y. V. Kervennic, H. S. J. Van der Zant, A. F. Morpurgo, L. Gurevich, and L. P. Kouwenhoven. "Nanometer-spaced electrodes with calibrated separation." *Applied Physics Letters*, 80(2):321–323, 2002. 6

[22] J. M. van Ruitenbeek, N. Agrait, and A. L. Yeyati. "Quantum properties of atomic-sized conductors." *Physics Reports-Review Section of Physics Letters*, 377(2-3):81–279, 2003. 7, 16

[23] A. Erbe, L. A. Zotti, T. Kirchner, J. C. Cuevas, F. Pauly, T. Huhn, and E. Scheer. "Revealing the Role of Anchoring Groups in the Electrical Conduction Through Single-Molecule Junctions." *Small*, 6(14):1529–1535, 2010. 7

[24] J. D. Zhang, A. M. Kuznetsov, I. G. Medvedev, Q. J. Chi, T. Albrecht, P. S. Jensen, and J. Ulstrup. "Single-molecule electron transfer in electrochemical environments." *Chemical Reviews*, 108(7):2737–2791, 2008. 7

[25] L. Gruter, M. T. Gonzalez, R. Huber, M. Calame, and C. Schonenberger. "Electrical conductance of atomic contacts in liquid environments." *Small*, 1(11):1067–1070, 2005. 7

[26] X. L. Li, J. He, J. Hihath, B. Q. Xu, S. M. Lindsay, and N. J. Tao. "Conductance of single alkanedithiols: Conduction mechanism and effect of molecule-electrode contacts." *Journal of the American Chemical Society*, 128(6):2135–2141, 2006. 7

[27] M. Kiguchi, N. Sekiguchi, and K. Murakoshi. "Electric conductance of metal nanowires at mechanically controllable break junctions under electrochemical potential control." *Surface Science*, 601(22):5262–5265, 2007. 7, 65, 66, 97

[28] N. Kang, A. Erbe, and E. Scheer. "Observation of negative differential resistance in DNA molecular junctions." *Applied Physics Letters*, 96(2):–, 2010. 7, 8, 58, 65

[29] R. A. Marcus. "Electron-Transfer Reactions in Chemistry - Theory and Experiment (Nobel Lecture)." *Angewandte Chemie-International Edition in English*, 32(8):1111–1121, 1993. 7

[30] Q. J. Chi, J. D. Zhang, T. Arslan, L. Borg, G. W. Pedersen, H. E. M. Christensen, R. R. Nazmudtinov, and J. Ulstrup. "Approach to Interfacial and Intramolecular Electron Transfer of the Diheme Protein Cytochrome c(4) Assembled on Au(111) Surfaces." *Journal of Physical Chemistry B*, 114(16):5617–5624, 2010. 7

[31] M. Ubbink. "The courtship of proteins: Understanding the encounter complex." *Febs Letters*, 583(7):1060–1066, 2009. 8

[32] M. Sastry, M. Rao, and K. N. Ganesh. "Electrostatic assembly of nanoparticles and biomacromolecules." *Accounts of Chemical Research*, 35(10):847–855, 2002. 8

[33] R. L. McCreery and A. J. Bergren. "Progress with Molecular Electronic Junctions: Meeting Experimental Challenges in Design and Fabrication." *Advanced Materials*, 21(43):4303–4322, 2009. 8

[34] X. Y. Xiao, B. Q. Xu, and N. J. Tao. "Measurement of single molecule conductance: Benzenedithiol and benzenedimethanethiol." *Nano Letters*, 4(2):267–271, 2004. 8, 88

[35] J. R. Widawsky, M. Kamenetska, J. Klare, C. Nuckolls, M. L. Steigerwald, M. S. Hybertsen, and L. Venkataraman. "Measurement of voltage-dependent electronic transport across amine-linked single-molecular-wire junctions." *Nanotechnology*, 20(43):434009, 2009. 8

[36] C. H. Ko, M. J. Huang, M. D. Fu, and C. H. Chen. "Superior Contact for Single-Molecule Conductance: Electronic Coupling of Thiolate and Isothiocyanate on Pt, Pd, and Au." *Journal of the American Chemical Society*, 132(2):756–764, 2010. 8

[37] F. Chen, X. L. Li, J. Hihath, Z. F. Huang, and N. J. Tao. "Effect of anchoring groups on single-molecule conductance: Comparative study of thiol-, amine-, and carboxylic-acid-terminated molecules." *Journal of the American Chemical Society*, 128(49):15874–15881, 2006. 8

[38] M. Kiguchi and K. Murakoshi. "Conductance of single C-60 molecule bridging metal electrodes." *Journal of Physical Chemistry C*, 112(22):8140–8143, 2008. 8

[39] F. Chen, J. He, C. Nuckolls, T. Roberts, J. E. Klare, and S. Lindsay. "A molecular switch based on potential-induced changes of oxidation state." *Nano Letters*, 5(3):503–506, 2005. 8

[40] T. Albrecht, A. Guckian, J. Ulstrup, and J. G. Vos. "Transistor-like behavior of transition metal complexes." *Nano Letters*, 5(7):1451–1455, 2005. 8

[41] S. M. Wu, M. T. Gonzalez, R. Huber, S. Grunder, M. Mayor, C. Schonenberger, and M. Calame. "Molecular junctions based on aromatic coupling." *Nature Nanotechnology*, 3(9):569–574, 2008. 8, 48, 104

[42] S. A. Chang, J. He, L. S. Lin, P. M. Zhang, F. Liang, M. Young, S. Huang, and S. Lindsay. "Tunnel conductance of Watson-Crick nucleoside-base pairs from telegraph noise." *Nanotechnology*, 20(18):185102, 2009. 8

[43] S. Datta. *Electronic Transport in Mesoscopic Systems*. Cambridge University Press, 1997. 9

[44] D. A. Wharam, T. J. Thornton, R. Newbury, M. Pepper, H. Ahmed, J. E. F. Frost, D. G. Hasko, D. C. Peacock, D. A. Ritchie, and G. A. C. Jones. "One-Dimensional Transport and the Quantization of the Ballistic Resistance." *Journal of Physics C-Solid State Physics*, 21(8):L209–L214, 1988. 9, 11, 14

[45] E. L. Wolf. *Principles of Electron Tunneling Spectroscopy*. Oxford University Press, 1989. 9

[46] H. E. Katz, Z. N. Bao, and S. L. Gilat. "Synthetic chemistry for ultrapure, processable, and high-mobility organic transistor semiconductors." *Accounts of Chemical Research*, 34(5):359–369, 2001. 9

[47] R. Landauer. "Electrical Resistance of Disordered One-Dimensional Lattices." *Philosophical Magazine*, 21(172):863, 1970. 10

[48] M. Buttiker. "Scattering-Theory of Thermal and Excess Noise in Open Conductors." *Physical Review Letters*, 65(23):2901–2904, 1990. 10

[49] S. Yin, Z. Z. Sun, J. Lu, and X. R. Wang. "Explanation to the resistance anomaly observed in nanowires." *Applied Physics Letters*, 88(23), 2006. 10

[50] C. J. Muller, J. M. Vanruitenbeek, and L. J. Dejongh. "Conductance and Supercurrent Discontinuities in Atomic-Scale Metallic Constrictions of Variable Width." *Physical Review Letters*, 69(1):140–143, 1992. 10, 11

[51] J. K. Gimzewski and R. Moller. "Transition from the Tunneling Regime to Point Contact Studied Using Scanning Tunneling Microscopy." *Physical Review B*, 36(2):1284–1287, 1987. 11

[52] B. J. Van Wees, H. Van Houten, C. W. J. Beenakker, J. G. Williamson, L. P. Kouwenhoven, D. Van der Marel, and C. T. Foxon. "Quantized Conductance of Point Contacts in A Two-Dimensional Electron-Gas." *Physical Review Letters*, 60(9):848–850, 1988. 11

[53] J. Moreland and J. W. Ekin. "Electron-Tunneling Experiments Using Nb-Sn Break Junctions." *Journal of Applied Physics*, 58(10):3888–3895, 1985. 11

[54] C. J. Muller, J. M. Vanruitenbeek, and L. J. Dejongh. "Experimental-Observation of the Transition from Weak Link to Tunnel Junction." *Physica C*, 191(3-4):485–504, 1992. 11

[55] H. Ohnishi, Y. Kondo, and K. Takayanagi. "Quantized conductance through individual rows of suspended gold atoms." *Nature*, 395(6704):780–783, 1998. 11

[56] N. Agrait, A. L. Yeyati, and J. M. van Ruitenbeek. "Quantum properties of atomic-sized conductors." *Physics Reports-Review Section of Physics Letters*, 377(2-3):81–279, 2003. 11

[57] M. Law, J. Goldberger, and P. D. Yang. "Semiconductor nanowires and nanotubes." *Annual Review of Materials Research*, 34:83–122, 2004. 11

[58] E. Tekman and S. Ciraci. "Theoretical-Study of Transport through a Quantum Point Contact." *Physical Review B*, 43(9):7145–7169, 1991. 11

[59] A. P. Sutton and J. B. Pethica. "Inelastic Flow Processes in Nanometer Volumes of Solids." *Journal of Physics-Condensed Matter*, 2(24):5317–5326, 1990. 11

[60] E. Scheer, P. Joyez, D. Esteve, C. Urbina, and M. H. Devoret. "Conduction channel transmissions of atomic-size aluminum contacts." *Physical Review Letters*, 78(18):3535–3538, 1997. 11

[61] N. D. Lang. "Resistance of Atomic Wires." *Physical Review B*, 52(7):5335–5342, 1995. 12

[62] W. A. Deheer. "The Physics of Simple Metal-Clusters - Experimental Aspects and Simple-Models." *Reviews of Modern Physics*, 65(3):611–676, 1993. 12

[63] M. Brack. "The Physics of Simple Metal-Clusters - Self-Consistent Jellium Model and Semiclassical Approaches." *Reviews of Modern Physics*, 65(3):677–732, 1993. 12

[64] A. Kiejna and K. F. Wojciechowski. "Work Function of Metals - Relation Between Theory and Experiment." *Progress in Surface Science*, 11(4):293–338, 1981. 13

[65] R. L. David. *CRC Handbook of Chemistry and Physics, 90ed.* CRC Press, Boca Raton, 2009. 14, 99

[66] A. Nitzan. "Electron transmission through molecules and molecular interfaces." *Annual Review of Physical Chemistry*, 52:681–750, 2001. 15

[67] J. G. Simmons. "Generalized Formula for Electric Tunnel Effect Between Similar Electrodes Separated by A Thin Insulating Film." *Journal of Applied Physics*, 34(6):1793–1803, 1963. 19

[68] J. M. Beebe, B. Kim, J. W. Gadzuk, C. D. Frisbie, and J. G. Kushmerick. "Transition from direct tunneling to field emission in metal-molecule-metal junctions." *Physical Review Letters*, 97(2), 2006. 20

[69] R. H. Fowler and L. Nordheim. "Electron emission in intense electric fields." *Proceedings of the Royal Society of London Series a-Containing Papers of a Mathematical and Physical Character*, 119(781):173–181, 1928. 20

[70] M. G. Evans and J. Gergely. "A Discussion of the Possibility of Bands of Energy Levels in Proteins - Electronic Interaction in Non Bonded Systems." *Biochimica et Biophysica Acta*, 3(2):188–197, 1949. 21

[71] F. L. Carter. "Molecular-Level Fabrication Techniques and Molecular Electronic Devices." *Journal of Vacuum Science and Technology B*, 1(4):959–968, 1983. 21

[72] J. Zhao, J. L. Yang, and J. G. Hou. "Theoretical study of small two-dimensional gold clusters." *Physical Review B*, 67(8), 2003. 21

[73] U. Durig, O. Zuger, B. Michel, L. Haussling, and H. Ringsdorf. "Electronic and Mechanical Characterization of Self-Assembled Alkanethiol Monolayers by Scanning-Tunneling-Microscopy Combined with Interaction-Force-Gradient Sensing." *Physical Review B*, 48(3):1711–1717, 1993. 21

[74] L. A. Bumm, J. J. Arnold, M. T. Cygan, T. D. Dunbar, T. P. Burgin, L. Jones, D. L. Allara, J. M. Tour, and P. S. Weiss. "Are single molecular wires conducting?" *Science*, 271(5256):1705–1707, 1996. 21, 47

[75] R. P. Andres, T. Bein, M. Dorogi, S. Feng, J. I. Henderson, C. P. Kubiak, W. Mahoney, R. G. Osifchin, and R. Reifenberger. ""Coulomb staircase" at room temperature in a self-assembled molecular nanostructure." *Science*, 272(5266):1323–1325, 1996. 21

[76] T. Vondrak, C. J. Cramer, and X. Y. Zhu. "The nature of electronic contact in self-assembled monolayers for molecular electronics: Evidence for strong coupling." *Journal of Physical Chemistry B*, 103(42):8915–8919, 1999. 22

[77] R. A. Marcus and N. Sutin. "Electron Transfers in Chemistry and Biology." *Biochimica et Biophysica Acta*, 811(3):265–322, 1985. 22

[78] Y. Q. Xue and M. A. Ratner. "Microscopic study of electrical transport through individual molecules with metallic contacts. II. Effect of the interface structure." *Physical Review B*, 68(11), 2003. 23

[79] D. Supriyo. *Electronic Transport in Mesoscopic Systems*. Cambridge University Press, 1995. 23

[80] A. J. Bard and L. R. Faulkner. *Electrochemical Methods: Fundamentals and Applications*. Wiley; 2 edition, 2000. 25, 26, 29

[81] O. Stern. "The theory of the electrolytic double shift." *Zeitschrift Fur Elektrochemie Und Angewandte Physikalische Chemie*, 30:508–516, 1924. 25

[82] Y. Zhang, J. Z. Zhou, L. L. Lin, and Z. H. Lin. "Determination of electrochemical electron-transfer reaction standard rate constants at nanoelectrodes: Standard rate constants for ferrocenylmethyltrimethylammonium(III)/(II) and hexacyanoferrate(III)/(II)." *Electroanalysis*, 20(13):1490–1494, 2008. 32

[83] I. Heller, J. Kong, H. A. Heering, K. A. Williams, S. G. Lemay, and C. Dekker. "Individual single-walled carbon nanotubes as nanoelectrodes for electrochemistry." *Nano Letters*, 5(1):137–142, 2005. 32

[84] D. W. M. Arrigan. "Nanoelectrodes, nanoelectrode arrays and their applications." *Analyst*, 129(12):1157–1165, 2004. 33

[85] B. B. Evgeni, T. S. Georgi, and J. L. Wolfgang. *Electrochemical Phase Formation and Growth*. VCH, 1996. 35

[86] B. Scharifker and G. Hills. "Theoretical and Experimental Studies of Multiple Nucleation." *Electrochimica Acta*, 28(7):879–889, 1983. 35, 76, 77

[87] P. Allongue and E. Souteyrand. "Metal Electrodeposition on Semiconductors .1. Comparison with Glassy-Carbon in the Case of Platinum Deposition." *Journal of Electroanalytical Chemistry*, 286(1-2):217–237, 1990. 35, 77

[88] D. A. Doane. "OPTICAL LITHOGRAPHY IN THE 1-MU-M LIMIT." *Solid State Technology*, 23(8):101–114, 1980. 38

[89] C. Vieu, F. Carcenac, A. Pepin, Y. Chen, M. Mejias, A. Lebib, L. Manin-Ferlazzo, L. Couraud, and H. Launois. "Electron beam lithography: resolution limits and applications." *Applied Surface Science*, 164:111–117, 2000. 41

[90] M. Parikh. "Corrections to Proximity Effects in Electron-Beam Lithography .1. Theory." *Journal of Applied Physics*, 50(6):4371–4377, 1979. 41

[91] M. Parikh. "Corrections to Proximity Effects in Electron-Beam Lithography .2. Implementation." *Journal of Applied Physics*, 50(6):4378–4382, 1979. 41

[92] M. Parikh. "Corrections to Proximity Effects in Electron-Beam Lithography .3. Experiments." *Journal of Applied Physics*, 50(6):4383–4387, 1979. 41

[93] C. R. K. Marrian and D. M. Tennant. "Nanofabrication." *Journal of Vacuum Science and Technology A*, 21(5):S207–S215, 2003. 41

[94] L. T. Canham. "Silicon quantum wire array fabrication by electrochemical and chemical dissolution of wafers." *Applied Physics Letters*, 57(10):1046–1048, 1990. 44

[95] D. Routkevitch, T. Bigioni, M. Moskovits, and J. M. Xu. "Electrochemical fabrication of CdS nanowire arrays in porous anodic aluminum oxide templates." *Journal of Physical Chemistry*, 100(33):14037–14047, 1996. 44

[96] E. W. Wong, C. P. Collier, M. Behloradsky, F. M. Raymo, J. F. Stoddart, and J. R. Heath. "Fabrication and transport properties of single-molecule-thick electrochemical junctions." *Journal of the American Chemical Society*, 122(24):5831–5840, 2000. 44

[97] M. J. Zheng, L. D. Zhang, G. H. Li, and W. Z. Shen. "Fabrication and optical properties of large-scale uniform zinc oxide nanowire arrays by one-step electrochemical deposition technique." *Chemical Physics Letters*, 363(1-2):123–128, 2002. 44

[98] P. C. Hidber, W. Helbig, E. Kim, and G. M. Whitesides. "Microcontact printing of palladium colloids: Micron-scale patterning by electroless deposition of copper." *Langmuir*, 12(5):1375–1380, 1996. 44

[99] Y. Kobayashi, V. Salgueirino-Maceira, and L. M. Liz-Marzan. "Deposition of sliver nanoparticles on silica spheres by pretreatment steps in electroless plating." *Chemistry of Materials*, 13(5):1630–1633, 2001. 44

[100] R. L. McCreery. "Molecular electronic junctions." *Chemistry of Materials*, 16(23):4477–4496, 2004. 47

[101] P. L. McEuen, J. Park, A. N. Pasupathy, J. I. Goldsmith, C. Chang, Y. Yaish, J. R. Petta, M. Rinkoski, J. P. Sethna, H. D. Abruna, and D. C. Ralph. "Coulomb blockade and the Kondo effect in single-atom transistors." *Nature*, 417(6890):722–725, 2002. 47

[102] T. Bjornholm, A. Danilov, S. Kubatkin, S. Kafanov, P. Hedegard, N. Stuhr-Hansen, and K. Moth-Poulsen. "Electronic transport in single molecule junctions: Control of the molecule-electrode coupling through intramolecular tunneling barriers." *Nano Letters*, 8(1):1–5, 2008. 47

[103] K. Slowinski, H. K. Y. Fong, and M. Majda. "Mercury-Mercury Tunneling Junctions. 1. Electron Tunneling Across Symmetric and Asymmetric Alkanethiolate Bilayers." *Journal of the American Chemical Society*, 121(31):7257–7261, 1999. 47

[104] G. S. Bang, H. Chang, J.-R. Koo, T. Lee, R. C. Advincula, and H. Lee. "High-Fidelity Formation of a Molecular-Junction Device Using a Thickness-Controlled Bilayer Architecture." *Small*, 4(9):1399–1405, 2008. 47

[105] A. Danilov, S. Kubatkin, S. Kafanov, P. Hedegard, N. Stuhr-Hansen, K. Moth-Poulsen, and T. Bjornholm. "Electronic transport in single molecule junctions: Control of the molecule-electrode coupling through intramolecular tunneling barriers." *Nano Letters*, 8(1):1–5, 2008. 47

[106] K. Moth-Poulsen, L. Patrone, N. Stuhr-Hansen, J. B. Christensen, J. P. Bourgoin, and T. Bjornholm. "Probing the effects of conjugation path on the electronic transmission through single molecules using scanning tunneling microscopy." *Nano Letters*, 5(4):783–785, 2005. 47

[107] C. P. Collier, E. W. Wong, M. Belohradsky, F. M. Raymo, J. F. Stoddart, P. J. Kuekes, R. S. Williams, and J. R. Heath. "Electronically configurable molecular-based logic gates." *Science*, 285(5426):391–394, 1999. 47

[108] A. R. Pease, J. O. Jeppesen, J. F. Stoddart, Y. Luo, C. P. Collier, and J. R. Heath. "Switching devices based on interlocked molecules." *Accounts of Chemical Research*, 34(6):433–444, 2001. 47

[109] J. Zikovsky, S. A. Dogel, A. B. Haider, G. A. DiLabio, and R. A. Wolkow. "Self-directed growth of contiguous perpendicular molecular lines on H-Si(100) surfaces." *Journal of Physical Chemistry A*, 111(49):12257–12259, 2007. 47

[110] A. Scott, D. B. Janes, C. Risko, and M. A. Ratner. "Fabrication and characterization of metal-molecule-silicon devices." *Applied Physics Letters*, 91(3), 2007. 47

[111] R. Sordan, M. Burghard, and K. Kern. "Removable template route to metallic nanowires and nanogaps." *Applied Physics Letters*, 79(13):2073–2075, 2001. 52

[112] X. L. Li, S. Z. Hua, H. D. Chopra, and N. J. Tao. "Formation of atomic point contacts and molecular junctions with a combined mechanical break junction and electrodeposition method." *Micro and Nano Letters*, 1(2):83–88, 2006. 52, 69

[113] C. Z. Li, H. X. He, and N. J. Tao. "Quantized tunneling current in the metallic nanogaps formed by electrodeposition and etching." *Applied Physics Letters*, 77(24):3995–3997, 2000. 52, 56, 72, 83, 85, 86

[114] D. E. Johnston, D. R. Strachan, and A. T. C. Johnson. "Parallel fabrication of nanogap electrodes." *Nano Letters*, 7(9):2774–2777, 2007. 52

[115] H. Zhang, C. V. Thompson, F. Stellacci, and J. T. L. Thong. "Parallel fabrication of polymer-protected nanogaps." *Nanotechnology*, 21(38):–, 2010. 52

[116] C. A. Mack. *Corner rounding and line-end shortening in optical lithography*, pp. 83–92. MICROLITHOGRAPHIC TECHNIQUES IN INTEGRATED CIRCUIT FABRICATION II Proceedings of the society of photo-optical instrumentation engineers (Spie). Society of Photo Optical, 2000. S. 54

[117] S. Trellenkamp. "Designing patterns for the electron beam lithography.", 2009. 55

[118] P. Shi and P. W. Bohn. "Stable atom-scale junctions on silicon fabricated by kinetically controlled electrochemical deposition and dissolution." *Acs Nano*, 2(8):1581–1588, 2008. 55, 63, 72

[119] T. Blom, K. Welch, M. Stromme, E. Coronel, and K. Leifer. "Fabrication and characterization of highly reproducible, high resistance nanogaps made by focused ion beam milling." *Nanotechnology*, 18(28):–, 2007. 55, 63

[120] F. Chen, Q. Qing, L. Ren, Z. Y. Wu, and Z. F. Liu. "Electrochemical approach for fabricating nanogap electrodes with well controllable separation." *Applied Physics Letters*, 86(12):–, 2005. 56, 74, 80

[121] S. Nils. "Conducting AFM measurment of physical deposited gold surface.", 2010. 56

[122] L. A. Zotti, T. Kirchner, J. C. Cuevas, F. Pauly, T. Huhn, E. Scheer, and A. Erbe. "Revealing the Role of Anchoring Groups in the Electrical Conduction Through Single-Molecule Junctions." *Small*, 6(14):1529–1535, 2010. 58

[123] F. O. Hadeed and C. Durkan. "Controlled fabrication of 1-2 nm nanogaps by electromigration in gold and gold-palladium nanowires." *Applied Physics Letters*, 91(12):–, 2007. 58

[124] M. L. Trouwborst, S. J. van der Molen, and B. J. van Wees. "The role of Joule heating in the formation of nanogaps by electromigration." *Journal of Applied Physics*, 99(11):–, 2006. 58

[125] F. Prins, T. Hayashi, B. J. A. D. van Steenwijk, B. Gao, E. A. Osorio, K. Muraki, and H. S. J. van der Zant. "Room-temperature stability of Pt nanogaps formed by self-breaking." *Applied Physics Letters*, 94(12):–, 2009. 58

[126] Y. Tomoda, K. Takahashi, M. Hanada, W. Kume, and J. Shirakashi. "Fabrication of nanogap electrodes by field-emission-induced electromigration." *Journal of Vacuum Science and Technology B*, 27(2):813–816, 2009. 58

[127] G. Esen and M. S. Fuhrer. "Temperature control of electromigration to form gold nanogap junctions." *Applied Physics Letters*, 87(26), 2005. 58

[128] Q. Qing, F. Chen, P. G. Li, W. H. Tang, Z. Y. Wu, and Z. F. Liu. "Finely tuning metallic nanogap size with electrodeposition by utilizing high-frequency impedance in feedback." *Angewandte Chemie-International Edition*, 44(47):7771–7775, 2005. 59, 80

[129] D. R. Strachan, D. E. Smith, D. E. Johnston, T. H. Park, M. J. Therien, D. A. Bonnell, and A. T. Johnson. "Controlled fabrication of nanogaps in ambient environment for molecular electronics." *Applied Physics Letters*, 86(4):–, 2005. 59

[130] M. D. Fischbein and M. Drndic. "Nanogaps by direct lithography for high-resolution imaging and electronic characterization of nanostructures." *Applied Physics Letters*, 88(6):–, 2006. 60

[131] H. Suga, M. Horikawa, S. Odaka, H. Miyazaki, K. Tsukagoshi, T. Shimizu, and Y. Naitoh. "Influence of electrode size on resistance switching effect in nanogap junctions." *Applied Physics Letters*, 97(7):–, 2010. 63

[132] J. H. Tian, Y. Yang, B. Liu, B. Schollhorn, D. Y. Wu, E. Maisonhaute, A. S. Muns, Y. Chen, C. Amatore, N. J. Tao, and Z. Q. Tian. "The fabrication and characterization of adjustable nanogaps between gold electrodes on chip for electrical measurement of single molecules." *Nanotechnology*, 21(27):–, 2010. 65, 66, 67, 68, 70, 93, 97

[133] G. G. Wallace, S. E. Moulton, J. N. Barisci, A. Bath, and R. Stella. "Studies of double layer capacitance and electron transfer at a gold electrode exposed to protein solutions." *Electrochimica Acta*, 49(24):4223–4230, 2004. 65

[134] D. Mayer, F. Schroper, D. Bruggemann, Y. Mourzina, B. Wolfrum, and A. Offenhausser. "Analyzing the electroactive surface of gold nanopillars by electrochemical methods for electrode miniaturization." *Electrochimica Acta*, 53(21):6265–6272, 2008. 66

[135] C. H. Cho, B. H. Kim, S. K. Kim, and S. J. Park. "Characterization of electronic structure of silicon nanocrystals in silicon nitride by capacitance spectroscopy." *Applied Physics Letters*, 96(22), 2010. 69

[136] D. M. Jordan, R. H. Haslam, K. Mallik, R. J. Falster, and P. R. Wilshaw. "The Development of Semi-Insulating Silicon Substrates for Microwave Devices." *Journal of the Electrochemical Society*, 157(5):H540–H545, 2010. 69

[137] A. D. Yadav, A. P. Patel, S. K. Dubey, B. K. Panigrahi, R. Kesavamoorthy, and K. G. M. Nair. "Structural characterization of buried nitride layers formed by nitrogen ion implantation in silicon." *Nuclear Instruments and Methods in Physics Research Section B-Beam Interactions with Materials and Atoms*, 266(8):1447–1449, 2008. 69

[138] S. W. Howell, S. M. Dirk, K. Childs, H. Pang, M. Blain, R. J. Simonson, J. M. Tour, and D. R. Wheeler. "Mass-fabricated one-dimensional silicon nanogaps for hybrid organic/nanoparticle arrays." *Nanotechnology*, 16(6):754–758, 2005. 69

[139] Y. Yasutake, K. Kono, M. Kanehara, T. Teranishi, M. R. Buitelaar, C. G. Smith, and Y. Majima. "Simultaneous fabrication of nanogap gold electrodes by electroless gold plating using a common medical liquid." *Applied Physics Letters*, 91(20):–, 2007. 71

[140] G. Meszaros, S. Kronholz, S. Karthauser, D. Mayer, and T. Wandlowski. "Electrochemical fabrication and characterization of nanocontacts and nm-sized gaps." *Applied Physics A-Materials Science and Processing*, 87(3):569–575, 2007. 72, 74

[141] M. Kunitake, U. Akiba, N. Batina, and K. Itaya. "Structures and dynamic formation processes of porphyrin adlayers on iodine-modified Au(111) in solution: In situ STM study." *Langmuir*, 13(6):1607–1615, 1997. 72

[142] T. Osaka, A. Kodera, T. Misato, T. Homma, Y. Okinaka, and O. Yoshioka. "Electrodeposition of soft gold from a thiosulfate-sulfite bath for electronics applications." *Journal of the Electrochemical Society*, 144(10):3462–3469, 1997. 72

[143] T. A. Green, M. J. Liew, and S. Roy. "Electrodeposition of gold from a thiosulfate-sulfite bath for microelectronic applications." *Journal of the Electrochemical Society*, 150(3):C104–C110, 2003. 72

[144] M. A. Diaz, G. H. Kelsall, and N. J. Welham. "Electrowinning Coupled to Gold Leaching by Electrogenerated Chlorine .1. Au(Iii)-Au(I)/Au Kinetics in Aqueous Cl2/Cl- Electrolytes." *Journal of Electroanalytical Chemistry*, 361(1-2):25–38, 1993. 72

[145] U. Schmidt, M. Donten, and J. G. Osteryoung. "Gold electrocrystallization on carbon and highly oriented pyrolytic graphite from concentrated solutions of LiCl." *Journal of the Electrochemical Society*, 144(6):2013–2021, 1997. 72, 73, 76

[146] J. E. Anderson and S. M. Sawtelle. "Insitu Generation and Characterization of Gold(I) Complexes from K[Aucl4] in Aqueous-Solutions." *Inorganica Chimica Acta*, 194(2):171–177, 1992. 72

[147] Y. V. Kervennic and S. Kubatkin. "Fabrication of Clean Nanogaps Using a Combined Electrochemical-Chemical Method." *Small*, 5(22):2541–2544, 2009. 74, 87

[148] G. Gunawardena, G. Hills, I. Montenegro, and B. Scharifker. "Electrochemical Nucleation .1. General-Considerations." *Journal of Electroanalytical Chemistry*, 138(2):225–239, 1982. 75

[149] B. R. Scharifker and J. Mostany. "3-Dimensional Nucleation with Diffusion Controlled Growth .1. Number Density of Active-Sites and Nucleation Rates Per Site." *Journal of Electroanalytical Chemistry*, 177(1-2):13–23, 1984. 75

[150] J. Mostany, J. Mozota, and B. R. Scharifker. "3-Dimensional Nucleation with Diffusion Controlled Growth .2. The Nucleation of Lead on Vitreous Carbon." *Journal of Electroanalytical Chemistry*, 177(1-2):25–37, 1984. 75

[151] G. Hills, A. K. Pour, and B. Scharifker. "The Formation and Properties of Single Nuclei." *Electrochimica Acta*, 28(7):891–898, 1983. 76

[152] L. Komsiyska and G. Staikov. "Electrocrystallization of Au nanoparticles on glassy carbon from HClO(4) solution containing [AuCl(4)](-)." *Electrochimica Acta*, 54(2):168–172, 2008. 77

[153] E. S. Kooij, E. A. M. Brouwer, and B. Poelserna. "Electric field assisted nanocolloidal gold deposition." *Journal of Electroanalytical Chemistry*, 611(1-2):208–216, 2007. 79

[154] C. S. Ah, Y. J. Yun, J. S. Lee, H. J. Park, D. H. Ha, and W. S. Yun. "Fabrication of integrated nanogap electrodes by surface-catalyzed chemical deposition." *Applied Physics Letters*, 88(13):–, 2006. 80

[155] T. Michely and J. Krug. *Islands, Mounds, and Atoms: Patterns and Processes in Crystal Growth Far from Equilibrium*. Springer, Berlin, 2004. 81

[156] L. Komsiyska, V. Tsakova, and G. Staikov. "Electrochemical formation and properties of thin polyaniline films on Au(111) and p-Si(111)." *Applied Physics A-Materials Science and Processing*, 87(3):405–409, 2007. 82

[157] C. Shu, C. Z. Li, H. X. He, A. Bogozi, J. S. Bunch, and N. J. Tao. "Fractional conductance quantization in metallic nanoconstrictions under electrochemical potential control." *Physical Review Letters*, 84(22):5196–5199, 2000. 85

[158] C. F. Narambuena, M. G. Del Popolo, and E. P. M. Leiva. "On the reasons for stepwise changes in the tunneling current across metallic nanogaps." *Nano Letters*, 3(12):1633–1637, 2003. 85

[159] M. A. Reed, C. Zhou, C. J. Muller, T. P. Burgin, and J. M. Tour. "Conductance of a molecular junction." *Science*, 278(5336):252–254, 1997. 88

[160] M. Tsutsui, Y. Teramae, S. Kurokawa, and A. Sakai. "High-conductance states of single benzenedithiol molecules." *Applied Physics Letters*, 89(16), 2006. 88

[161] K. Horiguchi, S. Kurokawa, and A. Sakai. "Conductance and I-V characteristics of Au/BPY/Au single molecule junctions." *Journal of Chemical Physics*, 131(10), 2009. 88

[162] N. Hatanaka, M. Endo, S. Okumura, Y. Ie, R. Yamada, Y. Aso, K. Tanaka, and H. Tada. "Electrical conductance measurement of oligothiophene molecular wires using nanogap electrodes prepared by electrochemical plating." *Chemistry Letters*, 36(2):224–225, 2007. 88

[163] X. D. Dong, Y. Xia, G. Y. Zhu, and B. L. Zhang. "Molecular sensing with the tunnel junction of an Au nanogap in solution." *Nanotechnology*, 18(39):–, 2007. 88, 93

[164] T. T. Liang, Y. Naitoh, M. Horikawa, T. Ishida, and W. Mizutani. "Fabrication of steady junctions consisting of alpha,omega-bis(thioacetate) oligo(p-phenylene vinylene)s in nanogap electrodes." *Journal of the American Chemical Society*, 128(42):13720–13726, 2006. 88

[165] D. R. Strachan, D. E. Smith, M. D. Fischbein, D. E. Johnston, B. S. Guiton, M. Drndic, D. A. Bonnell, and A. T. Johnson. "Clean electromigrated nanogaps imaged by transmission electron microscopy." *Nano Letters*, 6(3):441–444, 2006. 88

[166] X. Y. Xiao, D. Brune, J. He, S. Lindsay, C. B. Gorman, and N. J. Tao. "Redox-gated electron transport in electrically wired ferrocene molecules." *Chemical Physics*, 326(1):138–143, 2006. 98, 101, 102, 104

[167] G. E. Coates. *Organo-Metallic Compounds*. Wiley, New York, 1960. 99

[168] O. Azzaroni, B. Yameen, and W. Knoll. "Effect of the electrostatic microenvironment on the observed redox potential of electroactive supramolecular bioconjugates." *Physical Chemistry Chemical Physics*, 10(46):7031–7038, 2008. 101

[169] H. T. Smith, A. J. Ahmed, and F. Millett. "Electrostatic Interaction of Cytochrome-C with Cytochrome-C1 and Cytochrome-Oxidase." *Journal of Biological Chemistry*, 256(10):4984–4990, 1981. 104

[170] T. W. Hamann, F. Gstrein, B. S. Brunschwig, and N. S. Lewis. "Measurement of the dependence of interfacial charge-transfer rate constants on the reorganization

energy of redox species at n-ZnO/H2O interfaces." *Journal of the American Chemical Society*, 127(40):13949–13954, 2005. 104

Acknowledgement / Danksagung

Foremost, I would like to express my sincere gratitude to my advisor Dr. Dirk Mayer for the continuous support of my doctoral study and research. He brought me to a fascinating research world. He taught me the disciplines of doing research, which is to provide knowledge that people are interested in or will be interested in. Dr. Dirk Mayer demonstrated the key to becoming a qualified scientist: communicating with colleagues with properly presented results. He also trained me how to write scientific papers. The general structure of scientific writing should be written like this: the state-of-art knowledge of the topic is firstly presented, and then the results are described and compared with the already known knowledge. Through the comparison, conclusion should be made that which knowledge can be obtained through the experiments. Dr. Dirk Mayer gave me instructions on how to organize data. For example: when presenting results, always provides references (books or scientific publications); avoid using sentence like "Something is something", just use more descriptive words; try use always the same tense, at least within one paragraph; when describing figures, first make a statement and then use the graphs and pictures to support the statement. His strict trainings helped me a lot during my PhD research and I believe I would benefit from these experiences in my future career.

Besides my advisor, I would like to thank Prof. Andreas Offenhäuser, especially for his guidance of my doctoral thesis and financial support during my doctoral study. Without his support, I can not accomplish my doctoral study.

I would like to thank the thesis committee: Prof. Andreas Offenhäuser and Prof. Ulrich Simon for their encouragement, insightful comments, and hard questions.

My sincere thanks also go to Dr. Stefan Trellenkamp for his assistance in the nanostructure fabrication using electron beam writer, Marco Banzet and Michael Prömpers for their guidance to work in the cleanroom.

I thank my fellow labmates in bioelectronics group: Florian Schröper, Karolina Caban, Martina Hitzbleck, Yaqing Liu, Dong Xiang, Sandra Gilles, Benyan Liu, for the stimulating discussions and for all the fun we have had in the last four years. I also thank Peigang Li from IBN-3, for the helpful collaboration in fabricating nanogap electrodes.

1. **Ferrocenes as Potential Building Blocks for Molecular Electronics**
   Self-Assembly and Tunneling Spectroscopy
   by L. Müller-Meskamp (2008), 153 pages
   ISBN: 978-3-89336-509-8

2. **Magnetic Proximity Effects in Highly-ordered Transition Metal Oxide Heterosystems studied by Soft x-Ray Photoemission Electron Microscopy**
   by I. P. Krug (2008), XX, 180 pages
   ISBN: 978-3-89336-521-0

3. **Seltenerd-basierte ternäre Oxide als alternative Gatedielektrika**
   von J. M. Roeckerath (2008), 148 Seiten
   ISBN: 978-3-89336-543-2

4. **Strominduzierte Magnetisierungsdynamik in einkristallinen Nanosäulen**
   von R. Lehndorff (2009), I, 86 Seiten
   ISBN: 978-3-89336-564-7

5. **Magnetization Dynamics in Magnetically Coupled Heterostructures**
   von A. Kaiser (2009), X, 121 pages
   ISBN: 978-3-89336-577-7

6. **Resistive switching in Pt/TiO_2/PT**
   by D. S. Jeong (2009), vii, 133 pages
   ISBN: 978-3-89336-579-1

7. **Electromechanical Force Microscopy and Tip-Enhanced Raman Spectroscopy for Polar Oxide Nanoparticles**
   by S. Röhrig (2009), vi, 114 pages
   ISBN: 978-3-89336-600-2

8. **Investigation of resistive switching in barium strontium titanate thin films for memory applications**
   by W. Shen (2010), 114 pages
   ISBN: 978-3-89336-608-8

9. **Nanostrukturierte Metallelektroden zur funktionalen Kopplung an neuronale Zellen**
   von D. Brüggemann (2010), vii, 160 Seiten
   ISBN: 978-3-89336-627-9

10. **Integration of resistive switching devices in crossbar structures**
    by Chr. Nauenheim (2010), XII, 142 pages
    ISBN: 978-3-89336-636-1

11. **Correlation between Raman spectroscopy and electron microscopy on individual carbon nanotubes and peapods**
by C. Spudat (2010). xiv, 125 pages
ISBN: 978-3-89336-648-4

12. **DC and RF Characterization of NiSi Schottky Barrier MOSFETs with Dopant Segregation**
by C. J. Urban (2010), iv, 151 pages
ISBN: 978-3-89336-644-6

13. **Alternative Systems for Molecular Electronics: Functionalized Carboxylic Acids on Structured Surfaces**
by M. C. Lennartz (2010), 183 pages
ISBN: 978-3-89336-667-5

14. **Highly conductive electrodes as diffusion barrier for high temperature applications**
by B. Meši (2010), VII, 138 pages
ISBN: 978-3-89336-670-5

15. **Modeling, Fabrication and Characterization of Silicon Tunnel Field-Effect Transistors**
by C. P. Sandow (2010), XIII, 112 pages
ISBN: 978-3-89336-675-0

16. **Substituted Coronenes for Molecular Electronics: From Supramolecular Structures to Single Molecules**
by P. Kowalzik (2010), ix, 149 pages
ISBN: 978-3-89336-679-8

17. **Resistive switching in TiO2 thin films**
by L. Yang (2011), VII, 117 pages
ISBN: 978-3-89336-707-8

18. **Crystal- and Defect-Chemistry of Fine Grained Thermistor Ceramics on $BaTiO_3$ Basis with BaO-Excess**
by H. Katsu (2011), xxvii, 163 pages
ISBN: 978-3-89336-741-2

19. **Flächenkontakte zu molekularen Schichten in der Bioelektronik**
von N. Sanetra (2012), XIII, 129 Seiten
ISBN: 978-3-89336-776-4

20. **Stacked device structures for resistive memory and logic**
by R. D. Rosezin (2012), 137 pages
ISBN: 978-3-89336-777-1

21. **Optical and electrical addressing in molecule-based logic circuits**
by M. Manheller (2012), XIV, 183 pages
ISBN: 978-3-89336-810-5

22. **Fabrication of Nanogaps and Investigation of Molecular Junctions by Electrochemical Methods**
by Z. Yi (2012), 132 pages
ISBN: 978-3-89336-812-9

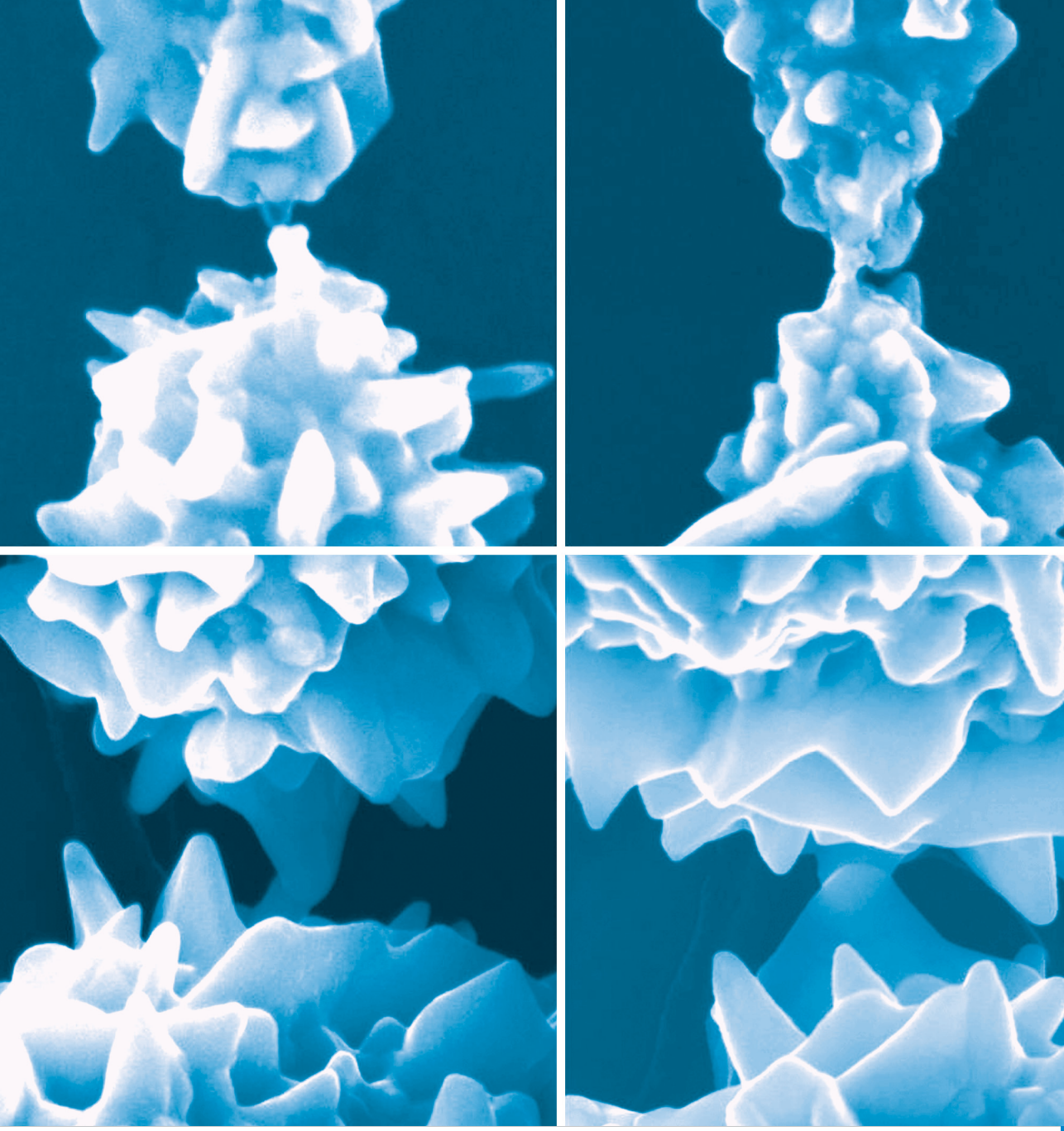

Information / Information
Band / Volume 22
ISBN 978-3-89336-812-9

JÜLICH
FORSCHUNGSZENTRUM